

TALLINN UNIVERSITY OF TECHNOLOGY
DOCTORAL THESIS
22/2019

Spatially Resolved Opto-electronical Investigations of Monograin Layer Solar Cells

CHRISTIAN NEUBAUER



TALLINN UNIVERSITY OF TECHNOLOGY

School of Engineering

Department of Materials and Environmental Technology

This dissertation was accepted for the defence of the degree 06/03/2019

Supervisor:

Prof. Dipl.-Chem. Dr. Dr. Dieter Meissner
School of Engineering
Department of Materials and Environmental Technology
TalTech, Tallinn, Estonia

Opponents:

Prof. Dr. Dr. Hans-Werner Schock
Helmholz Zentrum Berlin
Institute Competence Centre Photovoltaics Berlin
Berlin, Germany

Prof. Dr. Marco Kirm
Faculty of Science and Technology
Institute of Physics
University of Tartu, Tartu, Estonia

Defence of the thesis: 20/05/2019, Tallinn

Declaration:

Hereby I declare that this doctoral thesis, my original investigation and achievement, submitted for the doctoral degree at Tallinn University of Technology, has not been previously submitted for doctoral or equivalent academic degree.

Christian Neubauer

signature



European Union
European Regional
Development Fund



Investing
in your future

Copyright: Christian Neubauer, 2019

ISSN 2585-6898 (publication)

ISBN 978-9949-83-411-2 (publication)

ISSN 6898-6901 (PDF)

ISBN 978-9949-83-412-9 (PDF)

TALLINNA TEHNIKAÜLIKOOL
DOKTORITÖÖ
22/2019

**Monoterliste päikesepatareide
ruumilise lahutusega optoelektronsed
uuringud**

CHRISTIAN NEUBAUER



Contents

List of Publications	7
Author's Contribution to the Publications	8
Introduction	9
Abbreviations	11
1 Literature overview	12
1.1 Kesterite thin film and monograin layer solar cells.....	12
1.1.1 Kesterite absorber material	12
1.1.2 The monograin layer technology	13
1.2 Spatially resolved opto-electrical evaluation methods for solar cells.....	14
1.2.1 LBIC	14
1.2.2 EBIC	16
1.3 Ageing and degradation mechanism of photovoltaic devices	16
1.4 Aim of the thesis	17
2 Experimental	18
2.1 Sample preparation.....	18
2.1.1 Monograin synthesis.....	18
2.1.2 Device fabrication	18
2.1.3 Device ageing	20
2.2 Analysis methods	20
2.2.1 Current density/voltage measurements	20
2.2.2 External quantum efficiency and wavelength dependent transmission measurements	20
2.2.3 Light beam induced current measurements	20
2.2.4 Scanning electron microscopy and electron beam induced current measurements.	21
2.2.5 Raman and photoluminescence spectroscopy.....	21
2.2.6 Electroluminescence	21
2.2.7 X-ray photoelectron spectrometry	21
2.2.8 Optical microscopy.....	21
2.2.9 Kelvin Probe measurements	21
3 Results and discussion.....	23
3.1 Development of new analysis methods of spatially resolved photocurrent measurements	23
3.2 Application of spatially resolved investigations on MGL solar cells by means of LBIC.	26
3.3 Identification of reasons for inhomogeneities and performance reducing effects ..	28
3.4 Utilization of spatially resolved and integrated opto-electrical measurements for the identification of ageing processes.....	33
4 Conclusions	47
References	49
Abstract.....	62
Kokkuvõte	64

Appendix	67
Curriculum vitae.....	98
Elulookirjeldus.....	100

List of Publications

The list of author's publications, on the basis of which the thesis has been prepared:

- I **Neubauer, C.**, Babatas, E., Meissner, D. (2017). Investigation of rough surfaces on $\text{Cu}_2\text{ZnSn}(\text{S}_x\text{Se}_{1-x})_4$ monograin layers using light beam induced current measurements. *Appl. Surf. Sci.*, 423, 465-468.
- II **Neubauer, C.**, Samieipour, A., Oueslati, S., Ernits, K., Meissner, D. (2018). Spatially resolved opto-electrical performance investigations of $\text{Cu}_2\text{ZnSnS}_{3.2}\text{Se}_{0.8}$ photovoltaic devices. *Energy Sci Eng.*, 6, 563-569.
- III **Neubauer, C.**, Samieipour, A., Oueslati, S., Danilson, M., Meissner, D. (2019). Ageing of Kesterite solar cells 1: Degradation processes and their influence on solar cell parameters. *Thin Solid Films*, 669, 595-599.
- IV Samieipour, A., **Neubauer, C.**, Oueslati, S., Mikli, V., Meissner, D. (2019). Ageing of Kesterite solar cells 2: Impact on photocurrent generation. *Thin Solid Films*, 669, 509-513.

Author's Contribution to the Publications

Contribution to the papers in this thesis are:

- I Part in sample preparation, major part in measurements and evaluation (SEM, LBIC, j/V), major part in writing.
- II Part in sample preparation, sample measurements and evaluation (LBIC, transmission, EL imaging and spectra measurements, PL spectra measurements, SEM, j/V), major part in writing.
- III Part in sample preparation, sample measurements and evaluation (j/V, PL), major part in writing.
- IV Part in sample preparation, sample measurements and evaluation (LBIC, EQE), part in EBIC evaluation, part in writing.

Introduction

In 2015 the world's total primary energy demand was 13633 Mtoe (158552 TWh), of which renewable sources accounted for 1860 Mtoe (21632 TWh) or roughly 14%. Bioenergy accounts for the major share of around 71% of all renewables or about 9.7% of the total primary energy demand. In the same year the electricity production was 24240 TWh where renewables accounts for 5595 TWh and photovoltaics for 247 TWh, which is a share of 23% and 1% respectively [1]. Comparing the electricity production from photovoltaics (PV) to the total primary energy demand the share of photovoltaics is only around 0.16%.

Accounting for future developments such as demographics, economics, policies and price developments it is expected in the so called "New Policies Scenario" that the primary energy demand is growing in average by around 1% annually until the year 2040. The electricity generation is expected to grow even more by around 1.9% annually in average [1]. A growth in primary energy as well electricity generation is also expected in [2].

Although a prediction of future developments of the use of energy carriers is difficult, it is crucial to increase the share of renewables, whether because of finite fossil resources and nuclear fuels, externalized negative impacts of the same and risks of fossil or nuclear power plants and wastes, or to reduce greenhouse gas emissions, mainly carbon dioxide. In [3], the worldwide generation of electricity by photovoltaics is given with 443 TWh for the year 2017. The photovoltaic market is growing fast, with about 24% increase in average per year of PV-installations between the years 2010 and 2017. The market share of all thin film technologies, mainly copper indium gallium diselenide (CIGS) and cadmium telluride, accounts for only 5 %, while 95% of peak capacity is produced with crystalline silicon (c-Si) technology. This is despite that the efficiency of thin film photovoltaics is comparable to c-Si, the learning curves shows a bigger potential of cost reduction mainly due to economics of scale and the energy payback time is reduced by around 50 % [3, 4]. The highest conversion efficiencies of the commercially most common single-junction photovoltaic technologies are reported to be 26.7 % (monocrystalline silicon), 22.3% (multicrystalline silicon), 22.1 % (CdTe) [5] and 22.9 % (CIGS) [6].

Despite the big potential the current commercial CIGS and CdTe thin film technologies have to be utilized on a much bigger scale, there are concerns about the availability of large quantities of the rather rare metals used, mainly indium, gallium and tellurium. The possible production limits of photovoltaics due to scarce metals were investigated in literature [7-10]. The third widely commercialized thin film technology, which is based on amorphous silicon (a-Si), does not utilize these rare metals in the absorber material. Despite being one of the first thin film technologies on the market and decades of research, the conversion efficiency of a single junction cell is around 10% [5], which is rather low compared to c-Si, CdTe and CIGS devices.

The pentanary $\text{Cu}_2\text{ZnSn}(\text{S}_x\text{Se}_{1-x})_4$ -compounds (Kesterites) as p-type semiconductor materials have the potential to replace CdTe or CIGS as absorber materials in thin film photovoltaics, using earth abundant and non-toxic elements. In combination with an industrial and cost effective roll-to-roll (R2R) process utilizing the monograin technology [11], it could significantly contribute to a larger scale in the predicted and necessary increase in electricity generation from photovoltaics. For conventional Kesterite thin films conversion efficiencies of up to 12.6% were reported [12]. A certified conversion efficiency of up to 9.5% for Kesterite monograin devices with an active area efficiency of

around 12% was achieved [paper II]. Despite several beneficial parameters of this absorber material such as a high absorption coefficient, direct tunable bandgap and low temperature coefficients [13-15], the achieved efficiencies are still considerably lower compared to c-Si, CIGS and CdTe devices. Thus further research and knowledge is necessary to overcome the present limitations and improve the performance of the Kesterite based technologies generally and specifically the monograin technology further.

This PhD work aims at a better understanding of performance limiting processes and effects, and the development of analyzing methods to identify and evaluate them with the focus on spatially resolved investigations. Another focus was on the investigation and identification of ageing processes and the resulting stability of different Kesterite monograin devices.

The dissertation is divided into four main chapters, giving first a short overview of the literature and the aim of the study. In chapter 2 the experimental setup, including sample preparation and describing the analyzing methods used. The experimental results are presented in chapter 3, which are then furthermore discussed in there. Final conclusions are brought out in chapter four, based on the preceding results and discussions.

Abbreviations

CIGS	$\text{CuIn}_x\text{Ga}_{1-x}\text{S}_2$ or $\text{CuIn}_x\text{Ga}_{1-x}\text{Se}_2$
CIS	CuInS_2 or CuInSe_2
CZTS	$\text{Cu}_2\text{ZnSnS}_4$
CZTSe	$\text{Cu}_2\text{ZnSnSe}_4$
CZTSSe	$\text{Cu}_2\text{ZnSn}(\text{S}_x\text{Se}_{1-x})_4$ $0 < x < 1$
c-Si	Crystalline silicon
EBIC	Electron beam induced current
EL	Electroluminescence
EQE	External quantum efficiency
FF	Fill factor
FWHM	Full width at half maximum
j_{sc}	Short circuit current density
j/V	Current density/voltage
KP	Kelvin probe
LBIC	Light beam induced current
MGL	Monograin layer
PL	Photoluminescence
PV	Photovoltaics
R2R	Roll-to-roll
SEM	Scanning electron microscopy
TCO	Transparent conductive oxide
V_{oc}	Open circuit voltage
XPS	X-ray photoelectron spectrometry

1 Literature overview

1.1 Kesterite thin film and monograin layer solar cells

1.1.1 Kesterite absorber material

The investigations on Kesterites for photovoltaics started in the last century. Kesterite crystals are analogous to chalcopyrite copper indium diselenide (CIS) and can be derived from there by replacing indium by zinc and tin [16]. Already in 1988, Ito et al. manufactured pure sulphide $\text{Cu}_2\text{ZnSnS}_4$ (CZTS) samples by sputtering technique and proposed this material as a possible absorber material for photovoltaic applications. In there, the p-type conductivity and a high absorption coefficient larger than 10^4 cm^{-1} in the visible range of the spectrum of the material was published. Additionally a bandgap of 1.45 eV and a photovoltage of 165 mV under AM 1.5 illumination on a CZTS-cadmium-tin-oxide heterojunction sample was measured [13]. Nakayama et al. confirmed the p-type conductivity and investigated CZTS with different metal ratios. In there, also Cu on Zn and Sn antisites were proposed as acceptor levels [17]. The first fully functional CZTS photovoltaic cell with a conversion efficiency of 0.66 % was published by Katagiri et al. The absorber material was achieved by sputtering Cu, Zn and Sn followed by a sulfurization step with H_2S , and after depositing further layers an Al/ZnO/CdS/CZTS stack was achieved [18].

In these early publications, the authors stated that CZTS is formed in a Stannite crystal structure. However, later on it was shown that the material crystallizes preferably in the Kesterite structure [19-22]. The Kesterite and Stannite structures are very similar and it is very hard to distinguish between them with conventional X-ray diffraction measurements [19, 20, 22, 23]. It is proposed that the early identification of CZTS as Stannite crystal structure was due to partial disorder in the Kesterite structure [21] as well that Kesterite and Stannite structure may co-exist [23, 24].

The direct bandgap of CZTS was determined to be around 1.5 eV [25-34]. When replacing sulfur by selenium, forming pure selenide Kesterites (CZTSe), the bandgap is reduced to around 1 eV [34-40]. Historically, a large variation in bandgap energies have been published for CZTSe between 0.8 eV and 1.65 eV [25, 34-46]. Ahn et al. postulated, that the most likely reason for the measurements of bandgap energies for CZTSe at around 1.5 eV and therefor the big discrepancies between reported bandgap values is due to ZnSe binary compounds and confirmed that the bandgap of CZTSe is at around 1 eV [40]. By varying the S:Se ratio forming sulfur-selenide Kesterites (CZTSSe), the bandgap can be tuned between the values of CZTSe (1 eV) and CZTS (1.5 eV) [47-49]. With a bandgap between 1 eV and 1.5 eV, more than 95 % of the maximum theoretical efficiency for single junction devices can be achieved, which are 33.8 %, 33.4 % and 30.4 % at bandgaps 1.34 eV, 1.14 eV and 1.24 eV for the spectra AM 1.5G, AM 1.5D and AM 0 respectively [16].

In Kesterites, many different defects and defect clusters (vacancies, interstitials and anti-sites) are possible to be formed. An overview of these possible defects is given by Chen et al. [50]. The defects play an important role in Kesterites and its properties, e.g. they are responsible for the intrinsic p-type doping of the material, while certain defects also lead to a performance reduction of the material. While for CIGS copper vacancies (V_{Cu}) act as major acceptor levels and thus p-doping, in Kesterites Cu_{Zn} anti-sites have a lower formation energy than V_{Cu} and are believed to be the major defect which acts as acceptor [23, 50-53]. However, for certain non-stoichiometric compositions such as

copper poor and zinc rich materials, the formation energies change, resulting in a smaller formation energy of V_{Cu} and Zn_{Sn} and a higher formation energy for Cu_{Zn} and Sn_{Zn} , thus leads to V_{Cu} as dominating acceptor. Other acceptor defects than Cu_{Zn} and V_{Cu} such as V_{Zn} , Zn_{Sn} and Cu_{Sn} have a much higher formation energy and therefore have just a negligible influence on the electrical conductivity. The high formation energy of donor defects in the neutral state explains the intrinsic p-type conductivity of the Kesterite absorber material [50, 51]. Donor-acceptor compensation, forming defect clusters such as $[Cu_{Zn} + Zn_{Cu}]$ can lead to partial disorder of Cu and Zn when present as high population [50]. Such disorder was measured and reported by Schorr et al. [20, 21]. Since defect complexes, if present, are changing the conduction and valence band energies, bandgap fluctuations can occur. This is especially the case for complexes composed of deep level defects such as Sn_{Zn} , Sn_{Cu} , Cu_{Sn} and Zn_i . Additionally, deep defects decrease the short circuit current density (j_{sc}) by acting as recombination centers and decreasing minority carrier lifetime as well reduce the open circuit voltage (V_{oc}) [50, 54]. Since the rather deep defect Cu_{Zn} might not be optimal for high efficiency Kesterite materials, the shallower V_{Cu} acceptor defect might be beneficial [51]. This might be the reason why the majority of the reported composition necessary for high efficiency solar cells is Cu-poor and Zn-rich [23, 36, 55-61].

Since the first published CZTS solar cell device with a conversion efficiency of 0.66% in 1997 [18], there has been a continuous improvement over the last 2 decades. An overview of the reported efficiencies over time is given by Wang [62] and Kumar et al. [63]. The highest reported conversion efficiencies up to date has been 11.0 % [64], 11.6 % [65] and 12.6 % [12] for CZTS, CZTSe and CZTSSe respectively.

For the manufacturing, different vacuum and non-vacuum processes are possible and reported. The main process technologies are sputtering, evaporation, spray pyrolysis, spin coating, electrochemical deposition and nanocrystal synthesis by hot injection method [62, 63, 66-71]. The before mentioned manufacturing methods belong to the in here called conventional thin film technologies, with usually a rather homogenous absorber layer with a thickness of a few μm . The monograin technology [11, 72] and their monograin layer devices show some similarities and share many advantages with the conventional thin film technologies, however differ in many aspects. Therefore a more detailed historical overview about this technology will be given in the following chapter 1.1.2.

1.1.2 The monograin layer technology

The use of crystals or powders for semiconductor and photovoltaic purposes reaches far back in history. The start of PV applications with semiconductor power can be defined when a patent with its title "Large Area Solar Energy Converter and Method for Making the Same" was filed in 1957 and granted in 1959 by Hoffman Electronics Corporation and its inventor Maurice Elliot Paradise. In there, silicon particles with an approximate diameter of 2mm were used, achieved by grinding larger hyper pure silicon chunks, followed by an in-diffusion of an acceptor material for a certain distance. These particles were mixed with electrical insulating plastic material such as polyethylene and applied on a substrate. Part of the insulating material was etched on the surface and the p-doped layer was removed to expose n-type material. This was followed by the application of an electric contact material. By removing the substrate and selective etching on the opposite side, the p-type active surface was laid free and contacted to achieve the desired device structure. Already at this time one of the major goals stated in the patent

was the reduction of production costs compared to the standard manufacturing technique at this time [73].

Another major step in the history of powder based semiconductor devices was when the company Philips and the inventor Ties Siebold te Velde filed several patents in the field of utilization of semiconductor materials in powder form. Most notably from these is probably the patent with the title “Electrical monograin layers having a radiation permeable electrode”, filed in the year 1965. In there, the manufacturing of “monograin layers” with electric contacts, where at least one of them is radiation permeable, is described as well as their possible applications, for example for solar cells as stated: “Such devices are also useful for converting radiation energy into electrical energy, for example, a solar cell”. Additionally it is mentioned that the used grains can have different sizes, “However, in the manufacture of electrical devices according to the invention, grains are preferably used having an average diameter smaller than 100 microns, and preferably smaller than 50 microns” [74]. Hence the described technology resembles in many parts the nowadays produced Kesterite monograin layers as described in the experimental part in chapter 2.

Philips monograin layer technology was later used since the 1980s by researchers at Hamburg University working on photochemical solar energy utilization. Monograin membranes with CdS as active material were used to perform solar water splitting for the production of hydrogen and oxygen [75-78].

Already earlier in the 1970s, researchers at TalTech worked on the development of single crystalline semiconductor powder [79, 80] and later on the monograin layer technology for the manufacturing of electromagnetic radiation sensitive sensors [81-82]. Their work on monograin layers continued with the focus on solar cell applications. First chalcogenides such as CdSe and CdTe were utilized as semiconductor material [83-86], later CIS and CIGS [87-91] and then Kesterite material [14, 35, 92-95].

In 2007 crystalsol OÜ was founded as a spin off company from Tallinn University of Technology (nowadays TalTech) and one year later crystalsol GmbH. In these companies the monograin technology based on Kesterite powders is utilized and further developed, where the focus of crystalsol OÜ lies on the production of the semiconductor powders while crystalsol GmbH focuses on the utilization of these powders in a cost effective and industrial R2R process. A pilot R2R production line was installed at crystalsol GmbH in Vienna, Austria. Up to now, the highest certified conversion efficiency achieved with this process is 9.5% [paper II].

1.2 Spatially resolved opto-electrical evaluation methods for solar cells

Several spatially resolved investigation techniques such as light beam induced current measurements (LBIC), electron beam induced current measurements (EBIC), photoluminescence and electroluminescence imaging, (lock-in) thermography and others are commonly used for the analysis of photovoltaic devices. In this thesis and the corresponding papers mainly two of them, LBIC and EBIC, are intensively used, hence in this chapter a compact literature overview with the emphasis on these two technologies is given.

1.2.1 LBIC

LBIC measurements is a classical analysis technique and frequently used for spatially resolved investigations of semiconductor devices. Hereby the surface of the investigated sample is scanned by a light spot and the generated photocurrent is measured.

While LBIC measurements are accurate, measurements are often rather slow and time intensive. The measurement speed is basically affected by 3 factors, which are the scan rate, the acquisition time per measurement point and the total number of measurement points which is determined by the investigated area and the resolution. By using continuously moving x-y-stages, the scan rate can be increased so that it does not seriously contribute to the limitations of the measurement speed anymore [96-98]. LBIC measurements can be conducted with different light wavelengths, various light intensities, bias light and applied voltages [97-101]. Additionally, spatially resolved spectral response measurements are possible [102]. A scheme of an advanced LBIC measurement setup which the authors named "CELLO" and a description of this technique with the possibility to extract additional cell parameters next to the photocurrent which allows the calculation of spatially resolved current density/voltage (j/V) curves can be found in a paper by Carstensen et al. [101]. A scheme of a more conventional LBIC measurement setup, which resembles the basic principles of LBIC measurements can be seen in figure 2 in a paper by Kaminski et al. [103].

The use of LBIC for different investigations is reported for solar cells with various absorber materials such as crystalline silicon [101, 104-108], amorphous silicon [98, 109], CdTe [102], CIGS [110], dye sensitized and polymer solar cells [96, 111-113], Kesterites [99, 100, 114] and other semiconductor devices such as photodiodes, photoresistors [112, 115] and integrated circuits [116].

LBIC measurement systems are usually utilized for mainly two purposes, for the determination of the photoactive area of a device and the evaluation of the photocurrent related local homogeneity of a device. While the former one is used to allow a more precise evaluation of the conversion efficiency and the related solar cell parameters as shown by Jones et al. [111], the latter is used in correlation with several possible subjects of interest. Examples from literature which lead to inhomogeneities observed by LBIC measurements are different Na-concentration in CZTS [114], defects, shunting and interconnection problems in amorphous silicon modules [98], CdS layer thickness variations [99, 100], carrier diffusion lengths and recombination mechanism in the bulk, grain boundaries and interfaces in polycrystalline silicon devices [105, 106, 117, 118].

For Kesterite monograin photovoltaic devices, just few LBIC utilizations and investigations are reported in literature. Mellikov et al. reported the use of LBIC for the identification of the "active area" of a single Kesterite monograin, from which the "material efficiency" of this grain could be extracted [72]. Here the "active area" is the contact area of the grains with the front contact, since the area in between the grains or the area of the grains covered by polymer are not active in generating photocurrent. So only a part (70-85 %) of the solar cell is active. In order to compare monograin layer (MGL) results with those of thin film devices, in which 100% of the cell area is active, the "material efficiency" allows a better comparison of the materials quality.

A first thorough investigation by means of LBIC of Kesterite monograin layer devices was conducted by Lehner. In there, two Kesterite MGL devices with different conversion efficiencies were investigated and principles of the influence of focus settings, illumination intensity and background illuminations were investigated. Additionally a correlation between conversion efficiency and photocurrent homogeneity could be seen with a higher degree of inhomogeneity correlating to a reduced solar cell performance [119].

1.2.2 EBIC

EBIC measurements resemble in many cases the LBIC measurement technique, but instead of (focused) electro-magnetic radiation an electron beam is used as excitation source. This results in a usually smaller penetration depth of the electron beam compared to the light beam in LBIC systems. The big advantage of EBIC over LBIC is that higher mapping resolutions are possible [103]. A comprehensive review of the EBIC measurement technique can be found in papers by Leamy and Scheer [120, 121]. EBIC measurements can be used for plan view, measured on the front side or back side of a sample [122-124], as well as cross-section investigations [12, 125]. Plan view measurements are commonly utilized to determine local uniformity of the current response of a device similar as for LBIC investigations and to detect defects [122]. Temperature dependent defects were investigated by means of EBIC by Breitenstein et al. on silicon cells. Additionally conductive and shunting channels through a device caused by SiC precipitates could be identified [123]. Scheer et al. determined the diffusion length of the charge carriers by varying the beam energy and therefore the penetration depth while measuring the correlated collection efficiency [124]. The diffusion length, depletion width or space charge region is more often investigated by cross-section measurements. Wang et al. investigated a sister device of their record CZTSSe sample with EBIC. From these measurements they concluded a rather homogenous collection width of around 1 μm . This collection width is said to be roughly the sum of the depletion width and the diffusion length [12].

Depending on the acceleration voltage, the penetration depth of the electron beam is different, as depicted in figures 1 and 2 in [102]. This is especially of importance if a high surface recombination of the investigated sample is present, since it influences the carrier lifetime and collection and is dependent on the penetration depth as shown by Nichterwitz et al. [126]. One possibility to reduce the surface recombination was shown by Bissig et al. In there the authors showed that a thin layer (few nm) of Al_2O_3 deposited by atomic layer deposition on the cross-section surface reduces the surface recombination and enhances the EBIC signal significantly [127].

Just a few reports on the utilization of EBIC measurements on MGL photovoltaic devices can be found in literature. The use of EBIC for the identification of active grains or the active surface is reported for MGL devices with CdTe monograins [128, 129] and CuInSe_2 monograins [90]. In [130], Mellikov et al. utilized EBIC measurements for the determination of the local efficiency homogeneity of a CZTSSe MGL device.

1.3 Ageing and degradation mechanism of photovoltaic devices

International standards for measurements of photovoltaic modules are published by the International Electrotechnical Commission. While there is no standard for the Kesterite technology available, a standard can be found for CIGS, which is closest to the Kesterite material, in IEC 61215-1-4 [131], which directs to the testing standard IEC 61215-2 [132]. In there, various testing standards are described, including test for the stability of modules such as thermal cycling and humidity-freeze tests. In the damp heat test description, conditions which are required are a temperature of 85 ± 2 °C, a relative humidity of 85 ± 5 % and a test duration of 1000 to 1048 hours.

Ageing or degradation of Kesterite photovoltaic devices is just poorly covered in literature. A model for the decomposition of CZTS thin films was proposed by Yin et al. Additionally a Cu-Zn separation was observed when applying a directional heat with a heat plate. These investigations were carried out at temperatures between 623 K and

873 K [133]. Due to the relatively high temperatures far higher compared to the temperatures as required in the above mentioned standard or the temperatures used in this thesis, the published results of Yin et al. are hard to utilize and to compare with ageing mechanism occurring at lower temperatures.

The stability of CZTS with different window layers was tested with damp heat treatment and accelerated thermal cycling by Peng et al., based on the standard IEC 61646, which was replaced by the standard IEC 61215-1-4 mentioned above [134]. Degradation related modeling of V_{OC} and j_{SC} of perovskite and other thin film technologies including Kesterites were carried out by Darvishzadeh et al. [135, 136].

1.4 Aim of the thesis

Research of literature shows that Kesterites as a semiconductor absorber material and its utilization in photovoltaics can have an important role for future PV applications. The monograin layer technology is one way to utilize this material in a cost effective, industrial and competitive way. Research in the last years gave more insight in understanding the properties and led to significant improvements of this technology. Nevertheless further research and development is needed to improve the absorber material as well as the device manufacturing further. In addition, ageing or degradation processes are just very poorly covered in literature, despite its importance for a successful industrial implementation of Kesterite thin films or MGL photovoltaics.

Hence in this thesis the main aims are:

- The development and evaluation of methods for spatially resolved opto-electronic investigation techniques with the focus on LBIC. As outcome the used methods should be described and evaluated regarding prospects for further investigations of solar cells.
- The utilization of spatially resolved opto-electronic investigation techniques on Kesterite MGL devices. The focus hereby lies on the detection and identification of performance reducing effects. As outcome different performance reducing effects are investigated and evaluated with the goal of identifying the cause.
- The investigation of ageing effects in Kesterite material and MGL solar cells. The aim hereby is the identification of ageing processes and their evaluation and description by different analysis methods, including the utilization of spatially resolved opto-electronic investigation techniques such as LBIC and EBIC. The findings should build a fundament for further investigations on this topic.

2 Experimental

2.1 Sample preparation

2.1.1 Monograin synthesis

Two pure sulphide monograin powders and four sulfur-selenide powders with a sulfur to selenium ratio of 4:1 and 3:2 are investigated in this thesis. The monograins are synthesized from copper, zinc sulphide, tin and sulfur for CZTS and in addition zinc selenide for CZTSSe in potassium iodide as flux material in quartz vessels in a furnace above 700°C for different durations. After the synthesis the powder is washed with water which dissolves and removes the KI. After drying, a sieving procedure separates grains of different sizes to obtain the desired grainsize between 56 and 90 µm. This is followed by a heat treatment step at 740°C at low vacuum (CZTSSe) or in a sulfur atmosphere (CZTS). Cadmium sulphide as buffer layer is deposited on the grains by chemical bath deposition, employing cadmium acetate and thiourea in an ammonia solution. After additional drying the semi-finished product of monograin powder (Figure 1) is obtained, where each grain has a fully functional p-n-junction. The investigated powders are produced and provided by crystalsol OÜ, Akadeemia tee 15a, 12818 Tallinn, Estonia.

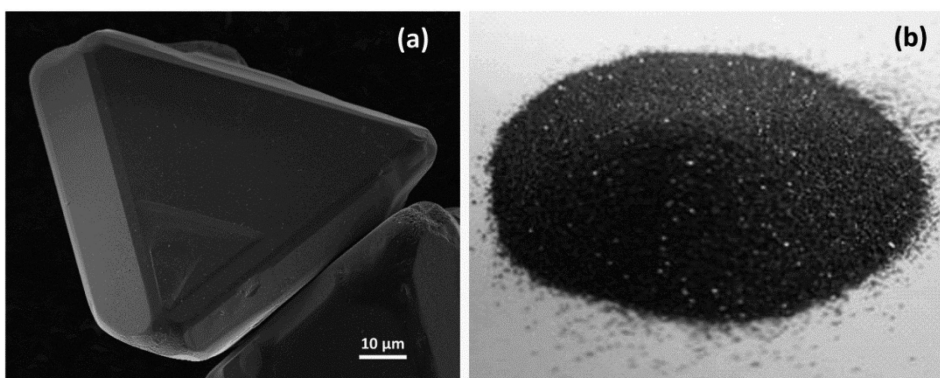


Figure 1 SEM image of a Kesterite crystal (a) and an optical image of Kesterite monograin powder (b) [137]

2.1.2 Device fabrication

For the production of PV devices a thin layer of polymer, Buehler EpoThin 2 Resin and Hardener, Lake Bluff, IL, USA, is applied on a substrate foil by doctor blading, forming the membrane polymer layer. The thickness of the polymer layer is aimed to be around 30% of the average diameter of the used monograins. The monograin powder is applied on top of the polymer, where by adhesion, due to the contact of grains to the semi-cured polymer, a single layer of grains is formed. The excess powder, which is not sticking to the polymer can be shook of and reused in future. By gravity and additional applied pressure the monograins are embedded partially into the polymer, leaving around half of the grain surface open and uncovered, which forms the so called monograin layer (Figure 2).

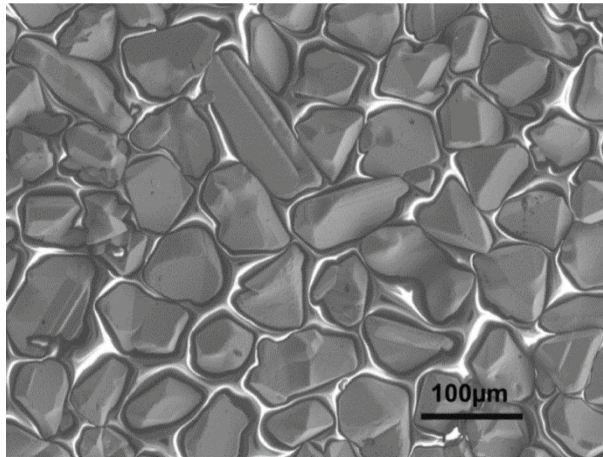


Figure 2 SEM surface image of a MGL, produced by partially embedding of monograins into polymer

After full curing of the polymer, a transparent conductive oxide (TCO) layer, consisting of intrinsic and aluminum doped zinc oxide is deposited by radio frequency sputtering on the front side of the MGL. To increase the electric conductivity of the front contact, a thin layer of silver nanowires is applied on top. Additional front current collector stripes are applied by silver paint, Electrolube/HK Wentworth Ltd., Ashby de la Zouch, UK. Following this, the MGL is glued with transparent polymer (Buehler EpoThin 2) to a soda lime glass to seal the front side. After curing of the sealing polymer, the initial substrate foil can be peeled off and removed. By dipping the device into concentrated sulfuric acid, part of the membrane polymer on the backside is etched away and the embedded monograins are partially laid free. The back side is treated with a mechanical abrasive process with sandpaper to open the grains, which ensures a good Ohmic contact to the back contact material. This back contact material, which is aqueous based electrically conductive graphite paint, Alfa Aesar, Ward Hill, MA, USA, is applied to the back side which forms the finished back contact after drying. To be able to access the electric front contact, a hole is drilled into the MGL and filled with silver paint, which establishes the front contact for measurements and finishes the device production. A cross-section scanning electron microscope (SEM) image and a scheme thereof of such a finished PV-device can be seen in Figure 3 below.

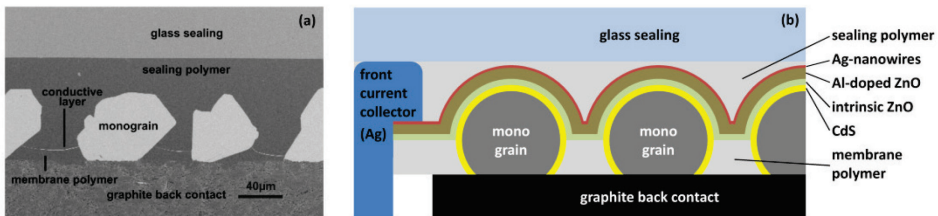


Figure 3 Cross-section SEM image (a) and a scheme (b) (not to scale) of a finished MGL photovoltaic laboratory device as used for the analysis conducted in this thesis

The above described device manufacturing is used for standard laboratory PV-devices. For certain investigations, the device structure has to be altered. For devices which are produced for investigations by means of EBIC measurements, the insulating sealing polymer is mixed with small electric conductive metal pieces.

This ensures a reduction of disturbing charging effects during measurements. For being able to measure the cross-section of the sample, the PV-device is mounted into Buehler EpoThin 2 polymer, and after curing the sample is polished by using a Bühler Ecomet 250 polishing apparatus.

For the j/V investigations of the Kesterite-back contact interfaces during ageing, a MGL is abraded with sandpaper on the front side after embedding of the monograins and curing of the membrane polymer. After that the front side is covered with graphite paint and after the graphite paint is dry the MGL is glued with polymer to the soda lime glass. The finishing of the backside follows the same procedure as for the standard manufacturing. Such fabricated devices form a carbon-Kesterite-carbon (C-Kesterite-C) structure. Such C-Kesterite-C devices are also used for investigations by X-ray photoelectron spectrometry (XPS) and Kelvin probe (KP) measurements.

2.1.3 Device ageing

For the investigations how the devices with different materials behave during ageing, the samples undergo an accelerated ageing procedure at elevated temperature. For that the devices are put into a furnace at 105 °C for various durations. The atmosphere is air and a desiccant is added to provide low humidity conditions.

2.2 Analysis methods

2.2.1 Current density/voltage measurements

The j/V measurements are performed with a Keithley 2400 Source Meter, Keithley Instruments Inc., Cleveland, Ohio, USA, with a 2-wire measurement setup (PV-devices) or a 4-wire measurement setup (for C-Kesterite-C devices). The voltage is applied between different ranges and with different increment steps, while the current is floating and measured. The illumination source for measurements under light conditions is provided by a Philips Broadway halogen lamp, 250 W, 24 V, operating at 21V (papers I and II) or a Newport Oriel AAA-class sun simulator, Newport Corporation, Stratford, CT, USA (papers III and IV). All measurements are carried out at ambient conditions.

The certification measurements (paper II) are carried out by FhG ISE, Freiburg, Germany, Certificate-Nr. 1001076CRY0317, March 24, 2017.

2.2.2 External quantum efficiency and wavelength dependent transmission measurements

The external quantum efficiency (EQE) and wavelength dependent transmission measurements are carried out by means of a Newport Oriel 300W Xenon lamp with a Cornerstone 260 Monochromator, silicon detector and a Merlin radiometer system, Newport Corporation, Stratford, CT, USA. The quantum efficiency and transmission is measured between the wavelengths 350 nm and 1000 nm in 10 nm increments.

2.2.3 Light beam induced current measurements

The LBIC measurements are conducted with a red (633 nm) laser and a lock-in amplifier with a scanning rate of around 10 measurement points per second. The laserspot diameter, evaluated similar as in [138, 139], is determined to be around 5 μm . The excitation laser intensity is adjusted with spectral neutral grey filters, which reduces the intensity to around 0.013 μW and 0.08 μW for the LBIC measurements conducted. The steplength, which results in the resolution of the LBIC image, is chosen between 1 μm and 5 μm , depending on the measurement area. The LBIC measurements result in a datamatrix. This datamatrix can be used to construct an image, which for this thesis is

done with the program Matlab, or for additional statistical analysis and evaluation, for which the programs Matlab, Microsoft Excel, Microsoft Access and Origin are used.

2.2.4 Scanning electron microscopy and electron beam induced current measurements

The majority of the SEM analyses are conducted by a Zeiss ULTRA 55, Carl Zeiss Microscopy GmbH, Jena, Germany instrument. The measurements are performed by Mr. Ali Samieipour and Dr. Valdek Mikli, TalTech.

The cross-section electron beam induced current investigations are conducted with the same instrument by the same operators.

Additionally a JOEL JSM-7600F field emission SEM, JEOL Ltd., Akishima, Japan as well as a Hitachi TM-1000, Hitachi High-Technologies Corporation, Minato-ku, Japan is used for some of the SEM analysis.

2.2.5 Raman and photoluminescence spectroscopy

A Horiba Jobin Yvon Labram HR800 instrument, Horiba Ltd, Kyoto, Japan, with a CCD detection system is used for Raman spectroscopy measurements. As excitation source a green laser (532 nm) is utilized, adjusted with spectral neutral grey filters to a light intensity of around 2.8 mW.

The same system and excitation source is used for photoluminescence (PL) spectroscopy, with an exposure time of three seconds. The detection range is set to be between 1.1 eV and 1.8 eV.

2.2.6 Electroluminescence

Electroluminescence (EL) spectra measurements are carried out with applied voltages between 1.2V and 2V and floating currents. The EL emission is detected by the CCD detection system from the Horiba Jobin Yvon Labram HR800 instrument between 1.1 eV and 1.8 eV. The accumulation time is set to 30 seconds.

For the EL imaging an Andor iKon M camera, Oxford Instruments plc, Abingdon, UK is utilized. The measurements are conducted with a current density of 200 mA/cm² and an accumulation time of 30 seconds.

2.2.7 X-ray photoelectron spectrometry

The elemental composition of the Kesterite samples are studied by Kratos AXIS Ultra DLD X-ray photoelectron spectrometer using a monochromatic Al K α X-ray source at 150W. The detailed XPS spectra of core levels are recorded at 20eV pass energy using the aperture slot of 300 \times 700 μ m. The surface composition is determined from the detailed spectra of the Zn 2p, Cu 2p, and Sn 3d. The relative atomic concentrations are determined from the appropriate core level integrated peak areas and sensitivity factors provided by the Kratos analysis software Vision 2.2.10. The measurements are conducted by Dr. Mati Danilson, TalTech.

2.2.8 Optical microscopy

Optical microscope images are taken with a Nikon SMZ 745T optical microscope, Nikon Corporation, Tokyo, Japan.

2.2.9 Kelvin Probe measurements

Workfunction measurements are conducted with a scanning Kelvin probe measurement system, KP Technology Ltd., Wick, UK. The measurements are conducted with a gold probe at ambient conditions.

In Table 1 below all produced and investigated samples are shown, with a summary of some material parameters and the analysis methods which are used for the investigations presented in this thesis.

Table 1 Summary of investigated samples in this thesis.

sample name	S:Se ratio [a.u.]	av. grain size (range) [μm]	analysis methods	papers
sample 1	4:1	69 (63-75)	j/V, SEM, LBIC, PL, EL, Raman, transmittance	I, II
sample 2a	4:1	85 (80-90)		
sample 2b	4:1	85 (80-90)		
record	3:2	72 (63-80)	j/V, LBIC	II
CZTS semi-stable	1:0	68 (56-80)	j/V, SEM, XPS, PL, EQE, LBIC, EBIC, KP	III, IV
CZTS unstable	1:0	68 (56-80)		
CZTSSe semi-stable	4:1	68 (56-80)		
CZTSSe unstable	4:1	68 (56-80)		

3 Results and discussion

3.1 Development of new analysis methods of spatially resolved photocurrent measurements

The production of PV-devices with Kesterite monograins result in semi-transparent MGLs since the monograins do not cover the whole total area and leave empty spaces between the grains. This semi-transparency is seen in Figure 4, where the transmittance of a MGL and an empty polymer layer is shown. While the transmittance of the polymer layer is wavelength independent at around 95%, the MGL shows a transmission between 13 % and 14% in the wavelength range 350 nm to around 880 nm, as indicated by the tilted straight dashed line. 880 nm (1.41 eV) corresponds to the bandgap, this is why the transmittance is increased from this wavelength on to higher wavelengths. This uncovered area between the grains is an inactive area during j/V measurements of PV-devices and thus reduces the derived j_{sc} . However it also provides the possibility to make a device or module semi-transparent.

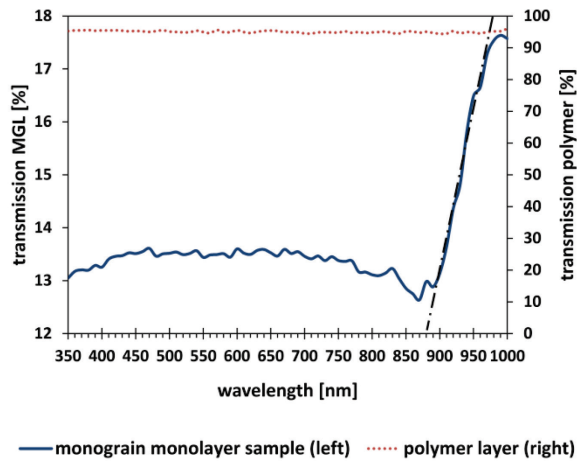


Figure 4 Transmission measurements of a MGL sample and of an empty polymer layer. The tilted dashed vertical line indicates the bandgap.

Although empty spaces between the monograins is the major reason for the reduction of active area which contributes to the current generation, also grains or part of grains can be inactive. This can be the case due to a missing front or back contact. This can be seen in Figure 5, where in part (a) on the left a constructed image of LBIC measurement data, in part (b) in the middle a superposition of LBIC and SEM image and in part (c) on the right a superposition of LBIC and transmission image is presented. These images represent a small area of sample 2b. From there inactive grains due to a missing back contact are seen, indicated as example by the solid circle. Such grains give no LBIC response but are seen in the SEM image and the transmission image. It is also possible that grains or parts of grains are inactive due to a missing front contact. Such an inactive part of a grain is indicated as an example by the dashed circle in Figure 5. Such parts are covered by the electrically insulating but optically transparent polymer, that's why they don't have an electric contact and do not give a LBIC response, are not visible in the SEM

image but are visible in the transmission image. Such partially or fully inactive grains reduce the active area and thus the current response during j/V measurements further and can be one possible reason for a low performance of MGL photovoltaic devices.

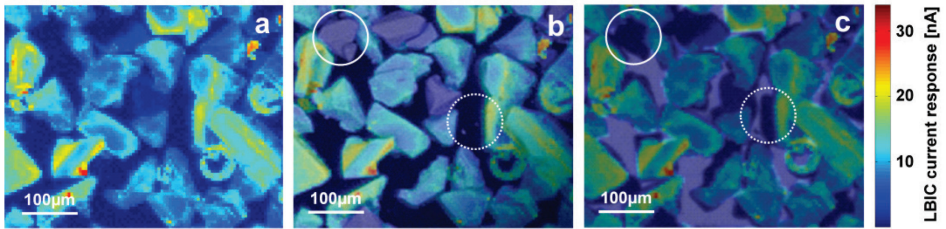


Figure 5 LBIC (a) and superposition of LBIC and SEM image (b) and LBIC and transmission image (c) of an excerpt of sample 2b. The solid circle indicates an inactive grain without back contact, the dashed circle a part of a grain which is inactive due to a missing front contact.

To evaluate the LBIC response from different areas further, the LBIC measurement values are plotted with the current value in descending order, as it is seen in Figure 6. In this graph four distinctive areas can be defined. The “peak area” represents LBIC measurement values from highly efficient areas, the “main active area” correspond to the majority of the measurement response from the active area, the “border area”, which consist of measurement points where the laser spot is just partially on the active grain, and the “inactive area” corresponding to measurement values from areas without absorber material or inactive absorber material. The small current response from the inactive area is due to reflection of part of the excitation light from the inactive area to nearby (active) grains. The peak area and the main active area can be also combined to the “active area”, as it is done for some of the analysis later in this thesis if the distinction between these two areas is not of significant interest.

In Figure 7 constructed images with the defined areas from the measurement data of Figure 6 are shown. The exact position of the border area is arbitrary to a certain extent. However, when defining 3 different border areas which differ each by a factor of approximately 2 in Figure 6 and the corresponding images in Figure 7, it becomes visible that border area “a” (Figure 7a) leads to an overestimation of the area due to response values which can be clearly attributed to the inactive area. The border area “c” (Figure 7c) on the other hand leads to a border area thickness below the laser spot size and is thus clearly underestimated. Therefore the border area “b” (Figure 7b) represents a realistic estimation of the width.

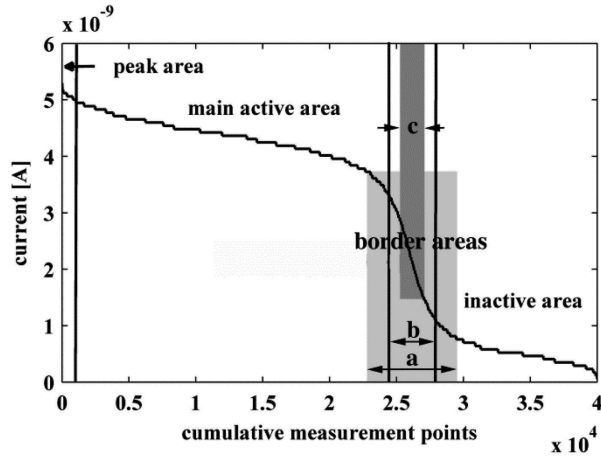


Figure 6 Definition of characteristic areas of a small area of sample 1, where all measurement points are counted with the corresponding current response in descending order. The different definition widths of the border area are indicated as a, b and c and correspond to the parts a, b and c in Figure 7.

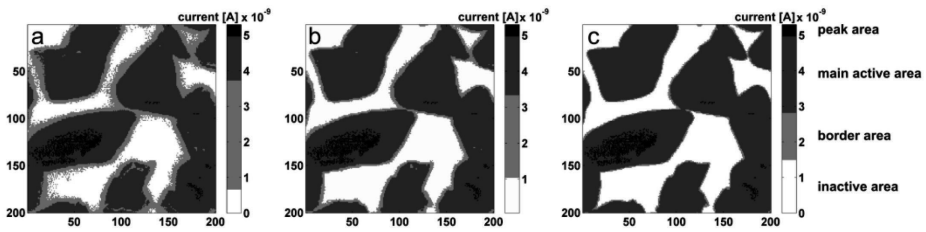


Figure 7 Constructed LBIC images of the small area of sample 1 evaluated in Figure 6, with a scale divided into characteristic areas (see text). The data correspond to the measurement values presented in Figure 6. The units of the axis are measurement steps with a set step width of $1\mu\text{m}$.

From these defined areas the active area ratio (AAR) can be derived by the equation 1 below, where n_p is the number of measurement points of the peak area, n_m the number of measurement points of the main active area, n_b is the number of measurement point of the border area and n the total number of measurement points. The defined width of the border area affects the AAR just to a minor extent. For the example shown in Figure 6 and Figure 7 with a big variation of the defined border area the difference of the ARR is just 0.2 percent points. By the AAR the effects of inactive areas due to empty spaces or inactive absorber material can be quantified.

$$AAR = \frac{n_p + n_m + n_b/2}{n} \times 100 \% \quad (1)$$

The width of the border area is dependent on the laser spot size as well the average monograin size of the absorber material. The correlation of the border area and the number of measurement points within and the utilized grain size can be explained by the non-linear ratio of the circumference and the diameter of the grain polygons.

Additionally the slope of the curve as in Figure 6, consisting of measurement points of the main active area or generalized active area, correlate to the homogeneity regarding the current response of these areas during measurements, where a steeper slope means a more inhomogenous current response. The homogeneity of the measured areas is best seen in the “homogeneity plot” (current density distribution), introduced in the right part of Figure 8 below, where the measurement data of the record CZTSSe MGL device is presented. The main peak at high current values represent the measurement points of the active area, while the (small) peak at low current values consist of the measurement point of the inactive area, where the small current response comes from reflected light onto active material. The main peak has a gaussian like shape and can be fitted with a gaussian curve, as it is seen in the inset of the right part of Figure 8. From this curve statistical values such as the full width at half maximum (FWHM), peak position and peak height can be extracted. While the peak position can be correlated to the average current response of the active area, the FWHM and peak height is a good indicator for the homogeneity of the active area regarding the LBIC current response. The record device shows hereby a remarkable high photocurrent homogeneity of around $\pm 3\%$.

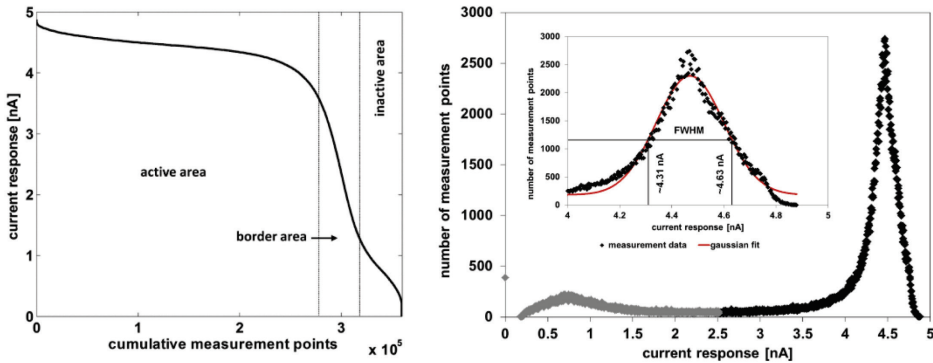


Figure 8 Statistical analysis of the LBIC measurement data of the record device, presented as cumulated measurement points with corresponding current response in descending order (left) and the homogeneity plot (current density distribution) of the measured points (right). The inset shows only the active current peak with a Gaussian fit thereof. In the right image the black filled markers correspond to measurement points of the active area while the grey filled markers correspond to measurement points from the inactive area where the current is generated by reflected light.

3.2 Application of spatially resolved investigations on MGL solar cells by means of LBIC

In Table 2 below the most important solar cell parameters, derived from j/V measurements of three CZTSSe MGL devices, are presented. As seen there, the values of sample 2a and 2b are lower compared to sample 1, specifically with a big difference in j_{sc} . To investigate, whether the much lower j_{sc} of samples 2a and 2b is a result of a lower packing density or inactive absorber material resulting in a lower active area, or if other reasons can be assigned for these big differences, the analyzing method as shown in chapter 3.1 is applied for this devices. The measured area size and number of measurement points are the same for all three samples.

Table 2 Solar cell parameters derived from j/V measurements of differently efficient CZTSSe MGL devices.

sample	area [mm ²]	V _{oc} [V]	FF [%]	j _{sc} [mA*cm ⁻²]	efficiency [%]
sample 1	3.9	0.688	55.8	15.6	6.0
sample 2a	4.29	0.643	41.3	9.05	2.4
sample 2b	2.39	0.629	42.8	7.07	1.9

Analyzing the plotted curves of the LBIC measurement data in Figure 9, where the measurement values are plotted in descending order and divided into active, border and inactive area, similar as in Figure 6 or the left part of Figure 8, certain observations can be made. The curves of sample 2a and 2b show clearly a lower LBIC current response. The defined border areas indicate that the AAR is rather similar between sample 1 and sample 2a while the ARR of sample 2b seems to be bigger since the border area is shifted to the right. Additionally the width of the border area of sample 1 appears to be bigger compared to sample 2a and 2b. The AAR and the width of the border areas (expressed as number of measurement points of which the defined border area exists of) are extracted and presented in Table 3. These values confirm the above mentioned observations from the visual evaluation of the curves. A correlation between the number of measurement points of the border area and the grain size (sample 1 consist of monograins of smaller size, thus a wider border area can be expected) can be seen, as it was proposed in chapter 3.1. Comparing the slopes of the curves in Figure 9, the current response of sample 1 appears to be more homogenous compared to sample 2a and 2b. This can be also observed in the homogeneity plot in Figure 10. The FWHM, extracted from these homogeneity plots and presented in Table 3 confirms this, with sample 2a and 2b having clearly higher FWHM than sample 1 and are thus more inhomogeneous regarding the current response.

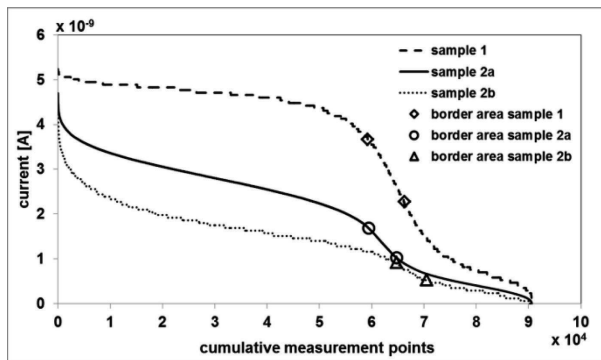


Figure 9 Cumulative measurement points of LBIC measurements on samples 1, 2a and 2b with indicated border areas.

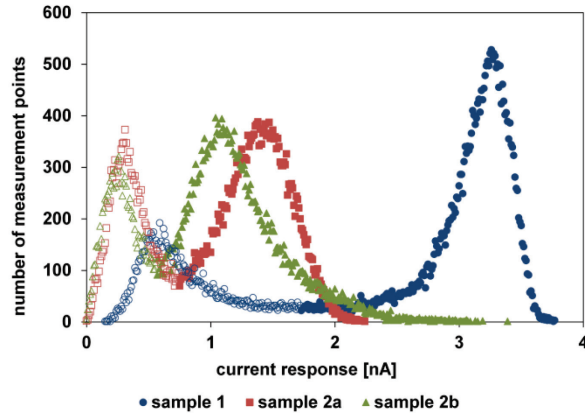


Figure 10 Homogeneity plot (current density distribution) of the LBIC current response of samples 1, 2a and 2b. The filled symbols correspond to measurement points on the active area of the grains, while empty markers correspond to measurement points of the inactive area with the current being generated in the surrounding grains by reflected light.

Table 3 Extracted parameters from the LBIC measurements of sample 1, 2a and 2b.

sample	av. grain size [μm]	AAR [%]	number of meas. points of border area	FWHM [nA]	FWHM [%]
sample 1	69	69	7027	0.46	6
sample 2a	85	68	5333	0.65	20
sample 2b	85	75	5684	0.62	25

From the analysis of the LBIC measurements above it becomes clear that a difference in active area, expressed as the AAR, is not the reason for the high difference in j_{sc} of the investigated devices. Instead the absorber material of sample 2a and 2b shows a general lower current response, with additionally very high inhomogeneity, which are suspected as the major cause for the reduction of the solar cell parameters, especially j_{sc} .

3.3 Identification of reasons for inhomogeneities and performance reducing effects

To investigate the inhomogeneity of the LBIC current response further, additional opto-electric measurement techniques such as EL imaging and EL as well as PL spectra measurements are employed on sample 2b. In Figure 11 a constructed LBIC image (a) and an EL image (b) of a nearly identical area of sample 2b are shown. While in both images a high degree of inhomogeneity can be observed, the LBIC response is inversely correlated with the EL response. Grains or areas of grains with high LBIC response show a low EL response, and vice versa. Examples for such grains are given in Figure 11, indicated by dashed circles and named grain A (high LBIC, low EL) and grain B (low LBIC, high EL) respectively.

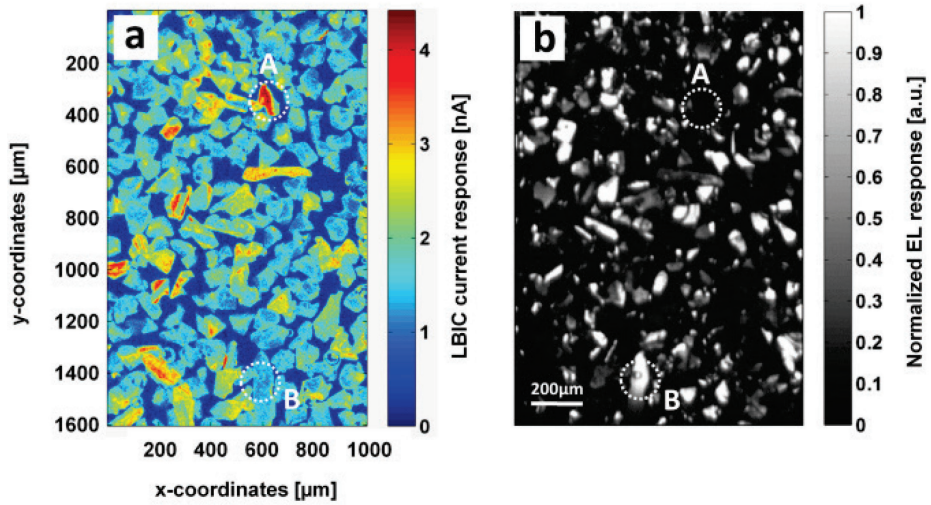


Figure 11 LBIC (a) and EL (b) image of sample 2b. PL and EL spectra of specific grains indicated by dashed circles are seen in Figure 12.

From the same grains (grains A and B) as indicated in Figure 11, EL and PL spectra measurements are conducted, which are seen in Figure 12. From there a direct correlation between PL and EL response is visible, where grain A shows a lower EL and PL response (seen from the peak height) compared to grain B. The shape of the peaks, which are broad and unsymmetrical, indicate different emission energies, however look similar for grain A as well for grain B. It is clearly visible, that the peak position of the EL emission is at lower energies compared to the peak position of the PL emission. It is reported in literature, that an ordering-disordering effect can cause a peak shift for PL spectra measurements, with more ordering of CZTS leads to higher emission energies [140, 141]. However, grain A as well grain B show similar peak positions, either at higher energies (PL) or lower energies (EL), which does not support a different degree of ordering. The difference of the emission energies between PL and EL measurements can be explained by the fact that the photon flux intensity during PL measurements was around four orders of magnitude higher than the average current density during EL measurements. Such intensity dependent emission energy shifts are also reported in literature for PL measurements [141, 142].

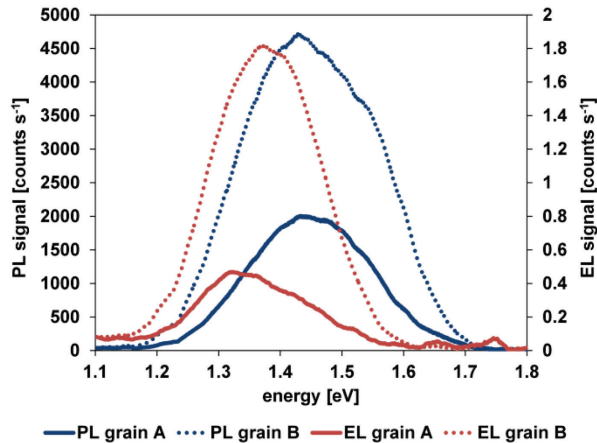


Figure 12 PL and EL spectra of grains of sample 2b indicated by the circles given in Figure 11.

Both grains are investigated by Raman spectroscopy, where the spectra are seen in Figure 13. The spectra from both grains look very similar, with clear peaks, which can be attributed to CZTSSe and are indicated in the Figure. It has to be mentioned, that the Raman measurements are conducted on fully functional PV-devices with additional layers on top of CZTSSe such as CdS and TCO as described in the experimental part, thus small additional responses beside the ones from CZTSSe can be attributed to this additional layers.

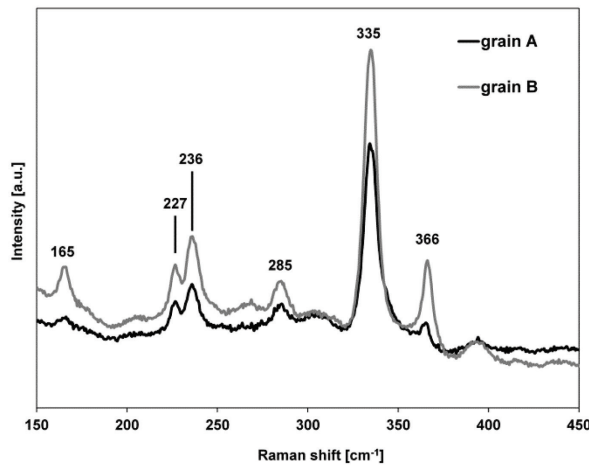


Figure 13 Raman spectra of grain A and grain B of sample 2b. The two measured grains are seen and indicated by dashed circles in Figure 11 and are analyzed by PL and EL spectra in Figure 12. The indicated peak positions in the Raman spectra correspond to CZTSSe.

In addition to whole grains which show a big difference in LBIC response and EL and PL emission, some grains show a distinctive pattern in LBIC and EL images. Such a grain is displayed in Figure 14, where in part (a) a SEM image is presented, which shows the grain with certain planes. These planes can be also identified in the EL image (Figure 14b) and LBIC images (Figures 14c and 14d) due to their difference in response.

As already observed before, the LBIC and EL response is inversely correlated, with areas which show high LBIC have low EL response and vice versa. While the LBIC image in Figure 14c is constructed from measurement data where the excitation laser beam is perpendicular to the sample, the sample was tilted around 18° in Figure 14d. This leads to the conclusion that the different measurement response of the different planes is not due to their orientation towards the laserbeam and is incident angle independent. From three different spots (spot C, D and E) on the analysed grain, which are indicated in Figure 14a as dashed circles, PL and EL spectra measurements are conducted, which are seen in Figure 15. From these spectra measurements the same observations can be made as for the spectra in Figure 12. From this it can be concluded that the reasons for the inhomogenous response of all three opto-electric measurement techniques as well as the invers correlation between LBIC and EL respectively PL signal is the same, whether they appear on full grains or just certain parts or planes of the monograins.

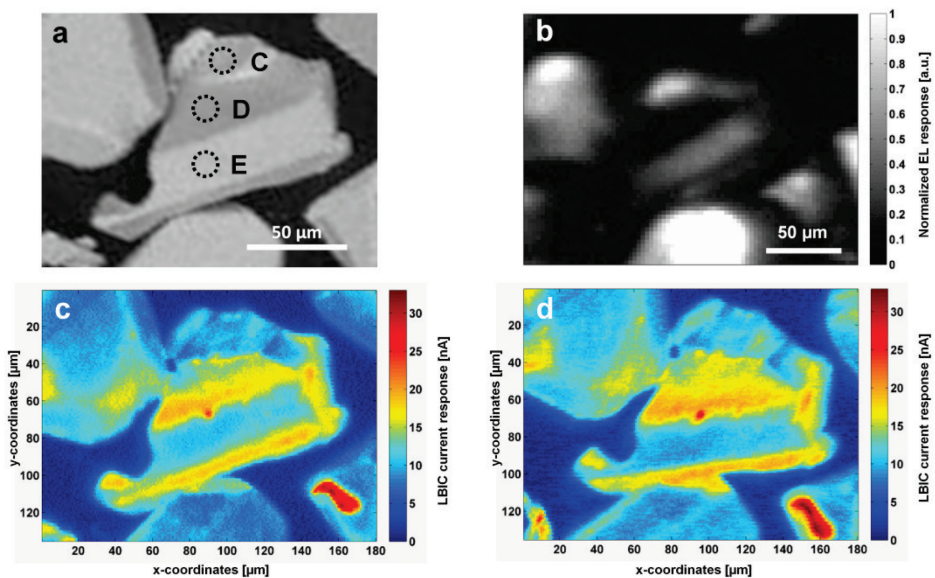


Figure 14 SEM (a), EL (b) and LBIC (c,d) images of one grain of sample 2b. In image (c) the LBIC scanning was conducted with the laser perpendicular to the membrane surface while in (d) the sample surface to the laser was tilted by around 18° . The dashed circles in (a) indicate the measurement spots where EL and PL spectra measurements are conducted (Figure 15).

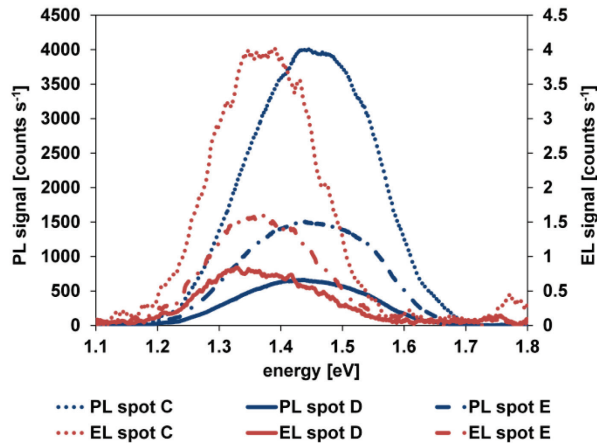


Figure 15 PL and EL spectra measurements of certain areas on the grain seen in Figure 14 as indicated by the dashed circles in Figure 14 a.

The results of the LBIC photocurrent measurements showing an inverse correlation with the EL and PL measurement data as well as the high inhomogeneity of the response for different areas can be explained by assuming a difference in the p-n-junction barrier height. The barrier height hereby correlates with the electric field, where a high barrier correlates to a strong and wide electric field and correspondingly a low barrier to a weaker and smaller electric field. Low barrier heights of grains or areas of grains lead to an insufficient charge carrier separation, which subsequently results in a low LBIC signal as well as a high recombination and thus a high PL result. Grains or areas of grains with a high barrier height on the other hand and a corresponding effective charge carrier separation lead to a high LBIC signal. At the same time the radiative recombination rate is reduced, resulting in a low PL signal. During EL measurements, the voltage is applied over the whole area. This results in variances in current flow densities. Where at grains or areas of grains with a low barrier a higher current is flowing, which is mainly limited by the Ohmic resistance of the materials involved, areas with a high barrier lead to a lower current flow. The higher current density flux at materials with low barriers, leads to a higher radiative recombination rate and therefore higher EL signal. Therefore we propose that the inverse correlation between LBIC and luminescence (PL and EL) response is the result of the mentioned difference in barrier heights and the corresponding electric field and p-n-junction.

In Figure 16, the integrated EL spectrum response, measured at different applied voltages between 1.2 V and 2 V from the same two grains indicated by dashed circles in Figure 11 is shown. From there it is seen that the integrated EL response of grain A (high LBIC, low EL and PL) is increasing slowly and non-linear with increasing voltage. Grain B (low LBIC, high EL and PL) on the other hand is increasing fast and nearly linearly with increasing voltage. This indicates that the current flow in grain A is limited by a high barrier (good p-n-junction, strong and wide electric field), while the current flow of grain B is bigger due to the lower barrier and just limited by the Ohmic resistance. These results clearly support the above proposed mechanism.

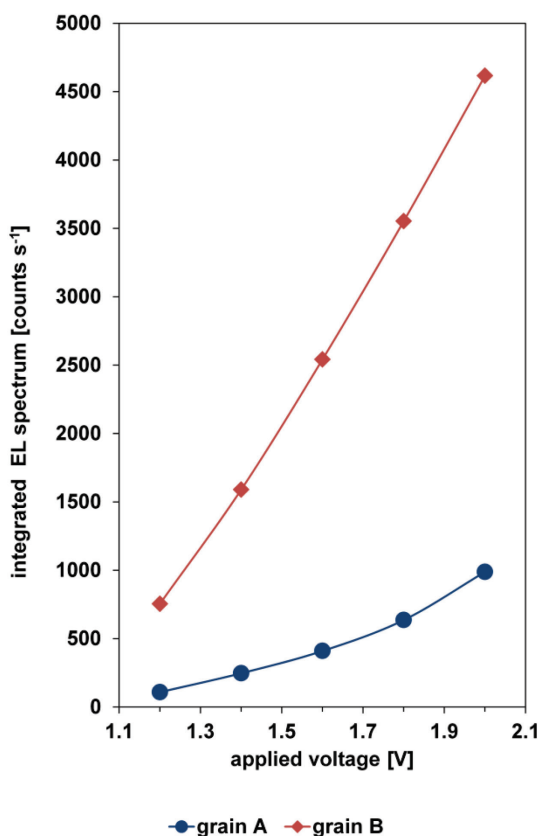


Figure 16 EL response of 2 grains seen in Figure 11 (indicated by dashed circles) for different applied voltages. The EL response was derived by the integration of the EL spectra.

3.4 Utilization of spatially resolved and integrated opto-electrical measurements for the identification of ageing processes

The stability of MGL solar cells is of great importance for a successful industrial implementation of this technology. To investigate and identify ageing or degradation mechanism, several investigation techniques are applied. For this work 4 different powders are analyzed. The solar cell parameters derived from j/V measurements are presented in Figure 17 for two pure sulfide powders, before (0h) and after degradation (8.5h and 95.5h). For both investigated samples a decrease in efficiency is noticeable with increasing degradation duration, however one is degrading stronger than the other. Therefore the samples are named “CZTS unstable” and “CZTS semi-stable” respectively. Comparing the solar cell parameters it shows that V_{OC} , fill factor (FF) and j_{SC} are decreasing very significantly for the unstable device. The semi-stable device on the other hand shows also a decrease in FF but to a smaller extent, while j_{SC} does not change much and V_{OC} is even increasing by a small amount. The increase of V_{OC} can be explained mostly by an ordering-disordering effect, as will be discussed later. The reduction of the FF and to a certain extent also j_{SC} is partially related to the change of the series resistance (R_S).

This change of R_s is very pronounced, with a very strong increase for the unstable sample and a smaller but still significant increase for the semi-stable device.

Similar observations, however to a lesser extent, can be made for the two sulfur-selenide samples which are investigated and where the solar cell parameters are shown in Figure 18. These two samples with their difference in change of the conversion efficiency upon ageing or degradation are named consequently “CZTSSe unstable” and “CZTSSe semi-stable”.

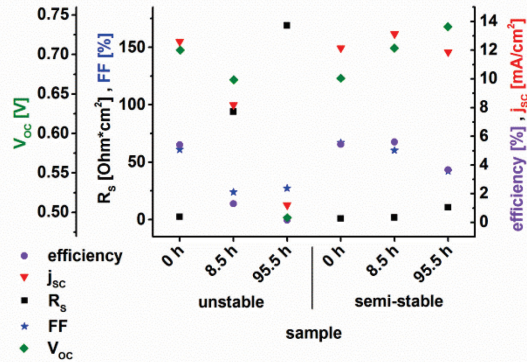


Figure 17 Solar cell parameters of CZTS samples after different times of degradation.

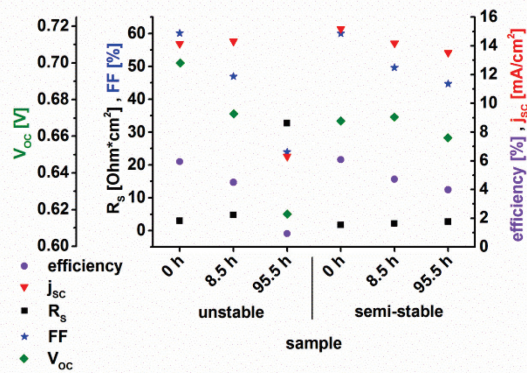


Figure 18 Solar cell parameters of CZTSSe samples after different times of degradation.

The j/V measurement data of all investigated samples is shown in Figure 19. The change in solar cell parameters can be also observed from there. Additionally a non-Ohmic barrier, opposite to the p-n-junction becomes visible during degradation, most notable for the unstable CZTS device after 8.5 hours of degradation.

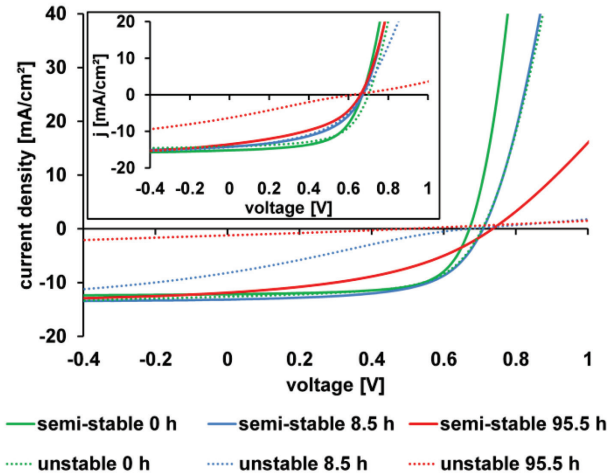


Figure 19 j/V measurements of CZTS samples after different times of degradation. The inset shows the j/V curves of the CZTSSe samples, with the same legend as for the CZTS samples.

To investigate the observed barrier in the j/V curves from Figure 19, devices with abraded grains and graphite contacts on the front and back side were manufactured, as described in the experimental part. These devices, named C-CZTS-C and C-CZTSSe-C are analyzed by j/V measurements. In Figure 20, the results of these measurements for the unstable CZTS device are shown. From there it is seen, that the j/V curve of the fresh (0 h) sample shows a nearly linear (Ohmic) behavior, while after 8.5 hours of degradation a very strong nonlinear curve (non-Ohmic behavior) can be observed. After further degradation however, at 95.5 hours, the curve shows again a very strong linear, Ohmic behavior, with an even higher current flow compared to the fresh sample before degradation. These results show clearly the formation of a barrier which is built up during the first few hours of degradation. This barrier is however just temporary.

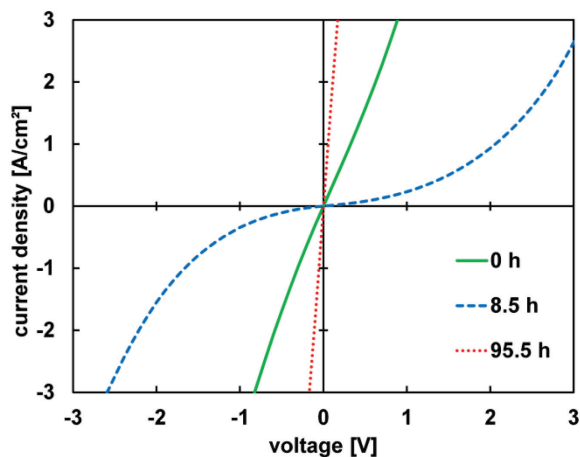


Figure 20 j/V measurements of the C-CZTS-C sample, made from unstable CZTS monograins after 0, 8.5 and 95.5 hours of degradation.

To analyze and compare the above observed temporary formation of the non-Ohmic barrier for all samples, the resistance, extracted from the slope of the j/V curves of the C-Kesterite-C samples at 0.1 V of the applied voltage, is shown for several degradation durations in Figure 21. In there it is seen that both CZTS samples show a sharp increase in resistance at the beginning of the degradation. However, the increase of the resistance is smaller for the semi-stable sample compared to the unstable sample. Furthermore, for both samples, unstable as well as semi-stable CZTS, the resistance decreases significantly again after further degradation, reaching values below the initial ones. A similar change of the resistance can be observed for the unstable CZTSSe device, but with prolonged degradation the reduction of the resistance is not so pronounced anymore, ending up at similar and comparable values than the initial resistance before degradation. In contrast to that, the resistance of the semi-stable C-CZTSSe-C sample does show just a minor change.

Since the measured j/V curves are partially strongly non-linear, the extracted resistance is voltage dependent. To account for this, the “linearity” is additionally extracted and shown in Figure 22. In here, the linearity is defined by the ratio of the resistance extracted at 0.9 V to the resistance at 0.1 V. Therefore the smaller the linearity value, the more non-linear respectively non-Ohmic is the measured j/V curve, with a value of 1 meaning a linear curve and an Ohmic resistance. Comparing the resistance values in Figure 21 and the linearity values in Figure 22, a clear correlation can be observed, where high resistance values correspond to small linearity values and vice versa. From this correlation it becomes clear that the increase respectively the change in resistance is mainly caused by the seen temporary barrier.

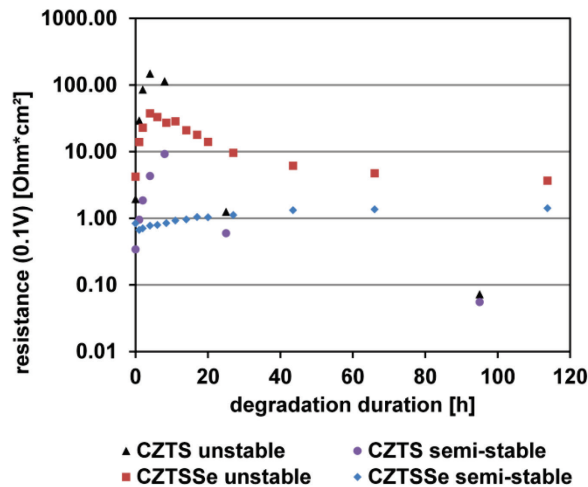


Figure 21 Resistances of C-CZTS-C and C-CZTSSe-C samples derived from the j/V measurements of these samples at 0.1V, different degradation durations.

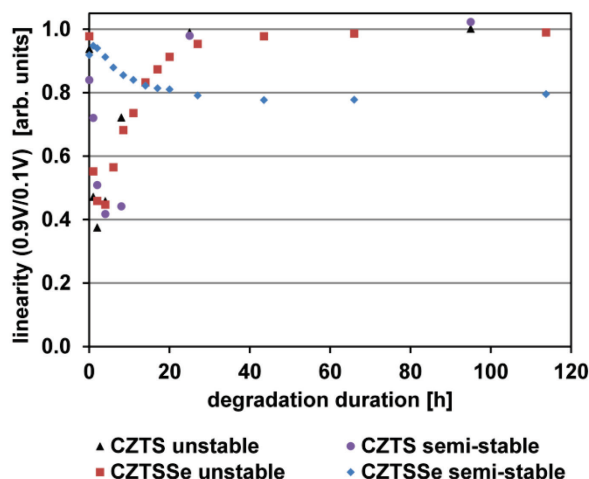


Figure 22 Linearity values of C-CZTS-C and C-CZTSSe-C samples, derived from the ratio of the resistance at 0.9V and 0.1V (see also text).

Since the temporary barrier is observed in C-Kesterites-C samples, it can be assumed that this barrier is caused by a change of the graphite-absorber interface. To evaluate this, surface sensitive XPS measurements are conducted at the polished backside of fresh (0h) and degraded samples (8.5 h and 95.5 h). For each measurement, separate samples are made, with identical powder and production process but with different degradation durations. The measured copper concentration, copper to zinc plus tin ratio with additionally the normalized R_s and efficiency of the solar cell parameters are shown in Table 4. From there a significant reduction of the copper concentration for the unstable CZTS and CZTSSe samples can be noticed, while for the semi-stable materials the copper depletion is less (for CZTS) or even no significant change can be observed (for CZTSSe). Similar changes during degradation can be observed from normalized the Cu to Zn plus Sn ratio, where the unstable absorber material shows a higher change than the semi-stable material. In addition, the change in copper concentration correlates very well with the change in the series resistance of the PV-devices, as seen from the normalized R_s value in Table 4. From these measurement results it can be concluded that the copper depletion at the surface of the Kesterite material on the backside and thus at the interface to the graphite back contact is the major reason for the formation of the temporary barrier observed earlier. With further copper reduction however, the barrier is vanishing again and a very low resistive Ohmic contact is formed again.

Table 4 XPS measurement results of the copper concentration in atomic percent and the normalized copper to zinc plus tin ratio measured at the back side of the samples at different degradation stages, with the efficiency and normalized R_s of the corresponding samples derived from the j/V measurements.

sample	deg. duration [h]	efficiency [%]	Cu conc. [at%]	Cu/(Zn+Sn) [a.u.]	norm. R_s [a.u.]
CZTS unstable	0	5.41	14.6	1.00	1.00
CZTS unstable	8.5	1.31	10.1	0.73	38.9
CZTS unstable	95.5	0.16	9.1	0.58	70.0
CZTS semi-stable	0	5.44	13.1	1.00	1.00
CZTS semi-stable	8.5	5.60	11.0	0.82	2.11
CZTS semi-stable	95.5	3.67	10.3	0.67	12.9
CZTSSe unstable	0	5.94	14.3	1.00	1.00
CZTSSe unstable	8.5	4.51	10.3	0.75	1.62
CZTSSe unstable	95.5	0.93	9.8	0.72	11.2
CZTSSe semi-stable	0	6.08	11.5	1.00	1.00
CZTSSe semi-stable	8.5	4.72	13.0	1.04	1.26
CZTSSe semi-stable	95.5	3.98	12.0	1.00	1.60

The formation of the temporary barrier at the graphite-absorber interface, presumably caused by the changed copper concentration, should correlate with a change in the energy bands and band alignments respectively. Degradation experiments with and without the presence of the graphite back contact as well as carefully removing the graphite back contact material after degradation and painting a fresh contact does not result in major changes in the j/V measurement results, thus it is concluded that the proposed change in energy bands and band alignment is just related to the absorber material. In order to evaluate this change, KP measurements are conducted on the abraded backside of devices, where the front side is connected with graphite paste (similar as the C-Kesterites-C samples but without graphite on the backside, thus forming an absorber-graphite structure). The results of the KP measurements can be seen in Figure 23. In there, the inset shows the workfunction difference to the gold probe after fresh abrasion of the backside over time. The measured workfunction difference is decreasing over time, but reaching a stabilized value after a few days of storage in ambient conditions, after which the values for “0 hours degradation” are measured. This change of the workfunction directly after the fresh abrasion can be attributed to oxidation processes of the very surface. The workfunction difference is not changing significantly anymore with degradation at elevated temperature (105°C). Since KP measurements are very surface sensitive, the oxidized surface dominates the measurement response and the attempted measurements of the change of the workfunction of the absorber material due to the degradation respectively copper diffusion is unsuccessful.

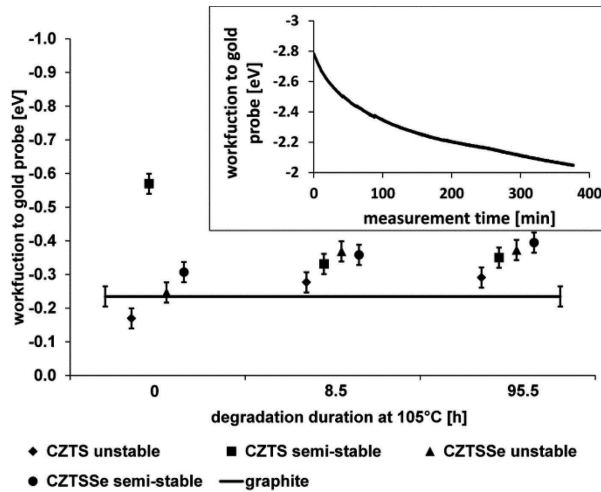


Figure 23 Kelvin Probe measurements on unstable and semi-stable CZTS and CZTSSe devices at different degradation stages.

Despite that the change in copper concentration and the related copper diffusion is measured on the surface of the backside, it shows the high mobility of copper at the applied degradation conditions. Therefore it can be assumed that also on the front side copper is diffusing. It is well known from literature [143, 144], that copper doping of CdS leads to photoconductivity with a high dark resistivity. Additionally it was reported in [145] that copper doping of CdS leads to recombination centers and therefore to increased recombination close to the p-n-junction with an ultimately reduced FF. These effects are the most likely reason for the observed increased resistance of the MGL PV-devices upon ageing as well the reduction of the solar cell parameters, especially FF.

Due to the increased recombination rate upon ageing, also a reduction of V_{OC} can be expected. This can be observed for the unstable CZTS and CZTSSe devices and to a smaller extent for the semi-stable CZTSSe sample, while for the semi-stable CZTS device V_{OC} is even increasing (compare Figure 17 and 18). Analyzing all samples at different degradation durations by means of PL, as seen in Figure 24 for the CZTS samples and Figure 25 for the CZTSSe samples, it can be noticed that for the CZTS devices the PL response is increasing and a shift of the peak towards higher energy is noticeable. The peak shift between the fresh and 95.5 hours degraded sample is approximately 100 meV. The change of the peak height and shift can be partially explained by the increased resistance upon ageing and thus an increased recombination as already observed before and described in paper II. A measurement with lower excitation light intensity by approximately one order of magnitude however leads just to a shift of the peak to lower energy values by just approximately 20 meV. The main reason for the peak shift can be attributed to an ordering-disordering process upon ageing, with more ordering corresponds to a peak position at higher energies. Such ordering-disordering related shifts of the PL peaks are in accordance with earlier published results [140], where a temperature treatment of CZTS monograins for 4 hours at 150°C led to a similar peak shift. The proposed ordering of the CZTS upon degradation explains the increase of V_{OC} for the semi-stable sample, while for the unstable CZTS sample the V_{OC} reducing effect of the degradation is already dominating, leading to a reduction of V_{OC} . For the CZTSSe samples however, no major PL peak shift can be observed upon ageing as seen

in Figure 25, hence it can be concluded that degradation does not lead to a major ordering of the absorber material in these samples. Therefore no increase of V_{OC} , but a degradation related reduction to different degrees can be observed.

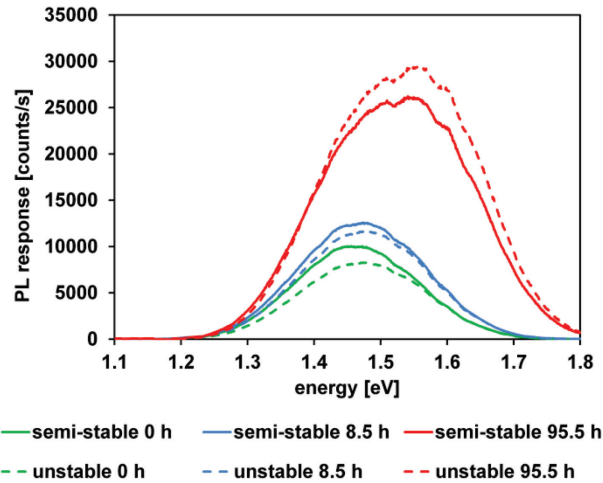


Figure 24 PL response of the semi-stable and unstable CZTS PV-devices without and after 8.5 and 95.5 hours of degradation.

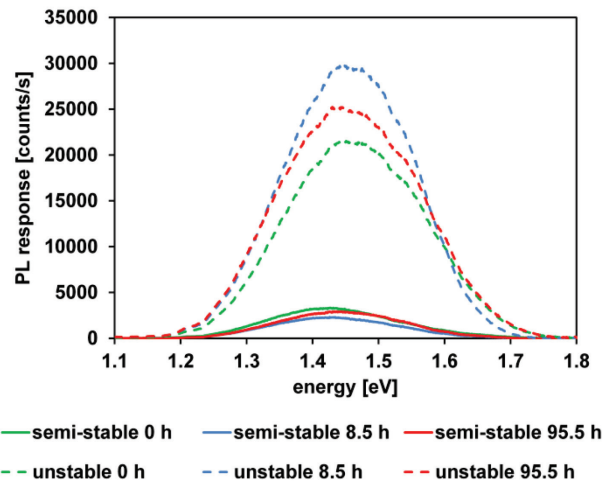


Figure 25 PL response of the semi-stable and unstable CZTSSe PV-devices without and after 8.5 and 95.5 hours of degradation.

Degradation can lead to a reduction of j_{SC} , as seen in Figures 17 and 18. Hence a detailed and spatially resolved high resolution investigation of the change in photocurrent response is conducted. Since the reduction of j_{SC} upon degradation is highest for the unstable CZTS samples, this material is chosen for further investigations. To analyze the local photocurrent distribution of different grains and areas of grains of a device, LBIC measurements are conducted of the same unstable CZTS sample at different degradation durations, which allows an analysis of each single grain. The results of these

measurements are seen in Figure 26. In Figure 26 a the photocurrent response of the fresh sample is displayed, which shows a very homogenous current distribution. After degrading the sample for 8.5 hours (Figure 26 b), the majority of the grains show an inhomogeneous reduction of the photocurrent, while some grains show even an increase. With further degradation for 95.5 hours (Figure 26 c), the current response for all grains is very weak, even for the grains which show an increased current response after 8.5 hours.

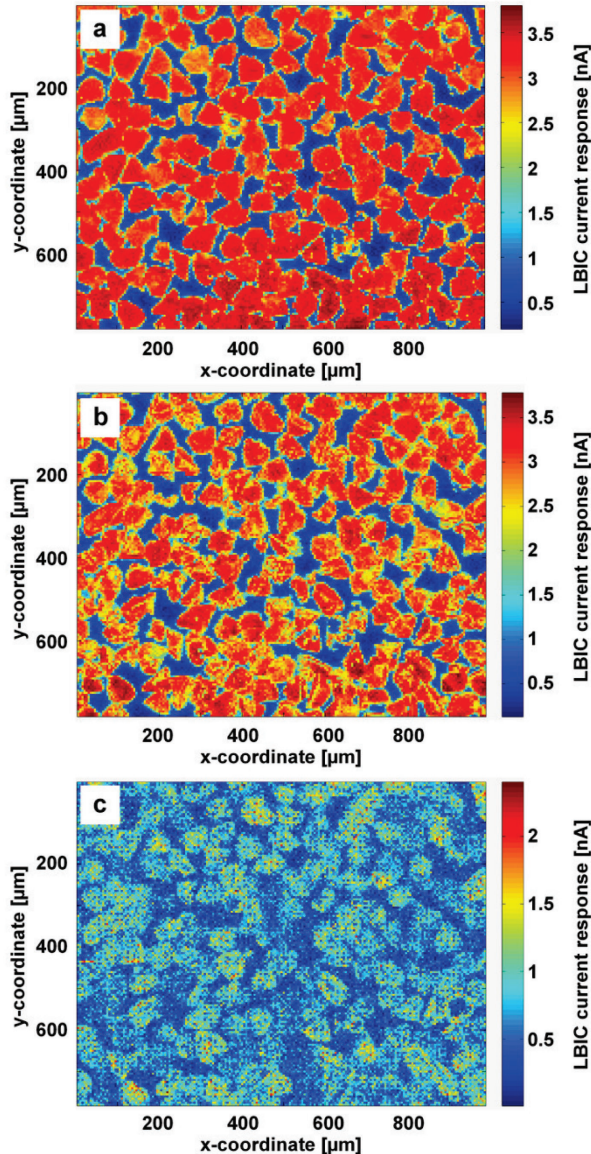


Figure 26 LBIC results of unstable fresh (0 h, a), medium aged (8.5 h, b) and most aged (95.5 h, c) CZTS photovoltaic devices.

The change in homogeneity becomes very clear when analyzing the LBIC data in the homogeneity plot, as seen in Figure 27. For a description on how such homogeneity plots

can be evaluated and which information and interpretation can be drawn, the reader is referred to Figure 8 and the related description in the text. As can be seen in Figure 27, while the highest current values between the fresh (0 hours) and 8.5 hours degraded samples are in a very similar range, the peak width, which corresponds to the homogeneity of the LBIC response, is widening for the sample after 8.5 hours of degradation compared to the fresh sample. Due to the very weak current response for the 95.5 hours degraded sample, the peak of the active area and the peak of the inactive area are very close at low current values and nearly no distinction between these two peaks is possible anymore.

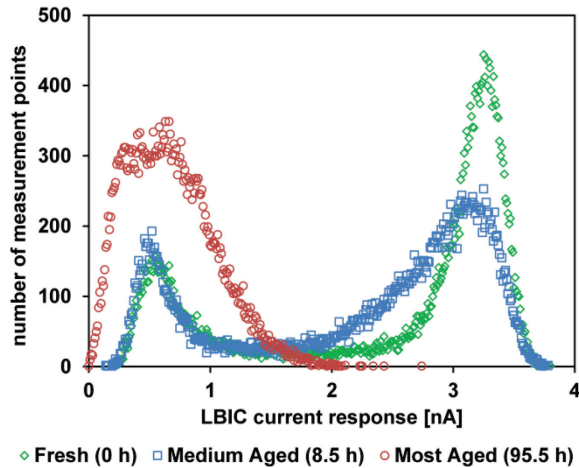


Figure 27 Homogeneity plot of the differently degraded unstable CZTS samples.

The local current generation in the absorber material is investigated by means of cross-section EBIC measurements. In Figure 28 an overview with low magnification (2000x) of such a measurement of a fresh sample is shown. The right side of the figure displays the SEM image of the cross-section sample, by the use of the secondary electron detector, by the use of the secondary electron detector. It shows two grains, with the front sealing polymer right side handed of these grains. Small metal parts are embedded into this sealing polymer to reduce charging effects. On the left side of Figure 28 the corresponding EBIC image is seen. It shows the EBIC signal, which follows the shape of the grains seen in the SEM image and thus the interface of CZTS-CdS-TCO.



Figure 28 EBIC signal of two CZTS grains (left) and the SEM picture of those (right).

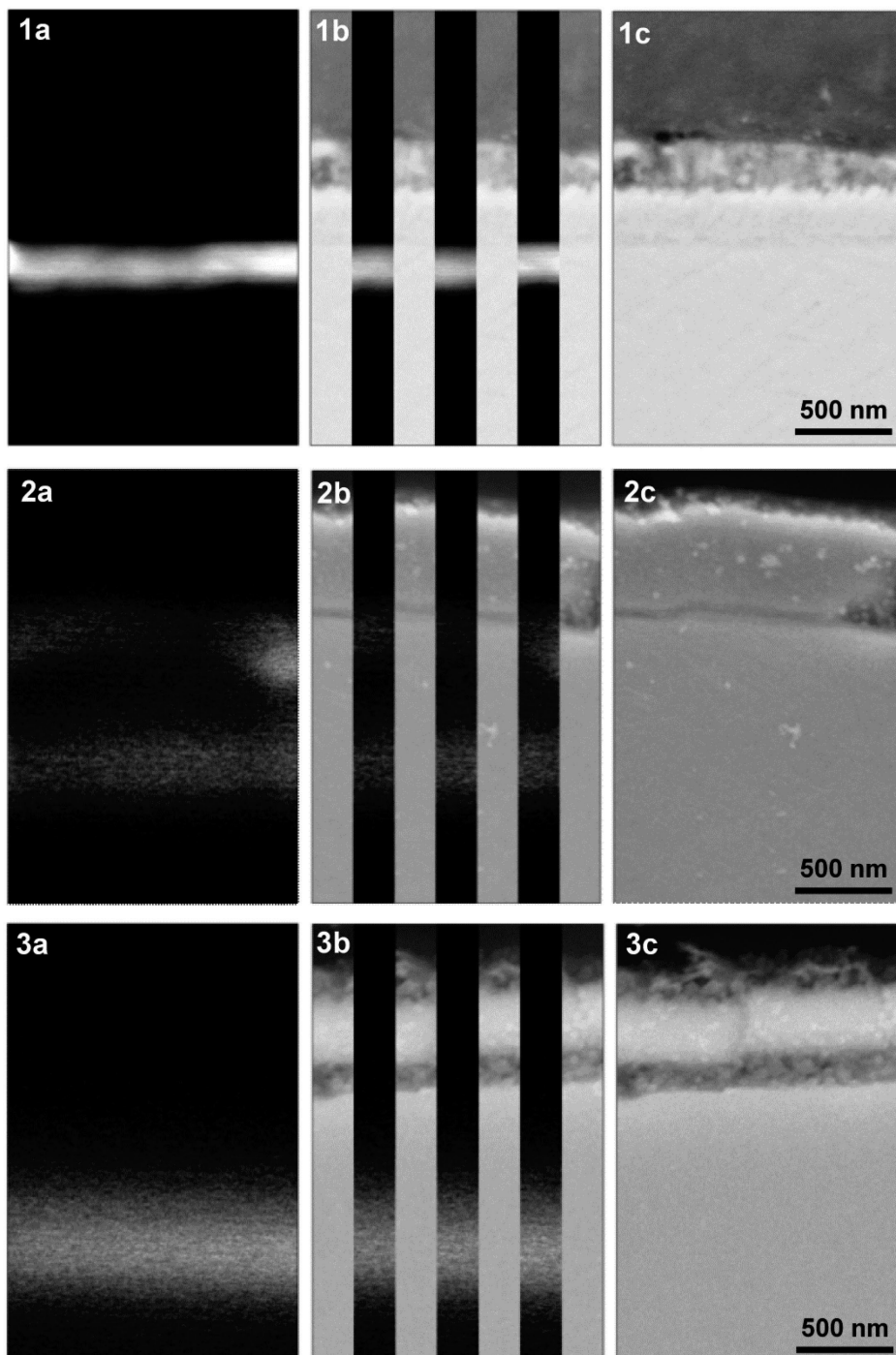


Figure 29 EBIC (a), superimposed EBIC on SEM (b) and SEM (c) pictures of fresh (1), 8.5 h degradation (2) and 95.5 h degradation (3) CZTS solar cell.

In Figure 29 high magnification (100 000x) EBIC (1a - 3a), SEM (1c - 3c) and superimposed EBIC on SEM (1b - 3b) images are shown for the fresh (0 h, 1a - 1c),

medium aged (8.5 h, 2a-2c) and most aged (95.5 h, 3a – 3c) samples. The fresh sample hereby shows a strong but narrow EBIC signal close to the CZTS-CdS interface. After 8.5 hours of degradation the EBIC response close to the interface is weakening and a second area, deeper in the bulk shows a signal. After further degradation (95.5 hours) the response close to the interface vanishes completely, while the response deeper in the bulk remains.

The appearance of the EBIC signal towards the CZTS-CdS interface is best seen in the normalized EBIC profiles seen in Figure 30. From there again the pronounced narrow EBIC peak close to the interface is seen, the double peak after 8.5 hours of degradation and the rather broad single peak deeper in the bulk of the sample after 95.5 hours of degradation.

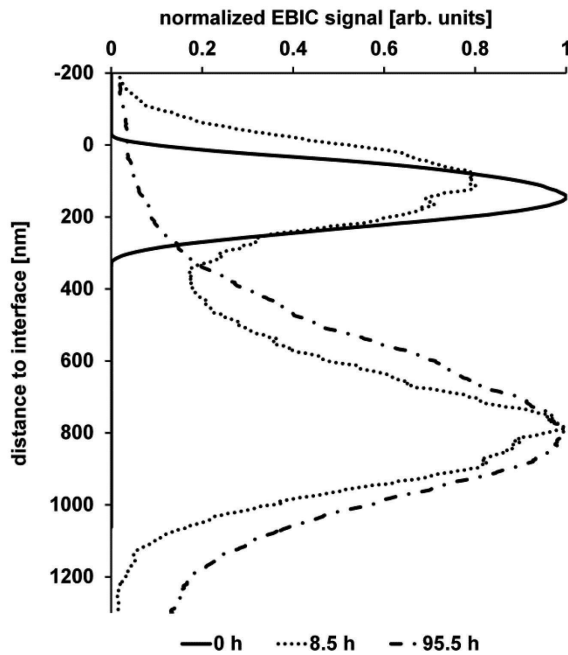


Figure 30 Normalized EBIC signal of CZTS of fresh (solid), 8.5 h degradation (dotted) and 95.5 h degradation (solid-dash).

The behavior of the change of the current response can be explained by the diffusion of the copper ions as proposed before. Copper in CdS causes strong recombination centers, an effect even used in photodetectors [11, 146]. Under dark conditions, this increases the resistance of the CdS, while under illumination the recombination centers lead to a low life time and high recombination rate of generated charge carriers in the CdS. For the measurements of the fresh, undegraded samples, without a major copper concentration in the CdS and the related recombination centers, the charge carrier collection stems predominantly from close the interface. The exact width of the space charge region (SCR) is still under investigation, however it can be assumed that it is wider than the seen peak for the fresh sample in Figure 30 and also charge carriers generated deeper in the bulk are collected to a minor extent, however since the signal close to the interface is strong, which requires a low EBIC current amplification, these charge carriers originating deeper in the bulk are not seen in the EBIC images or profiles in Figure 29 and

30. Upon degradation (e.g. after 8.5 hours) with a diffusion of copper into the CdS and the related generation of recombination centers, charge carriers which are generated close to the CdS (up to around 300 nm) and therefore are able to diffuse into the CdS, are recombining, hence the EBIC signal in this area is reduced. On the other hand, electron-hole pairs generated deeper in the bulk are separated by the electric field. Thereby the majority carriers (holes) do not diffuse in a sufficient amount into the CdS anymore, which reduces the recombination and the charge carriers can be extracted. Due to the smaller absolute signal strength, the current amplification has to be increased, which makes the charge carrier collection deeper in the bulk visible. From these results, also a diffusion length of around 300 nm can be estimated. With further degradation (e.g. after 95.5 hours) and increased copper diffusion and therefore recombination in the CdS the collection of charge carriers generated close to the CdS is very low and thus the EBIC signal is disappearing, while the signal from deeper in the bulk, where charge carriers are still collected, remains.

The above mentioned degradation related effects which lead to a change in current generation during EBIC measurements can be also observed from EQE measurements, which are seen in Figure 31 for the fresh (0 h) and degraded (8.5 h and 95.5 h) devices. Comparing the EQE response of the 8.5 hours degraded with the fresh sample, a reduction of the response in the short wavelength range (around 350 nm to 600 nm) can be noticed, while the response in the wavelength range higher than approximately 600 nm up to the bandgap is increasing. With further degradation (95.5 hours) the EQE response is decreasing over the whole wavelength range, however also here the reduction for the high energy excitation light is bigger compared to the low energy light. It has to be mentioned, that the reduction of the EQE response upon ageing is less compared to the reduction of the j_{sc} derived from the j/V measurements. The reason for the difference of EQE response and j_{sc} can be found in the difference in excitation light intensity, which is for the EQE measurements approximately by the factor 1000 lower compared to the light intensity during j/V measurements. Since high energy light is absorbed closer to the CZTS-CdS interface relatively compared to the low energy light, which penetrates the absorber layer also deeper into the bulk, the related charge carrier generation from the high energy light is effected more by the recombination centers in the CdS than the charge carriers generated by the low energy light deeper in the bulk, similar as discussed for the EBIC measurements. This explains the EQE measurement results and as well supports the above proposed mechanism about the effect of copper diffusion and the correlated recombination effects during degradation of the CZTS samples.

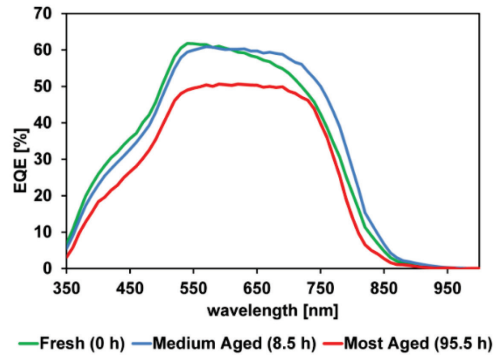


Figure 31 EQE measurements of the unstable CZTS PV-device, fresh and degraded for 8.5 and 95.5 hours.

4 Conclusions

Based on the aims of this study different questions and topics regarding the behavior of Kesterite MGL solar cells are analyzed. To achieve this, the devices are intensively investigated by different opto-electrical and spatially resolved analysis methods. The main outcomes of these investigations are:

- Spatially resolved investigations of MGL solar cells by means of LBIC allow the definition of certain areas such as the active area, border area and inactive area. The active area hereby can be further analyzed statistically to get information about the local photocurrent homogeneity and thereby the quality of the powder material used.
- By the ratio of the active area to the total area, the so called Active Area Ratio (AAR) can be evaluated. Attributing the photocurrent only to the active area, the “material efficiency” can be determined, which better characterizes the quality of the Kesterite material and its junctions eliminating density variations of the powder layer. For the record CZTSSe MGL device (certified cell efficiency 9.5 %) the material efficiency is in the range of the best thin film devices at around 12%.
- A combination of LBIC measurements with optical transmission and SEM imaging, allows determining the reason for inactive areas. Three different possibilities can be observed: inactive areas due to missing of absorber material (i.e. gaps between monograins, the majority of the inactive area), a missing front contact due to (mainly partial) coverage of monograins by electrically insulating polymer or, a missing back contact (e.g. due to insufficient opening or abrasion on the backside).
- The developed LBIC analysis is used for devices with different solar cell parameters, with an especially big difference in j_{sc} (sample 1, 2a and 2b). Thereby it is shown that the reason for the reduced j_{sc} in the worse performing samples (sample 2a and 2b) is not due to a difference in active area (as initially assumed). It results from a generally lower and a wider distribution of the photocurrent coming from the active area.
- By combining different opto-electrical measurement techniques such as LBIC, EL imaging and spectra and PL spectra measurements, the reason for the lower and inhomogeneous current response can be determined. An inverse correlation of the LBIC on the one hand and the PL and EL responses on the other hand can be observed. High LBIC corresponds to low EL and PL and vice versa. This can be attributed to differences in the p-n-junction and therefore related different barrier heights.
- Ageing or degradation investigations on CZTS and CZTSSe show highly different stabilities of samples. Two main degradation processes are identified. One is short termed and temporary back side degradation with a non-Ohmic barrier built up. The second is a long term permanent front side degradation leading to an increase of resistance and recombination.
- Copper diffusion processes are identified. Copper in CdS leads to an increase of the resistance, effective charge carrier recombination processes and pronounced photocurrent effects. All three are observed in aged or degraded devices.

- Cross-section EBIC measurements show a change of the photocurrent profile close to the CZTS-CdS interface with ageing time. It can be explained by progressive diffusion of copper into CdS upon ageing leading to an increase of recombination. Close to the interface, minority and majority charge carriers reach the CdS and recombine. Whereas majority carriers from deeper in the bulk will not reach the CdS anymore so that the photocurrent generated there is less affected. EQE measurements support this proposed mechanism.

References

- [1] OECD/IEA. (2017). 2017 World Energy Outlook. Paris, France: IEA Publishing.
- [2] Dudley, B. (2018). 2018 BP Energy Outlook. London, UK: BP energy economics.
- [3] FGH ISE. (2018). Photovoltaics Report 2018. Freiburg, Germany: Fraunhofer Institute for Solar Energy Systems, ISE.
- [4] de Wild-Scholten, M.J. (2013). Energy payback time and carbon footprint of commercial photovoltaic systems. *Sol. Energy Mater. Sol. Cells*, 119, 296-305.
- [5] Green, M.A., Hishikawa, Y., Dunlop, E.D., Levi, D.H., Hohl-Ebinger, J., Ho-Baillie, A.W.Y. (2018). Solar cell efficiency tables (version 51). *Prog. Photovolt: Res. Appl.*, 26, 3-12.
- [6] Solar Frontier K.K., 2-3-2 Daiba, Tokyo, Japan. (2019, February 3). Press release. Retrieved from http://www.solar-frontier.com/eng/news/2017/1220_press.
- [7] Andersson, B.A. (2000). Materials availability for large-scale thin-film photovoltaics. *Prog. Photovolt: Res. Appl.*, 8, 61-76.
- [8] Feltrin, A., Freundlich, A. (2008). Material considerations for terawatt level deployment of photovoltaics. *Renewable Energy*, 33, 180-185.
- [9] Grandell, L., Höök, M. (2015). Assessing rare metal availability challenges for solar energy technologies. *Sustainability*, 7, 11818-11837.
- [10] Green, M.A. (2009). Estimates of Te and In prices from direct mining of known ores. *Prog. Photovolt: Res. Appl.*, 17, 347-359
- [11] Meissner, D. (2013). Photovoltaics based on semiconductor powders. In A. Méndez-Vilas (Ed.). *Materials and processes for energy: communicating current research and technological developments* (pp. 114-125). Badajoz, Spain: Formatex Research Center.
- [12] Wang, W., Winkler, M.T., Gunawan, O., Gokmen, T., Todorov, T.K., Zhu, Y., Mitzi, D.B. (2014). Device characteristics of CZTSSe thin-film solar cells with 12.6% efficiency. *Adv. Energy Mater.*, 4, 1301465.
- [13] Ito, K., Nakazawa, T. (1988). Electrical and optical properties of Stannite-type quaternary semiconductor thin films. *Jap. J. Appl. Phys.*, 27, 2094-2097.
- [14] Mellikov, E., Meissner, D., Altosaar, M., Kauk, M., Krustok, J., Öpik, A., Volobujeva, O., Iljina, J., Timmo, K., Klavina, I., Raudoja, J., Grossberg, M., Varema, T., Muska, K., Ganchev, M., Bereznev, S., Danilson, M. (2011). CZTS monograin powders and thin films. *Advanced Materials Research*, 222, 8-13.
- [15] Krustok, J., Josepson, R., Danilson, M., Meissner, D. (2010). Temperature dependence of $\text{Cu}_2\text{ZnSn}(\text{Se}_x\text{S}_{1-x})_4$ monograin solar cells. *Solar Energy*, 84, 379-383.

- [16] Ito, K. (2015). An overview of CZTS-based thin-film solar cells. In K. Ito (Ed.). *Copper zinc tin sulfide-based thin-film solar cells*. (pp. 3-41). UK: John Wiley & Sons Ltd.
- [17] Nakayama, N., Ito, K. (1996). Sprayed films of Stannite $\text{Cu}_2\text{ZnSnS}_4$. *Applied Surface Science*, 92, 171-175.
- [18] Katagiri, H., Sasaguchi, N., Hando, S., Hoshino, S., Ohashi, J., Yokota, T. Preparation and evaluation of $\text{Cu}_2\text{ZnSnS}_4$ thin films by sulfurization of E-B evaporated precursors. *Sol. Energy Mater. Sol. Cells*, 49, 407-414.
- [19] Shibuya, T., Goto, Y., Kamihara, Y., Matoba, M., Yasuoka, K., Burton, L.A., Walsh, A. (2014). From Kesterite to Stannite photovoltaics: Stability and band gaps of the $\text{Cu}_2(\text{Zn,Fe})\text{SnS}_4$ alloy. *Appl. Phys.*, 104, 021912.
- [20] Schorr, S., Hoebler, H.J., Tovar, M. (2007). A neutron diffraction study of the Stannite-Kesterite solid solution series. *Eur. J. Mineral.*, 19, 65-73.
- [21] Schorr, S. (2011). The crystal structure of Kesterite type compounds: A neutron and X-ray diffraction study. *Sol. Energy Mater. Sol. Cells*, 95, 1482-1488.
- [22] Nozaki, H., Fukano, T., Ohta, S., Seno, Y., Katagiri, H., Jimbo, K. (2012). Crystal structure determination of solar cell materials: $\text{Cu}_2\text{ZnSnS}_4$ thin films using X-ray anomalous dispersion. *J. Alloy. Compd.*, 524, 22-25.
- [23] Siebentritt, S., Schorr, S. (2012). Kesterites - a challenging material for solar cells. *Prog. Photovolt: Res. Appl.*, 20, 512-519.
- [24] Persson, C. (2010). Electronic and optical properties of $\text{Cu}_2\text{ZnSnS}_4$ and $\text{Cu}_2\text{ZnSnSe}_4$. *J. Appl. Phys.*, 107, 053710.
- [25] Friedlmeier, T.M., Wieser, N., Walter, T., Dittrich, H., Schock, H.W. (1997). *Heterojunctions based on $\text{Cu}_2\text{ZnSnS}_4$ and $\text{Cu}_2\text{ZnSnSe}_4$ thin films*. Paper presented at the 14th European Photovoltaic Solar Energy Conference, Barcelona, Spain, (pp. 1242-1245).
- [26] Seol, J.S., Lee, S.Y., Lee, J.C., Nam, H.D., Kim, K.H. (2003). Electrical and optical properties of $\text{Cu}_2\text{ZnSnS}_4$ thin films prepared by RF magnetron sputtering process. *Sol. Energy Mater. Sol. Cells*, 75, 155-162.
- [27] Tanaka, T., Nagatomo, T., Kawasaki, D., Nishio, M., Guo, Q.X., Wakahara, A., Yoshida, A., Ogawa, H. (2005). Preparation of $\text{Cu}_2\text{ZnSnS}_4$ thin films by hybrid sputtering. *Journal of Physics and Chemistry of Solids*, 66, 1978-1981.
- [28] Moriya, K., Watabe, J., Tanaka, K., Uchiki, H. (2006). Characterisation of $\text{Cu}_2\text{ZnSnS}_4$ thin films prepared by photochemical deposition. *Phys. Stat. Sol. C*, 3, 2848-2852.
- [29] Scragg, J.J., Dale, P.J. Peter, L.M. (2008). Towards sustainable materials for solar energy conversion: preparation and photoelectrochemical characterization of $\text{Cu}_2\text{ZnSnS}_4$. *Electrochemistry Communications*, 10, 639-642.

- [30] Kamoun, N., Bouzouita, H., Rezig, B. (2007). Fabrication and characterization of $\text{Cu}_2\text{ZnSnS}_4$ thin films deposited by spray pyrolysis technique. *Thin Solid Films*, 515, 5949-5952.
- [31] Sekiguchi, K., Tanaka, K., Moriya, K., Uchiki, H. (2006). Epitaxial growth of $\text{Cu}_2\text{ZnSnS}_4$ thin films by pulsed laser deposition. *Phys. Stat. Sol. C*, 3, 2618-2621.
- [32] Zhang, J., Shao, L.X., Fu, Y.J., Xie, E.Q. (2006). $\text{Cu}_2\text{ZnSnS}_4$ thin films prepared by sulfurization of ion beam sputtered precursor and their electrical and optical properties. *Rare Metals*, 25, 315-319.
- [33] Katagiri, H., Saitoh, K., Washio, T., Shinohara, H., Kurumadani, T., Miyajima, S. (2001). Development of thin film solar cell based on $\text{Cu}_2\text{ZnSnS}_4$ thin films. *Sol. Energy Mater. Sol. Cells*, 65, 141-148.
- [34] Persson, C., Chen, R., Zhao, H., Kumar, M., Huang, D. (2015). Electronic structure and optical properties from first-principles modeling. In K. Ito (Ed.). *Copper zinc tin sulfide-based thin-film solar cells*. (pp. 75-105). UK: John Wiley & Sons Ltd.
- [35] Altosaar, M., Raudoja, J., Timmo, K., Danilson, M., Grossberg, M., Krustok, J., Mellikov, E. (2008). $\text{Cu}_2\text{Zn}_{1-x}\text{Cd}_x\text{Sn}(\text{Se}_{1-y}\text{S}_y)_4$ solid solutions as absorber materials for solar cells. *Phys. Stat. Sol. A*, 205, 167-170.
- [36] Todorov, T., Reuter, K., Mitzi, D.B. (2010). High-efficiency solar cell with earth-abundant liquid-processed absorber. *Advanced Materials*, 22, E156-E159.
- [37] Grossberg, M., Krustok, J., Timmo, K., Altosaar, M. (2009). Radiative recombination in $\text{Cu}_2\text{ZnSnSe}_4$ monograins studied by photoluminescence spectroscopy. *Thin Solid Films*, 517, 2489-2492.
- [38] Chen, S., Gong, X.G., Walsh, A., Wei, S.H. (2009). Crystal and electronic band structure of $\text{Cu}_2\text{ZnSnX}_4$ (X=S and Se) photovoltaic absorbers: First-principles insights. *Appl. Phys. Lett.*, 94, 041903.
- [39] Zoppi, G., Forbes, I., Miles, R.W., Dale, P.J., Scragg, J.J., Peter, L.M. (2009). $\text{Cu}_2\text{ZnSnSe}_4$ thin film solar cells produced by selenisation of magnetron sputtered precursors. *Prog. Photovolt: Res. Appl.*, 17, 315-319.
- [40] Ahn, S., Jung, S., Gwak, J., Cho, A., Shin, K., Yoon, K., Park, D., Cheong, H., Yun J.H. (2010). Determination of band gap energy (E_g) of $\text{Cu}_2\text{ZnSnSe}_4$ thin films: on the discrepancies of reported band gap values. *Appl. Phys. Lett.*, 97, 021905.
- [41] Babu, G.S., Kishore Kumar, Y.B., Uday Bhaskar, P., Sundara Raja, V. (2008). Effect of post-deposition annealing on the growth of $\text{Cu}_2\text{ZnSnSe}_4$ thin films for a solar cell absorber layer. *Semicond. Sci. Technol.*, 23, 085023.

- [42] Matsushita, H., Maeda, T., Katsui, A., Takizawa, T. (2000). Thermal analysis and synthesis from the melts of Cu-based quaternary compounds Cu-III-IV-VI_4 , and $\text{Cu}_2\text{-II-IV-VI}_4$ (II = Zn, Cd; III =Ga, In; IV= Ge, Sn; VI = Se). *Journal of Crystal Growth*, 208, 416-422.
- [43] Wibowo, R.A., Kim, W.S., Lee, E.S., Munir, B., Kim, K.H. (2007). Single step preparation of quaternary $\text{Cu}_2\text{ZnSnSe}_4$ thin films by RF magnetron sputtering from binary chalcogenide targets. *Journal of Physics and Chemistry of Solids*, 68, 1908-1913.
- [44] Wibowo, R.A., Lee, E.S., Munir, B., Kim, K.H. (2007). Pulsed laser deposition of quaternary $\text{Cu}_2\text{ZnSnSe}_4$ thin films. *Phys. Stat. Sol. A*, 204, 3373-3379.
- [45] Liu, M.L., Huang, F.Q., Chen, L.D., Chen, I.W. (2009). A wide-band-gap p-type thermoelectric material based on quaternary chalcogenides of $\text{Cu}_2\text{ZnSnQ}_4$ (Q=S, Se). *Appl. Phys. Lett.*, 94, 202103.
- [46] Babu, G.S., Kumar, Y.B.K., Bhaskar, P.U., Vanjari, S.R. (2010). Effect of Cu/(Zn+Sn) ratio on the properties of co-evaporated $\text{Cu}_2\text{ZnSnSe}_4$ thin films. *Sol. Energy Mater. Sol. Cells*, 94, 221-226.
- [47] Grossberg, M., Krustok, J., Raudoja, J., Timmo, K., Altosaar, M., Raadik, T. (2011). Photoluminescence and Raman study of $\text{Cu}_2\text{ZnSn}(\text{Se}_x\text{S}_{1-x})_4$ monograins for photovoltaic applications. *Thin Solid Films*, 519, 7403-7406.
- [48] Riha, S.C., Parkinson, B.A., Prieto, A.L. (2011). Compositionally tunable $\text{Cu}_2\text{ZnSn}(\text{S}_{1-x}\text{Se}_x)_4$ nanocrystals: Probing the effect of Se-inclusion in mixed chalcogenide thin films. *J. Am. Chem. Soc.*, 133, 15272-15275
- [49] Ramasamy, K., Malik M.A., O'Brien, P. (2012). Routes to copper zinc tin sulfide $\text{Cu}_2\text{ZnSnS}_4$ a potential material for solar cells. *Chem. Commun.*, 48, 5703-5714.
- [50] Chen, S., Walsh, A., Gong, X.G., Wei, S.H. (2013). Classification of lattice defects in the Kesterite $\text{Cu}_2\text{ZnSnS}_4$ and $\text{Cu}_2\text{ZnSnSe}_4$ earth-abundant solar cell absorbers. *Adv. Mater.*, 25, 1522-1539.
- [51] Chen, S., Gong, X.G., Walsh, A., Wei, S.H. (2010). Defect physics of the Kesterite thin-film solar cell absorber $\text{Cu}_2\text{ZnSnS}_4$. *Appl. Phys. Lett.*, 96, 021902.
- [52] Chen, S., Yang, J.H., Gong, X.G., Walsh, A., Wei, S.H. (2010). Intrinsic point defects and complexes in the quaternary Kesterite semiconductor $\text{Cu}_2\text{ZnSnS}_4$. *Phys Rev. B*, 81, 245204.
- [53] Romero, M.J., Du, H., Teeter, G., Yan, Y., Al-Jassim, M.M. (2011). Comparative study of the luminescence and intrinsic point defects in the Kesterite $\text{Cu}_2\text{ZnSnS}_4$ and chalcopyrite $\text{Cu}(\text{In,Ga})\text{Se}_2$ thin films used in photovoltaic applications. *Phys Rev. B*, 84, 165324.
- [54] Polizzotti, A., Repins, I., Noufi, R., Wei, S.H., Mitzi, D. (2013). The state and future prospects of Kesterite photovoltaics. *Energy Environ. Sci.*, 6, 3171-3182.

- [55] Katagiri, H., Jimbo, K., Maw, W.S., Oishi, K., Yamazaki, M., Araki, H., Takeuchi, A. (2009). Development of CZTS-based thin film solar cells. *Thin Solid Films*, 517, 2455-2460.
- [56] Ennaoui, A., Lux-Steiner, M., Weber, A., Abou-Ras, D., Kötschau, I., Schock, H.-W., Schurr, R., Hölzing, A., Jost, S., Hock, R., Voß, T., Schulze, J., Kirbs, A. (2009). Cu₂ZnSnS₄ thin film solar cells from electroplated precursors: Novel low-cost perspective. *Thin Solid Films*, 517, 2511-2514.
- [57] Ki, W., Hillhouse, H.W. (2011). Earth-abundant element photovoltaics directly from soluble precursors with high yield using a non-toxic solvent. *Adv. Energy Mater.*, 1, 732-735.
- [58] Repins, I., Beall, C., Vora, N., DeHart, C., Kuciauskas, D., Dippo, P., To, B., Mann, J., Hsu, W.-C., Goodrich, A., Noufi, R. (2012). Co-evaporated Cu₂ZnSnSe₄ films and devices. *Sol. Energy Mater. Sol. Cells*, 101, 154-159.
- [59] Tanaka, K., Oonuki, M., Moritake, N., Uchiki, H. (2009). Cu₂ZnSnS₄ thin film solar cells prepared by non-vacuum processing. *Sol. Energy Mater. Sol. Cells*, 93, 583-587.
- [60] Shin, B., Gunawan, O., Zhu, Y., Bojarczuk, N.A., Chey, S.J., Guha, S. (2013). Thin film solar cell with 8.4% power conversion efficiency using an earth-abundant Cu₂ZnSnS₄ absorber. *Prog. Photovolt: Res. Appl.*, 21, 72-76.
- [61] Tanaka, K., Fukui, Y., Moritake, N., Uchiki, H. (2011). Chemical composition dependence of morphological and optical properties of Cu₂ZnSnS₄ thin films deposited by sol-gel sulfurization and Cu₂ZnSnS₄ thin film solar cell efficiency. *Sol. Energy Mater. Sol. Cells*, 95, 838-842.
- [62] Wang, H. (2011). Progress in thin film solar cells based on Cu₂ZnSnS₄. *Int. J. Photoenergy*, 2011, 801292.
- [63] Kumar, M., Dubey, A., Adhikari, N., Venkatesan, S., Qiao, Q. (2015). Strategic review of secondary phases, defects and defect-complexes in Kesterite CZTS-Se solar cells. *Energy Environ. Sci.*, 8, 3134-3159.
- [64] Yan, C., Huang, J., Sun, K., Johnston, S., Zhang, Y., Sun, H., Pu, A., He, M., Liu, F., Eder, K., Yang, L., Cairney, J.M., Ekins-Daukes, N.J., Hameiri, Z., Stride, J.A., Chen, S., Green, M.A., Hao, X. (2018). Cu₂ZnSnS₄ solar cell power conversion efficiency breaking the 10% barrier through heterojunction heat treatment. *Nature Energy*, 3, 764-772.
- [65] Lee, Y.S., Gershon, T., Gunawan, O., Todorov, T.K., Gokmen, T., Virgus, Y., Guha, S. (2015). Cu₂ZnSnSe₄ thin-film solar cells by thermal coevaporation with 11.6% efficiency and improved minority carrier diffusion length. *Adv. Energy Mater.*, 5, 1401372.
- [66] Mitzi, D.B., Gunawan, O., Todorov, T.K., Wang, K., Guha, S. (2011). The path towards a high-performance solution-processed Kesterite solar cell, *Sol. Energy Mater. Sol. Cells*, 95, 1421-1436.

- [67] Katagiri, H. (2015). Sulfurization of physical vapor-deposited precursor layers. In K. Ito (Ed.). *Copper zinc tin sulfide-based thin-film solar cells*. (pp. 183-202). UK: John Wiley & Sons Ltd.
- [68] Platzer-Björkman, C., Ericson, T., Scragg, J., Kubart, T. (2015). Reactive sputtering of CZTS. In K. Ito (Ed.). *Copper zinc tin sulfide-based thin-film solar cells*. (pp. 203-219). UK: John Wiley & Sons Ltd.
- [69] Unold, T., Just, J., Schock, H.-W. (2015). Coevaporation of CZTS films and solar cells. In K. Ito (Ed.). *Copper zinc tin sulfide-based thin-film solar cells*. (pp. 221-238). UK: John Wiley & Sons Ltd.
- [70] Hages, C.J., Agrawal, R. (2015). Synthesis of CZTSSe thin films from nanocrystal inks. In K. Ito (Ed.). *Copper zinc tin sulfide-based thin-film solar cells*. (pp. 239-270). UK: John Wiley & Sons Ltd.
- [71] Tanaka, K. (2015). CZTS thin films prepared by a non-vacuum process. In K. Ito (Ed.). *Copper zinc tin sulfide-based thin-film solar cells*. (pp. 271-287). UK: John Wiley & Sons Ltd.
- [72] Mellikov, E., Altosaar, M., Kauk-Kuusik, M., Timmo, K., Meissner, D., Grossberg, M., Krustok, J., Volobujeva, O. (2015). Growth of CZTS-based monograins and their application to membrane solar cells. In K. Ito (Ed.). *Copper zinc tin sulfide-based thin-film solar cells*. (pp. 289-309). UK: John Wiley & Sons Ltd.
- [73] Paradise, M.E. (1957). Large area solar energy converter and method for making the same. *Patent No. US 2,904,613*.
- [74] te Velde, T.S. (1965). Electrical monograin layers having a radiation permeable electrode. *Patent No. NL6510095*.
- [75] Meissner, D., Memming, R., Kastening, B. (1982). *Light induced hydrogen formation at CdS monograin membranes*. In J. Rabani, (Ed.), Paper presented at 4th international conference on photochemical conversion and storage of solar energy, Book of abstracts (p.267). Israel: The Hebrew university of Jerusalem.
- [76] Meissner, D., Memming, R., Kastening, B. (1983). Applications of monograin membranes for H₂O photoelectrolysis. In D.O. Hall, W. Palz, D. Pirrwitz (Eds.). *Photochemical, photoelectrochemical and photobiological processes*. (p. 110). Dordrecht, Netherlands: D. Reidel Publ. Comp.
- [77] Meissner, D., Memming, R., Kastening, B. (1983). The role of catalysis in light induced electrochemical reactions at semiconductor particles. *J. Electrochem. Soc.*, 131, 108 C.
- [78] Meissner, D., Memming, R., Kastening, B. (1983). Light induced generation of hydrogen at CdS-monograin membranes. *Chem. Phys. Lett.*, 96, 34-37.

- [79] Mellikov, E., Hiie, J. (1976). Effect of flux nature on the morphology of a recrystallized powder. *Trudy Tallinskogo Politehnicheskogo Instituta*, 404, 119-126.
- [80] Mellikov, E., Hiie, J. (1977). Mechanism and kinetics of growth and morphology of cadmium sulphide crystals. *Tezisy Dokl. Vses. Soveshch. Rostu Krist.*, 5th 1, 146-147.
- [81] Hiie, J., Krunks, M., Mellikov, E., Veel, E. (1980). *Photoconductive cadmium sulfide and cadmium sulfide selenide (CdS_xSe_{1-x}) layers for microwave range*. Paper presented at the 9th Int. Symp. Technical Committee on Photon-Detectors. (pp. 167-171).
- [82] Hiie, J., Ilna, N., Kukk, P., Mellikov, E., Varema, T. (1980). *Cadmium sulfide monograin layers as detectors of visible and x rays*. Paper presented at the 9th Int. Symp. Technical Committee on Photon-Detectors. (pp.172-174).
- [83] Mellikov, E., Hiie, J., Altosaar, M. (1994). Monograin A2B6 powders. *Proc. SPIE*, 2228, Producibility of II-VI materials and devices, 177-185.
- [84] Wirts, C., Altosaar, M., Varema, T., Mellikov, E., Meissner, D. (1994). *Tailoring II/VI semiconductor materials properties to photoelectrochemical requirements*. Paper presented at the 10th Int. Conf. Photoelectrochem. Conversion Storage of Solar Energy Interlaken, Switzerland. (p. 387).
- [85] Krustok, J., Mädasson, J., Hjelt, K., Collan, H. (1995). Study of the edge and exciton emission in CdTe:Cu:Cl powder samples. *J. Mater. Sci. Lett.*, 14, 1490-1492.
- [86] Hiie, J., Altosaar, M., Mellikov, E., Kukk, P., Sapogova, J., Meissner, D. (1997). Growth of CdTe monograin powders. *Physica Scripta*, T69, 155-158.
- [87] Krustok, J., Schön, J.H., Collan, H., Yakushev, M., Mädasson, J., Bucher, E. (1999). Origin of the deep center photoluminescence in CuGaSe₂ and CuInS₂ crystals. *J. Appl. Phys.*, 86, 364-369.
- [88] Altosaar, M., Mellikov, E. (2000). CuInSe₂ monograin growth in CuSe-Se liquid phase. *Jpn. J. Appl. Phys.*, 39, 65-66.
- [89] Altosaar, M., Jagomägi, A., Kauk, M., Krunks, M., Krustok, J., Mellikov, E., Raudoja, J., Varema, T. (2003). Monograin layer solar cells. *Thin Solid Films*, 431-432, 466-469.
- [90] Altosaar, M., Danilson, M., Kauk, M., Krustok, J., Mellikov, E., Raudoja, J., Timmo, K., Varema, T. (2005). Further developments in CIS monograin layer solar cells technology. *Sol. Energy Mater. Sol. Cells*, 87, 25-32.
- [91] Timmo, K., Altosaar, M., Kauk, M., Raudoja, J., Mellikov, E. (2007). CuInSe₂ monograin growth in the liquid phase of potassium iodide. *Thin Solid Films*, 15, 5884-5886.

- [92] Altosaar, M., Raudoja, J., Timmo, K., Danilson, M., Grossberg, M., Krunks, M., Varema, T., Mellikov, E. (2006). *Cu₂ZnSnSe₄ monograin powders for solar cell application*. Paper presented at the 4th World Conf. Photovoltaic Energy Conversion, Waikoloa, HI, USA. (p. 468).
- [93] Mellikov, E., Meissner, D., Varema, T., Altosaar, M., Kauk, M., Volobujeva, O., Raudoja, J., Timmo, K., Danilson, M. (2009). Monograin materials for solar cells. *Sol. Energy Mater. Sol. Cells*, 93, 65-68.
- [94] Krustok, J., Josepson, R., Danilson, M., Meissner, D. (2010). Temperature dependence of Cu₂ZnSn(Se_xS_{1-x})₄ monograin solar cells. *Solar Energy*, 84, 379-383.
- [95] Klavina, I., Kaljuvee, T., Timmo, K., Raudoja, J., Traksmas, R., Altosaar, M., Meissner, D. (2011). Study of Cu₂ZnSnSe₄ monograin formation in molten KI starting from binary chalcogenides. *Thin Solid Films*, 519, 7399-7402.
- [96] Cashmore, M.T., Koutsourakis, G., Gottschalg, R., Hall, S.R.G. (2016). Optical technique for photovoltaic spatial current response measurements using compressive sensing and random binary projections. *J. Photon. Energy*, 6, 025508.
- [97] Gupta, R., Breitenstein, O. (2007). Digital micromirror device application for inline characterization of solar cells by tomographic light beam-induced current imaging, *Proc. SPIE*, 6616, Optical measurement systems for industrial inspection V, 661600.
- [98] Vorasayan, P., Betts, T.R., Tiwari, A.N., Gottschalg, R. (2009). Multi-laser LBIC system for thin film PV module characterization. *Sol. Energy Mater. Sol. Cells*, 93, 917-921.
- [99] Chen, Q., Zhang, Y. (2014). *Correlating multiple spatially-resolved techniques (LBIC/Raman/PL/Reflectance/SEM/AFM) in the study of microscopic inhomogeneity of thin-film solar cells: Cu₂ZnSnSe₄ as an example*. Paper presented at the 40th Photovoltaic Specialist Conference (PVSC), Denver, CO, USA. (p. 3338).
- [100] Chen, Q., Zhang, Y. (2013). The reversal of the laser-beam-induced-current contrast with varying illumination density in a Cu₂ZnSnSe₄ thin-film solar cell. *Appl. Phys. Lett.*, 103, 242104.
- [101] Carstensen, J., Popkirov, G., Bahr, J., Föll, H. (2003). CELLO: an advanced LBIC measurement technique for solar cell local characterization. *Sol. Energy Mater. Sol. Cells*, 76, 599-611.
- [102] Edwards, P.R., Galloway, S.A., Durose, K. (2000). Erratum to "EBIC and luminescence mapping of CdTe/CdS solar cells". *Thin Solid Films*, 372, 284-291.
- [103] Kaminski, A., Breitenstein, O., Boyeaux, J.P., Rakotoniaina, P., Laugier, A. (2004). Light beam induced current and infrared thermography studies of multicrystalline silicon solar cells. *J. Phys.: Condens. Matter*, 16, S9-S18.

- [104] Peloso, M.P., Sern Lew, J., Trupke, T., Peters, M., Utama, R., Aberle, A.G. (2011). Evaluating the electrical properties of silicon wafer solar cells using hyperspectral imaging of luminescence. *Appl. Phys. Lett.*, 99, 97-99.
- [105] Nishioka, K., Yagi, T., Uraoka, Y., Fuyuki, T. (2007). Effect of hydrogen plasma treatment on grain boundaries in polycrystalline silicon solar cell evaluated by laser-beam-induced current. *Sol. Energy Mater. Sol. Cells*, 91, 1-5.
- [106] Dimassi, W., Bouaïcha, M., Nouri, H., Boujmil, M.F., Ben Nasrallah, S., Bessaïs, B. (2006). Grooving of grain boundaries in multicrystalline silicon: effect on solar cell performance. *Nucl. Instr. and Meth. in Phys. Res. B*, 253, 260-263.
- [107] Boyeaux, J.P., Kaminski, A., Fave, A., Laugier, A. (2001). Local characterization of large area multicrystalline solar cells by non-destructive mapping. *Mater. Sci. Semicond. Process.*, 4, 261-263.
- [108] Khezami, L., Al Megbel, A.O., Jemai, A.B., Ben Rabha, M. (2015). Theoretical and experimental analysis on effect of porous silicon surface treatment in multicrystalline silicon solar cells. *Appl. Surf. Sci.*, 353, 106-111.
- [109] Eisele, C., Nebel, C.E., Stutzmann, M. (2000). Spatially resolved photocurrent measurements of microstructured a-Si:H solar cells. *J. Non. Cryst. Solids*, 266-269, 1109-1113.
- [110] Kushiya, K. (2001). Improvement of electrical yield in the fabrication of CIGS-based thin-film modules. *Thin Solid Films*, 387, 257-261.
- [111] Jones, T.W., Feron, K., Anderson, K.F., Duck, B.C., Wilson, G.J. (2014). An applied light-beam induced current study of dye-sensitised solar cells: Photocurrent uniformity mapping and true photoactive area evaluation. *J. Appl. Phys.*, 116, 043104.
- [112] Navas, F.J., Alcántara, R., Fernández-Lorenzo, C., Martín-Calleja, J. (2010). High resolution laser beam induced current images under trichromatic laser radiation: Approximation to the solar irradiation. *Review of Scientific Instruments*, 81, 035108.
- [113] Scarratt, N.W., Griffin, J., Wang, T., Zhang, Y., Yi, H., Iraqi, A., Lidzey, D.G. (2015). Polymer-based solar cells having an active area of 1.6 cm² fabricated via spray coating. *APL Mater.*, 3, 126108.
- [114] Gershon, T., Hamann, C., Hopstaken, M., Lee, Y.S., Shin, B., Haight, R. (2015). Chemical consequences of alkali inhomogeneity in Cu₂ZnSnS₄ thin-film solar cells. *Adv. Energy Mater.*, 5, 1500922.
- [115] Feng, A.L., Li, G., He, G., Sun, Z.Q., Hu, W.D., Chen, X.S., Yin, F., Zhang, B., Lu, W. (2013). The role of localized junction leakage in the temperature-dependent laser-beam induced current spectra for HgCdTe infrared focal plane array photodiodes. *J. Appl. Phys.*, 114, 173107.

- [116] Xu, C., Denk, W. (1997). Two-photon optical beam induced current imaging through the backside of integrated circuits. *Appl. Phys. Lett.*, 71, 2578-2580.
- [117] Dimassi, W., Bouaïcha, M., Saadoun, M., Bessaïs, B., Ezzaouia, H., Bennaceur, R. (2002). Porous silicon-based passivation and gettering in polycrystalline silicon solar cells. *Nucl. Instr. and Meth. in Phys. Res. B*, 186, 441-445.
- [118] Dimassi, W., Bouaïcha, M., Kharroubi, M., Lajnef, M., Ezzaouia, H., Bessaïs, B. (2008). Two-dimensional LBIC and internal quantum efficiency investigations of porous silicon-based gettering procedure in multicrystalline silicon. *Sol. Energy Mater. Sol. Cells*, 92, 1421-1424.
- [119] Lehner, F. (2011). *Light beam induced current mapping for analysis of monograin layer solar cells* (Master's thesis). Tallinn University of Technology, Tallinn, Estonia.
- [120] Leamy, H.J. (1982). Charge collection scanning electron microscopy. *J. Appl. Phys.*, 53, R51-R80.
- [121] Scheer, R. (1999). Qualitative and quantitative analysis of thin film heterostructures by electron beam induced current. *Solid State Phenomena*, 67-68, 57-68.
- [122] Reuter, P., Rath, T., Fischereider, A., Trimmel, G., Hadley, P. (2011). Electron beam-induced current (EBIC) in solution-processed solar cells. *Scanning*, 33, 1-6.
- [123] Breitenstein, O., Bauer, J., Kittler, M., Arguirov, T., Seifert, W. (2008). EBIC and luminescence studies of defects in solar cells. *Scanning*, 30, 331-338.
- [124] Scheer, R., Knieper, C., Stolt, L. (1995). Depth dependent collection functions in thin film chalcopyrite solar cells. *Appl. Phys. Lett.*, 67, 3007-3009.
- [125] Kato, T., Muraoka, S., Sugimoto, H. (2011). *Cross-sectional study on Cu₂ZnSnS₄ thin-film solar cells*. Paper presented at the 21st international photovoltaic science and engineering conference, Fukuoka, Japan.
- [126] Nichterwitz, M., Unold, T. (2013). Numerical simulation of cross section electron-beam induced current in thin-film solar cells for low and high injection conditions. *J. Appl. Phys.*, 114, 134504.
- [127] Bissig, B., Guerra-Nunez, C., Carron, R., Nishiwaki, S., La Mattina, F., Pianezzi, F., Losio, P.A., Avancini, E., Reinhard, P., Haass, S.G., Lingg, M., Feurer, T., Utke, I., Buecheler, S., Tiwari, A.N. (2016). Surface passivation for reliable measurement of bulk electronic properties of heterojunction devices. *Small*, 12, 5339-5346.
- [128] Altosaar, M., Varema, T., Deppe, M., Wirts, C., Deppe, J., Hiie, J., Hiesgen, R., Mellikov, E., Meissner, D. (1996). *Monograin layers and membranes for photovoltaics*. Paper presented at the 25th Photovoltaic Specialist Conference (PVSC), Washington, D.C, USA, (p. 877).

- [129] Mellikov, E., Meissner, D., Varema, T., Hiie, J., Altosaar, M. (1997). Monograin layers as optoelectronic devices. *Proc. SPIE*, 2967, Optical inorganic dielectric materials and devices, 214-219.
- [130] Mellikov, E., Altosaar, M., Raudoja, J., Timmo, K., Volobujeva, O., Kauk, M., Krustok, J., Varema, T., Grossberg, M., Danilson, M., Muska, K., Ernits, K., Lehner, F., Meissner, D. (2012). $\text{Cu}_2(\text{Zn}_x\text{Sn}_{2-x})(\text{S}_y\text{Se}_{1-y})_4$ monograin materials for photovoltaics. In G. Wick, J. Simon, R. Zidan, E. Lara-Curzio, T. Adams, J. Zayas, A. Karkamkar, R. Sindelar, B. Garcia-Diaz (Eds.). *Materials challenges in alternative and renewable energy*. (pp. 137-141). UK: John Wiley & Sons Ltd.
- [131] International Electrotechnical Commission. (2016). Terrestrial photovoltaic (PV) modules – Design qualification and type approval – Part 1-4: Special requirements for testing of thin-film $\text{Cu}(\text{In,Ga})(\text{S,Se})_2$ based photovoltaic (PV) modules (IEC Standard No. 61215-1-4).
- [132] International Electrotechnical Commission. (2016). Terrestrial photovoltaic (PV) modules – Design qualification and type approval – Part 2: Test procedures (IEC Standard No. 61215-2).
- [133] Yin, X., Gong, H. (2012). Heat-field-stimulated decomposition reaction in $\text{Cu}_2\text{ZnSnS}_4$. *Acta Materialia*, 60, 6732-6741.
- [134] Peng, C.-Y., Dhakae, T.P., Emrani, A., Lu, S., Westgate, C.R. (2014). *Stability of CZTS thin film solar cells upon accelerated thermal cycling and damp heat exposure*. Paper presented at the 40th Photovoltaic Specialist Conference (PVSC), Denver, Colorado, USA. (p. 2022).
- [135] Darvishzadeh, P., Redzwan, G., Ahmadi, R., Gorji, N.E. (2017). Modeling the degradation/recovery of short-circuit current density in perovskite and thin film photovoltaics. *Organic Electronics*, 43, 247-252.
- [136] Darvishzadeh, P., Babanezhad, M., Ahmadi, R., Gorji, N.E. (2017). Modeling the degradation/recovery of open-circuit voltage in perovskite and thin film solar cells. *Materials and Design*, 114, 339-344.
- [137] crystalsol GmbH, Am Kanal 27, Vienna, Austria, www.crystalsol.com
- [138] Poce-Fatou, J.A., Martín, J., Alcántara, R., Fernández-Lorenzo, C. (2002). A precision method for laser focusing on laser beam induced current experiments. *Rev. Sci. Instrum.*, 73, 3895-3900.
- [139] Fernández-Lorenzo, C., Poce-Fatou, J.A., Alcántara, R., Navas, J., Martín, J. (2006). High resolution laser beam induced current focusing for photoactive surface characterization. *Appl. Surf. Sci.*, 253, 2179-2188.

- [140] Timmo, K., Kauk-Kuusik, M., Pilvet, M., Raadik, T., Altosaar, M., Danilson, M., Grossberg, M., Raudoja, J., Ernits, K. (2017). Influence of order-disorder in $\text{Cu}_2\text{ZnSnS}_4$ powders on the performance of monograin layer solar cells. *Thin Solid Films*, 633, 122-126.
- [141] Grossberg, M., Krustok, J., Raudoja, J., Raadik, T. (2012). The role of structural properties on deep defect states in $\text{Cu}_2\text{ZnSnS}_4$ studied by photoluminescence spectroscopy. *Appl. Phys. Lett.*, 101, 102102.
- [142] Grossberg, M., Salu, P., Raudoja, J., Krustok, J. (2013). Microphotoluminescence study of $\text{Cu}_2\text{ZnSnS}_4$ polycrystals. *J. Photon Energy*, 3, 030599.
- [143] Panda, R., Rathore, V., Rathore, M., Shelke, V., Badera, N., Chandra, L.S.S., Jain, D., Gangrade, M., Shripati, T., Ganesan, V. (2012). Carrier recombination in Cu doped CdS thin films: Photocurrent and optical studies. *Appl. Surf. Sci.*, 258, 5086-5093.
- [144] Petre, D., Pintilie, I., Pentia, E., Pintilie, I., Botila, T. (1999). The influence of Cu doping on opto-electronic properties of chemically deposited CdS. *Materials Science and Engineering B*, 58, 238-243.
- [145] Deng, Y., Yang, J., Yang, R., Shen, K., Wang, D., Wang, D. (2016). Cu-doped CdS and its application in CdTe thin film solar cell. *AIP Advances*, 6, 015203.
- [146] te Velde, T.S., van Helden, G.W.M.T. (1968). Monograin Layers. *Philips Technical Review*, 29, 270-274.

Acknowledgements

Throughout my studies I received support from many people, more than I can mention here. I want to express my sincere gratitude, without all of you this thesis would not have been possible.

My deep gratitude goes to my supervisor Prof. Dieter Meissner. Thank you for your help, questions, encouragement, discussions and guidance. But most important, thank you for believing in me.

Many thanks go to all of the colleagues at TalTech and crystalsol. Especially I would like to thank Dr. Tiit Varema. Since the first day I stepped into the lab you were understanding and helpful. Thank you also for training me and for being patient.

I would also like to thank Prof. Lydia Helena Wong and colleagues at Nanyang Technological University, Singapore. I sincerely appreciate your warm welcoming, the experience and all I learned.

Special thanks go to Dr. Kaia Ernits and Ms. Elina Tasa for helping with Estonian language.

Financial support by the European Social Fund's Doctoral Studies and Internationalisation Programme DoRa, the Estonian Research Council (projects PUT265, IUT19-28, IUT19-28, IUT-T4) and the European Regional Development Fund (projects TK141, IRESOL 2014-2020.4.02.17-0083, TAR16016 and the Mobilitas Pluss Postdoctoral Researcher Grant MOBJD308) is gratefully acknowledged.

My deepest gratitude goes to my family, friends and loved ones. Your continuous support throughout the years kept me going.

Abstract

Spatially Resolved Opto-electronical Investigations of Monograin Layer Solar Cells

Photovoltaics is expected to play a major role in the future energy systems worldwide. The pentanary p-type semiconductor material $\text{Cu}_2\text{ZnSn}(\text{S}_x\text{Se}_{1-x})_4$, due to the preferably formed crystal structure also called Kesterite, is believed to be a suitable absorber material for photovoltaic applications. It utilizes earth abundant and non-toxic raw materials and has additional advantages such as a direct bandgap which can be tuned by the S:Se ratio, a high absorption coefficient, and a low temperature coefficient. Therefore Kesterites can possibly substitute other commercially utilized absorber materials such as CdTe and CIGS, which employ scarce metals such as Te, In or Ga.

Photovoltaic devices with Kesterites as absorber material are mainly manufactured by conventional thin film techniques such as sputtering, co-evaporation, spray-pyrolysis and other solution based processes. In this thesis material and devices produced in a so-called monograin technology are investigated. For this technology, Kesterite powders consisting of grains with diameters of several ten micrometers are synthesized. After coating their surface with an n-type semiconductor material such as CdS, every crystal has a fully functional p-n-junction. This approach as developed in crystalsol OÜ in Tallinn, Estonia, yields a high quality product, which can be further utilized in various module production manufacturing processes. As an example an industrial and cost effective roll-to-roll (R2R) process for producing modules was developed in crystalsol GmbH in Vienna, Austria. A pilot R2R manufacturing line using Tallinn's Kesterite monograin powder is in operation here.

Research in recent years led to continuous improvement of the Kesterite material. For conventional thin film technologies a conversion efficiency of 12.6 % was reported in the literature. A crystalsol solar cell was certified in a calibration lab with a conversion efficiency of 9.5 % utilizing crystalsol's Kesterite monograins. Due to their semi-transparent membrane structure the "material efficiency" can be calculated to be around 12 %. However, these efficiencies are still much lower than those obtained from devices employing CdTe or CIGS as absorber materials, for which efficiencies up to 22.1 % and 22.9 % are reported, respectively.

Another important parameter is the long-term stability of the materials and cells. Stability values and related degradation processes of the Kesterites are poorly covered in literature. However, long term stability is crucial for a successful market implementation of the Kesterite technology in photovoltaics.

This thesis describes the development of new methodologies for investigating Kesterite monograin layer (MGL) devices by different spatially resolved opto-electrical analysis techniques. The focus hereby lies on methods such as light beam induced current, electron beam induced current and electroluminescence imaging. By utilizing these techniques in combination with various complementary investigation techniques such as current-voltage analysis, photoluminescence, external quantum efficiency, scanning electron microscopy, transmission measurements, X-ray photoelectron spectrometry, Kelvin probe and Raman measurements, performance reducing effects of Kesterite MGL devices are investigated and analyzed. The analysis of ageing processes and their mechanisms of the devices is another focus of this work.

The results obtained show that the determination of the real electrically active area and the identification of its reduction within a MGL device is important for a correct

evaluation of the material performance. Additionally it is revealed that inhomogeneities in the monograins can be one major reason for the reduction of device performances. A difference in the p-n-junction formation and related barrier height fluctuations were identified as such inhomogeneities. Investigations on differently aged samples with different Kesterite absorber materials led to the identification of a diffusion mechanism involved in ageing processes of unstable Kesterite solar cells. It was found that copper diffusion plays a crucial role in these processes.

The presented and discussed results contribute to further understanding and improvement of Kesterite solar cells and shows possibilities of quality control for photovoltaic device manufacturing, also in post-production steps. The investigation of ageing and the proposed mechanism build a foundation for further investigations of this topic for all Kesterite solar cells, also including thin film technologies, and even for other photovoltaic materials and solar cell types.

Kokkuvõte

Monoterliste päikesepatareide ruumilise lahutusega optoelektronsed uuringud

Päikesepatareidele on energiasüsteemide tulevikus suured ootused ja seda ülemaailmselt. Mitmekomponentset p-tüüpi pooljuhtmaterjali, $\text{Cu}_2\text{ZnSn}(\text{S}_x\text{Se}_{1-x})_4$, peetakse sobivaks absorbermaterjaliks päikesepatareides tänu tema sobivale kristallstruktuurile, mida kutsutakse ka kesteriidiks. See materjal koosneb maakoos keskkonnas leiduvatest ja mittetoksislistest lähtematerjalidest, lisaks on tal sellised sobivad omadused nagu otsene keelutsoon, mille laiust on võimalik muuta varieerides S:Se suhet, suur neeldumiskoeffitsient ja väike temperatuurikoeffitsient. Seetõttu võiks kesteriidiga asendada selliseid senituntud ja kasutatud absorbermaterjale nagu CdTe ja CIGS, mille koostises on harvaesinevaid metalle nagu Te, In ja Ga.

Enamjaolt on kesteriidsetest absorbermaterjalidest valmistatud päikesepatareid toodetud üldtuntud õhukeste kilede valmistamise tehnikatega nagu tolmustamine, koos-aurustamine, pihustuspürolüüs ning muude lahuseliste protsessidega. Käesolevas doktoritöös uuritavad materjalid ja päikesepatareid on valmistatud nn monoter tehnoloogiat kasutades. Selle tehnoloogia tarvis on sünteesitud kesteriidne pulber, mis koosneb mitmekümne mikromeetri diameetriga teradest. Peale p-tüüpi terade pinna katmist ühtlase n-tüüpi pooljuhtmaterjalist kilega, nagu CdS, on igal teral töötav p-n üleminek. Selline lähenemine on välja töötatud Eestis, Tallinnas asuvas firmas OÜ crystalsol, tulemuseks on hea kvaliteediga toode, mida saab hiljem kasutada erinevates päikesepaneelide tootmisprotsessides. Näiteks arendati selle tehnoloogia baasil Austrias, Viinis asuvas GmbH crystalsolis, tööstuslik ja tasuv „roll-to-roll“ printimisliini päikesepatarei moodulite tootmiseks. See piloot-tootmisliin kasutab Tallinnas valmistatud kesteriidipulbrit.

Viimastel aastatel aset leidnud uuringud on taganud kesteriidse materjali pideva arengu. Üldtuntud õhukesekilise tehnoloogia baasil valmistatud päikesepatareid on saavutanud 12.6 % suuruse kasuteguri. Crystalsoli poolt valmistatud kesteriidist monoteradest päikesepatareil mõõdeti rahvusvahelises kalibreerimislaboratooriumis 9.5 % kasuteguriks. Kuna monoterakihiline päikesepatarei on osaliselt läbipaistev ja membraan on kaetud vaid osaliselt absorbermaterjaliga, siis saame materjali enda kasuteguriks umbes 12 %. Sellegipoolest on need kasuteguri väärtused märgatavalt madalamad CdTe või CIGS päikesepatareide kasuteguritest, mis küündivad vastavalt 22.1 % ja 22.9 % väärtusteni.

Veel on üheks oluliseks parameetriks materjalide ning päikesepatareide stabiilsus. Kesteriidmaterjali stabiilsuse väärtused ja sellega seotud vananemisprotsessid on kirjanduses seni puudulikult kajastatud. Vaatamata sellele, on patareide pikaajaline kestvus hädavajalik kesteriidmaterjalide tehnoloogia edu tagamiseks päikesepatarei turul.

Käesolevas doktoritöös kirjeldatakse uute meetodikate arendust kesteriidist monoterakihiliste päikesepatareide uurimiseks erinevate opto-elektriliste analüüsitehnikatega. Seega keskendutakse peamiselt taoliste meetodite nagu valgusvihi tekitatud vool, elektronvihi tekitatud vool ja elektroluminesentsi kujutamine. Kasutades neid analüüsitehnikaid koos täiendavate uurimismeetoditega nagu voolu-pinge analüüs, fotoluminesents, väline kvantefektiivsus, skaneeriv elektronmikroskoopia, läbipaistvuse mõõtmised, röntgenkiirte fotoelektronkiirte spektromeetria, Kelvini sond ja Raman mõõtmised, uuriti ning analüüsiti

kesteriitmaterjalist päikesepatarei kvaliteeti vähendavaid effekte. Täiendavalt on keskendunud päikesepatareide vanemisprotsessi ning selle mehhanismide analüüsimisele.

Saadud tulemused näitavad, et tegeliku elektriliselt aktiivse pindala määramine ja selle kasutamine monotera päikesepatarei parameetrite kalkuleerimiseks, on vajalikud materjali kvaliteedi adekvaatseks hindamiseks. Samuti selgus, et ebaühtlused monoterade kvaliteedis võivad olla peamiseks põhjuseks päikesepatarei kasuteguri vähenemisel. Need ebaühtlused monotera päikesepatareides leiti olevat peamiselt põhjustatud p-n ülemineku varieeruvusest piirkonniti ja sellega seotud barjääri suuruse kõikumistest. Tänu erineval viisil vanandatud objektide uuringutele erinevate kesteriitsete materjalidega identifitseeriti ebastabiilsete päikesepatareide vanemisprotsessist osavõttev difusioonimehhanism. Leiti, et vase difusioon mängib nendes protsessides otsustavat rolli.

Siin esitatud ja arutatud tulemused on oluliseks panuseks kesteriitsetest materjalidest päikesepatareide mõistmiseks ning on aluseks jätkuvale parendamisele, samuti on leitud võimalusi päikesepatarei tootmise ning järeltöötuse kvaliteedikontrolliks. Vanemise ning sellega seotud võimalike mehhanismide uuringud on loonud pinnase mitte ainult kõikide kesteriitmaterjalidel baseeruvate päikesepatareide edasiste uuringute jaoks, vaid ka õhukese-kilelistel tehnoloogiatel baseeruvate ning miks ka mitte teiste päikesepatarei materjalide ja päikesepatarei tüüpide jaoks.

Appendix

Paper I

Neubauer, C., Babatas, E., Meissner, D. (2017). Investigation of rough surfaces on $\text{Cu}_2\text{ZnSn}(\text{S}_x\text{Se}_{1-x})_4$ monograin layers using light beam induced current measurements. *Appl. Surf. Sci.*, 423, 465-468.



Contents lists available at ScienceDirect

Applied Surface Science

journal homepage: www.elsevier.com/locate/apsusc

Short communication

Investigation of rough surfaces on $\text{Cu}_2\text{ZnSn}(\text{S}_x\text{Se}_{1-x})_4$ monograin layers using light beam induced current measurements

Christian Neubauer^{a,b,*}, Ertug Babatas^a, Dieter Meissner^{a,b}^a Department of Materials and Environmental Technology, Tallinn University of Technology, Ehitajate tee 5, 19086, Tallinn, Estonia^b crystalsol OÜ, Akadeemia tee 15a, 12618, Tallinn, Estonia

ARTICLE INFO

Article history:

Received 31 January 2017

Received in revised form 7 June 2017

Accepted 8 June 2017

Available online 15 June 2017

Keywords:

LBIC

CZTS

Monograin

Photovoltaics

ABSTRACT

Monograin technology has proven to be a successful way of manufacturing low cost photovoltaic applications using the pentanary $\text{Cu}_2\text{ZnSn}(\text{S}_x\text{Se}_{1-x})_4$ (CZTSSe) as an absorber material in an industrial roll-to-roll process. For high efficient CZTSSe monograin device fabrication a thorough understanding of the impacts of the device characteristics and surface structure is important. A new evaluation method of Light Beam Induced Current (LBIC) images had to be developed to distinguish between different effects resulting from different surface orientations, grain sizes, packing densities and contacting areas. In this work we will show that with LBIC measurements it is possible to evaluate the quality and differences in produced CZTSSe monograin cells in a post-production and non-destructive step. The high spatial resolution evaluation allows investigating the homogeneity of single crystalline grains as well as certain areas of a CZTSSe device. By introducing a statistical method the active area as a major factor for the current density of a device will be calculated and evaluated. The results show that with LBIC measurements the active area can be quantified, which differs for the investigated cells up to 9%. Additionally, the homogeneity of short circuit current densities of the monograins and also of certain areas of a cell can be detected and quantified.

© 2017 Elsevier B.V. All rights reserved.

1. Introduction

The Indium-free semiconductor material CZTSSe gained attention in recent years in photovoltaics as a possibility to substitute $\text{Cu}(\text{In,Ga})\text{Se}_2$ (CIGS) as an absorber material for photovoltaics. The formation of CZTSSe thin films with different S:Se ratios were reported to be achieved by different deposition technologies, most commonly by co-evaporation [1], sputtering [2], pulsed laser deposition [3,4], spray pyrolysis [5] and electrodeposition [6,7]. A conversion efficiency above 10% for CZTSSe was first reported by using an hydrazine-based liquid process [8], which could be further improved to reach a conversion efficiency of 12.6% [9]. With the monograin monolayer technology it is possible to utilize this material in a low cost roll-to-roll process [10]. Conversion efficiencies of the photovoltaically active material can be derived from the product of the measured cell efficiency of more than 8% [11] and the Active Area Ratio (AAR, see below) of about 70% to be in the order of

11% so that the material quality is in the same order as of thin films. The use of monograins applied in a monolayer results in a unique surface with the monograin crystals partially standing out of the embedding material which form a three-dimensional photoactive surface area. Still a detailed understanding of the surface and interface properties is crucial for high efficient photovoltaic devices. LBIC measurements as an investigation method are widely used for the characterization of polycrystalline silicon cells [12–16], but also in float zone [17] and amorphous [18] silicon devices as well as other photosensitive applications or semiconductor materials in photovoltaics [19–22]. The use of LBIC for the definition of the active area of dye-sensitized solar cells (DSSCs) was reported [23]. For analyzing rough surfaces such as monograin monolayer devices and their high number of parallel-connected single crystals, LBIC provides a suitable method to investigate the behavior of different crystals as well as different areas in single crystals and the interface between grains and the embedding polymer.

2. Experimental

CZTSSe monograins were produced in a molten salt followed by deposition of cadmium sulfide (CdS) as buffer layer by chemical bath deposition (CBD). A more detailed description of the process is

* Corresponding author at: Department of Materials and Environmental Technology, Tallinn University of Technology, Ehitajate tee 5, 19086, Tallinn, Estonia.

E-mail addresses: c.neubauer@hotmail.com, christian.neubauer@crystalsol.com (C. Neubauer).

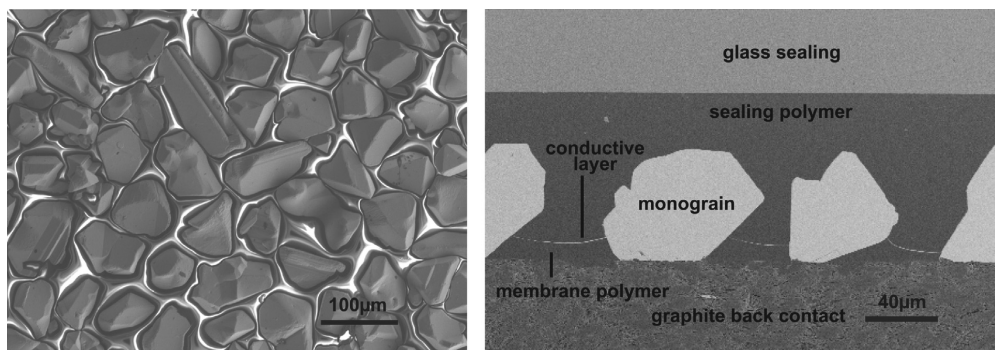


Fig. 1. SEM surface image of a single-layer monograin layer embedded into polymer (left) and a SEM cross-section image of a monograin layer photovoltaic device (right).

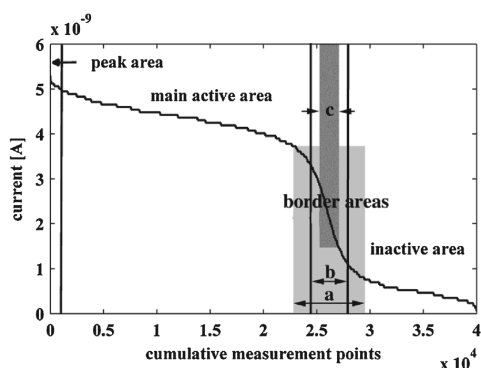


Fig. 2. Definition of characteristic areas of a small area of sample 1, where all measurement points are counted with the corresponding current response in descending order. The different definition widths of the border area are indicated as a, b and c and correspond to the parts a, b and c in Fig. 3.

published elsewhere [24]. The composition of the monograins was determined by EDX measurements to be $\text{Cu}_{1.76}\text{Zn}_{0.92}\text{Sn}_{1.52.96}\text{Se}_{0.71}$. By sieving the grains a more homogenous size distribution for later manufacturing steps for producing photovoltaic devices was achieved. By embedding the monograins into a polymer a single-layer monograin layer was formed (Fig. 1 left).

The device was finished by sputtering window layers of intrinsic and aluminum-doped zinc oxide (i-ZnO, ZnO:Al) on the front side, followed by an application of a layer of silver nanowires to enhance the surface cross-conductivity. The device was sealed by gluing soda lime glass onto this structure. By etching the polymer of the backside with sulfuric acid followed by sand paper abrasion,

the CZTSSe bulk was opened and contacted with graphite paste for establishing Ohmic back contacts.

The samples were chosen due to their high difference in electric parameters, especially of the short circuit current density (j_{sc}) measured. Variations of j_{sc} can originate from different reasons, one of them being a variation in the photovoltaically active area. Areas within a monograin layer without grains as well as grains with no electric front or back contact reduce the active area and thus lead to a reduced j_{sc} . By LBIC investigations applying the developed method it is possible to identify some major causes for a reduced j_{sc} .

The LBIC measurements were conducted with a red (632.81 nm) laser, focused through a 50x lens and measured with a lock in amplifier. The laser spot diameter in respect to the focus setting was evaluated by using a sharp edge (front contact finger) of a monocrystalline silicon cell, similar as described in [25,26], and was determined to be minimal 5 μm . The resulting light intensity of the laser was determined to be 0.53 suns.

3. Results and discussion

By ordering and plotting the measurement points from the LBIC measurements by the short circuit current values, specific areas become visible which are hereafter defined as peak area, main active area, border area and inactive area (Fig. 2). The “peak area” represents the number of measurement points with a very high efficiency, i.e. a short circuit current being clearly higher than the majority of the active measurement points. This majority defines the “main active area”. In the “border area” all measurement points are found measured where the laser spot is just partly on an active grain. It thus separates the active from the inactive area. In the “inactive area” there is either no CZTSSe grain or the grain does not have an electric contact on the front or backside. The small

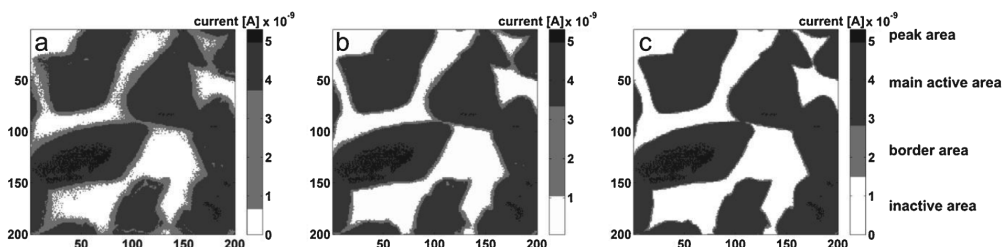


Fig. 3. Constructed LBIC images of the small area of sample 1 evaluated in Fig. 2, with a scale divided into characteristic areas (see text). The data correspond to the measurement values presented in Fig. 2. The units of the axis are measurement steps with a set step width of 1 μm .

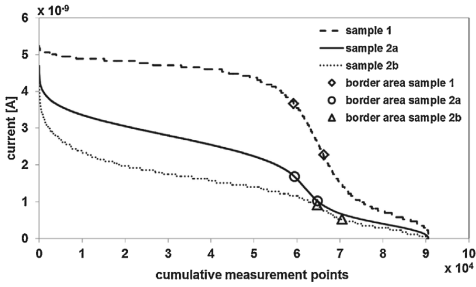


Fig. 4. Cumulative measurement points of LBIC measurements on samples 1, 2a and 2b with indicated border areas.

current response in this inactive area results from optical effects, where part of the laserlight is reflected from the polymer surface or refracted or scattered from the sealing material and its possible defects to nearby active grains. Constructing LBIC images (Fig. 3) from the measured data and applying scales as defined in Fig. 2 the defined areas become visible. The exact position of the borders between these “areas” in Fig. 2 (vertical lines) is arbitrary. The number of measurement points within the 3 different defined border areas shown in Fig. 2 and 3(a, b and c) differ each by approximately the factor 2. While the high number of measurement points within border area “a” leads to an overestimated border area due to a response from the inactive and main active area, the small number of measurement points of the defined border area “c” leads to a border area thickness below the laser spot diameter and thus is defined as too small. The defined border area “b” however presents a realistic estimation of the size.

To determine the size of the “active area” with respect to the total area the Active Area Ratio (AAR) is defined as described in equation 1, where n_p is the number of measurement points of the “peak area”, n_m the number of measurement points of the “main active area”, n_b is the number of measurement points of the “bor-

Table 2
AAR of the investigated samples.

sample 1	sample 2a	sample 2b
69	68	75

der area” and n the total number of measurement points of the measured area.

$$AAR = \frac{n_p + n_m + n_b/2}{n} \times 100\% \tag{1}$$

The definition of the width of the border area affects the calculated AAR just to a minor extent. In the cases presented in Fig. 2 and 3 with the big differences in the defined border areas a, b and c the AAR showed differences below 0.2 percent points.

The slope of the graph of the cumulated measurement points, mainly in the main active area, but also in the peak area, correlate with the homogeneity regarding j_{sc} of the monograins and the material of a single crystal. The width of the border area depends on the laser spot profile while the total number of measurement points contributing to the border area gives an indication of the grain size. The relation between the number of measurement points in the border area and the grain size can be explained by the nonlinear ratio of the circumference to the average diameter of polygons. However, this correlation is just a coarse one taking into account that the definition of the border area gets more difficult for data with lower signal strength and is arbitrary within limits.

In Fig. 4 the LBIC measurements of samples 1, 2a and 2b are shown. While the difference of the current response in the main active area is clearly visible, a difference of the current values of the peak area is noticeable but in a smaller range. The different slopes of the curves in the main active area indicate that sample 1 has a more homogenous current response compared to sample 2a and 2b. The number of measurement points of the border area in sample one (7027 measurement points) is bigger compared to sample 2a (5333 measurement points) and 2b (5684 measurement points) which correlates to the average grain diameter of the samples (Table 1)

Table 1
jV-measurement results of the analyzed samples.

	Av. grain diameter [μm]	area [mm ²]	Voc [V]	FF [%]	j_{sc} [mA/cm ²]	Eff [%]
sample 1	69	3.90	0.688	55.8	15.6	6.0
sample 2a	85	4.29	0.643	41.3	9.05	2.4
sample 2b	85	2.39	0.629	42.8	7.07	1.9

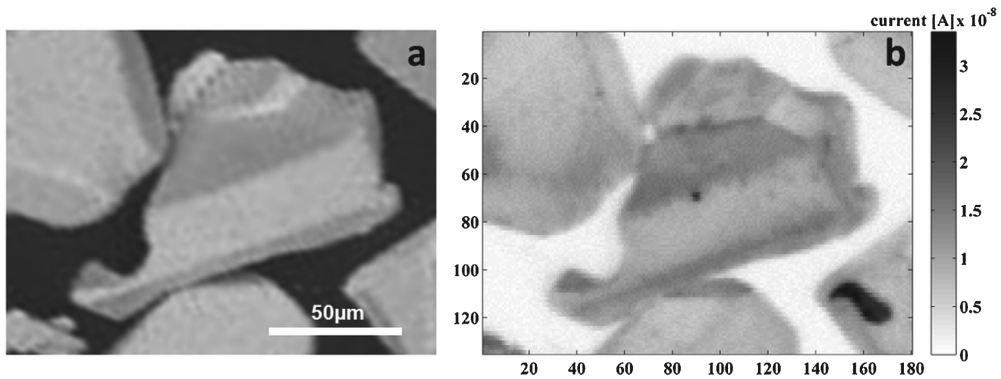


Fig. 5. SEM (a) and LBIC (b) image of a small area of sample 2b. The units of the axis of the LBIC image are measurement steps.

due to the different ratios of border area to grain size as shown above.

In Table 2 the AAR for all 3 investigated samples is presented. The difference between sample 1 and sample 2a is rather small, while sample 2b shows a considerable higher AAR than the previous ones. From these values it is evident that the main reason for the high difference of j_{sc} between the samples is not a difference of the active area.

Fig. 5 shows a SEM and LBIC image of a small area of sample 2b. In the SEM image different planes can be detected. These planes show also a different current response in the LBIC measurement, where additionally certain areas with a very high current can be seen. One important reason for these differences in the current density is their different orientation towards the incoming laser beam and thereby different reflection losses. However, as will be shown in the full paper, corresponding differences can also be seen in the electroluminescence, as will be discussed there.

4. Conclusions

A quantitative Analysis of LBIC as a spatial investigation method on the rough surface of CZTSSe monograin layer photovoltaic devices requires the development of a statistical analyzing method. By applying this method it is possible to evaluate the quality and homogeneity of different monograins as well certain areas of a single grain within a device, which affects the performance of photovoltaic cells. The calculation of an Active Area Ratio (AAR) gives insight in the active area and allows conclusions on the reasons for differences of short circuit current densities of the investigated monograin layer devices. The results show that the performances of the investigated devices differ due to current in homogeneities, while the active area as a reason for low performances can be excluded.

Acknowledgements

Valuable discussions with TUT researchers and colleagues Jüri Krustok, Tiit Varema, Elham Kouhiifahani, Ali Samieipour, Semjon Galajev is gratefully acknowledged. This work was financially supported by Archimedes/DoRa and the Estonian Research Council in PUT265 (1–2.10/13/39) and by the European Union through the European Regional Development Fund, Project TK141 “Advanced materials and high-technology devices for energy recuperation systems”.

References

- [1] G. Suresh Babu, Y.B. Kishore Kumar, P. Uday Bhaskar, V. Sundara Raja, Effect of Cu/(Zn+Sn) ratio on the properties of co-evaporated Cu₂ZnSnSe₄ thin films, *Sol. Energy Mater. Sol. Cells* 94 (2010) 221–226.
- [2] B.S. Sengar, V. Garg, V. Awasthi, S. Aaryashree, C. Kumar, M. Mukherjee, S. Gupta, Growth and characterization of dual ion beam sputtered Cu₂ZnSn(S, Se)₄ thin films for cost-effective photovoltaic application, *Sol. Energy* 139 (2016) 1–12.
- [3] M.R. Byeon, E.H. Chung, J.P. Kim, T.E. Hong, J.S. Jin, E.D. Jeong, J.S. Bae, Y.D. Kim, S. Park, W.T. Oh, Y.S. Huh, S.J. Chang, S.B. Lee, I.H. Jung, J. Hwang, The effects for the deposition temperature onto the structural, compositional and optical properties of pulsed laser ablated Cu₂ZnSnS₄ thin films grown on soda lime glass substrates, *Thin Solid Films* 546 (2013) 387–392.
- [4] L. Sun, J. He, H. Kong, F. Yue, P. Yang, J. Chu, Structure, composition and optical properties of Cu₂ZnSnS₄ thin films deposited by Pulsed Laser Deposition method, *Sol. Energy Mater. Sol. Cells* 95 (2011) 2907–2913.
- [5] H. Yoo, J. Kim, Comparative study of Cu₂ZnSnS₄ film growth, *Sol. Energy Mater. Sol. Cells* 95 (2011) 239–244.
- [6] J.J. Scragg, P.J. Dale, L.M. Peter, Synthesis and characterization of Cu₂ZnSnS₄ absorber layers by an electrodeposition-annealing route, *Thin Solid Films* 517 (2009) 2481–2484.
- [7] C.P. Chan, H. Lam, C. Surya, Preparation of Cu₂ZnSnS₄ films by electrodeposition using ionic liquids, *Sol. Energy Mater. Sol. Cells* 94 (2010) 207–211.
- [8] D.A.R. Barkhouse, O. Gunawan, T. Gokmen, T.K. Todorov, D.B. Mitzi, Device characteristics of a 10.1% hydrazine-processed Cu₂ZnSn(Se,S)₄ solar cell, *Prog. Photovolt. Res. Appl.* 20 (2012) 6–11.
- [9] W. Wang, M.T. Winkler, O. Gunawan, T. Gokmen, T.K. Todorov, Y. Zhu, D.B. Mitzi, Device characteristics of CZTSSe thin-film solar cells with 12.6% efficiency, *Adv. Energy Mater.* 4 (2014) 1–5.
- [10] D. Meissner, Photovoltaics based on semiconductor powders, in: A. Méndez-Vilas (Ed.), *Mater. Process. Energy Commun. Curr. Res. Technol. Dev.*, Formatec Research Center, Badajoz, Spain, 2013 (p. 114).
- [11] E. Mellikov, M. Altsaar, M. Kaul-Kuusik, K. Timmo, D. Meissner, M. Grossberg, J. Krustok, O. Volobujeva, Growth of CZTS-Based Monograins and Their Application to Membrane Solar Cells, chapter 13, in: Kentaro Ito (Ed.), *Copper Zinc Tin Sulfide-Based Thin-Film Solar Cells*, John Wiley & Sons Ltd, Chichester, UK, 2015, pp. 289–309.
- [12] M.P. Peloso, J. Sern Lew, T. Trupke, M. Peters, R. Utama, A.G. Aberle, Evaluating the electrical properties of silicon wafer solar cells using hyperspectral imaging of luminescence, *Appl. Phys. Lett.* 99 (2011) 97–99.
- [13] K. Nishioka, T. Yagi, Y. Uraoka, T. Fuyuki, Effect of hydrogen plasma treatment on grain boundaries in polycrystalline silicon solar cell evaluated by laser-beam-induced current, *Sol. Energy Mater. Sol. Cells* 91 (2007) 1–5.
- [14] W. Dimassi, M. Bouaicha, H. Nouri, M.F. Boujmil, S. Ben Nasrallah, B. Bessaïs, Grooving of grain boundaries in multycrystalline silicon: effect on solar cell performance, *Nucl. Instruments Methods Phys. Res. Sect. B* 253 (2006) 260–263.
- [15] J.P. Boyeaux, A. Kaminski, A. Fave, A. Laugier, Local characterization of large area multycrystalline solar cells by non-destructive mapping, *Mater. Sci. Semicond. Process.* 4 (2001) 261–263.
- [16] L. Khezami, A.O. Al Megbel, A.B. Jemai, M. Ben Rabha, Theoretical and experimental analysis on effect of porous silicon surface treatment in multycrystalline silicon solar cells, *Appl. Surf. Sci.* 353 (2015) 106–111.
- [17] J.J. Simon, L. Périchaud, N. Burle, M. Pasquinelli, S. Martinuzzi, Influence of phosphorus diffusion on the recombination strength of dislocations in float zone silicon wafers, *J. Appl. Phys.* 80 (1996) 4921–4927.
- [18] C. Eisele, C.E. Nebel, M. Stutzmann, Spatially resolved photocurrent measurements of microstructured a-Si:H solar cells, *J. Non. Cryst. Solids* 266–269 (2000) 1109–1110.
- [19] F.X. Zha, S.M. Zhou, H.L. Ma, F. Yin, B. Zhang, T.X. Li, J. Shao, X.C. Shen, Laser drilling induced electrical type inversion in vacancy-doped p-type HgCdTe, *Appl. Phys. Lett.* 93 (2008) 20–22.
- [20] H. Gebretsadik, K. Zhang, K. Kamath, X. Zhang, P. Bhattacharya, Recombination characteristics of minority carriers near the Al_xO_y/GaAs interface using the light beam induced current technique, *Appl. Phys. Lett.* 71 (1997) 3865–3867.
- [21] F.J. Navas, R. Alcántara, C. Fernández-Lorenzo, J. Martín-Calleja, High resolution laser beam induced current images under trichromatic laser radiation: approximation to the solar irradiation, *Rev. Sci. Instrum.* 81 (2010) 035108.
- [22] C. Xu, W. Denk, Two-photon optical beam induced current imaging through the backside of integrated circuits, *Appl. Phys. Lett.* 71 (1997) 2578–2580.
- [23] T.W. Jones, K. Feron, K.F. Anderson, B.C. Duck, G.J. Wilson, An applied light-beam induced current study of dye-sensitized solar cells: photocurrent uniformity mapping and true photoactive area evaluation, *J. Appl. Phys.* 116 (2014) 043104.
- [24] M. Nguyen, K. Ernits, K.F. Tai, C.F. Ng, S.S. Pramana, W.A. Sasangka, S.K. Batabyal, T. Holopainen, D. Meissner, A. Neisser, L.H. Wong, ZnS buffer layer for Cu₂ZnSn(SSe)₄ monograin layer solar cell, *Sol. Energy* 111 (2015) 344–349.
- [25] J.A. Poce-Fatou, J. Martín, R. Alcántara, C. Fernández-Lorenzo, A precision method for laser focusing on laser beam induced current experiments, *Rev. Sci. Instrum.* 73 (2002) 3895–3900.
- [26] C. Fernández-Lorenzo, J.A. Poce-Fatou, R. Alcántara, J. Navas, J. Martín, High resolution laser beam induced current focusing for photoactive surface characterization, *Appl. Surf. Sci.* 253 (2006) 2179–2188.

Paper II

Neubauer, C., Samiepour, A., Oueslati, S., Ernits, K., Meissner, D. (2018). Spatially resolved opto-electrical performance investigations of $\text{Cu}_2\text{ZnSnS}_{3.2}\text{Se}_{0.8}$ photovoltaic devices. *Energy Sci Eng.*, 6, 563-569.

RESEARCH ARTICLE

Spatially resolved opto-electrical performance investigations of $\text{Cu}_2\text{ZnSnS}_{3.2}\text{Se}_{0.8}$ photovoltaic devices

Christian Neubauer^{1,2} | Ali Samiepour¹ | Souhaib Oueslati^{1,2} | Kaia Ernits² | Dieter Meissner^{1,2} 

¹Department of Materials and Environmental Technology, Tallinn University of Technology, Tallinn, Estonia

²crystalsol OÜ, Tallinn, Estonia

Correspondence: Dieter Meissner, Department of Materials and Environmental Technology, Tallinn University of Technology, Ehitajate tee 5, 19086 Tallinn, Estonia (profdieter@gmail.com).

Funding information

European Regional Development Fund, Grant/Award Number: 2014-2020.4.02.17-0083 and TK141; Sihtasutus Archimedes; Mobilias Pluss Postdoctoral Researcher, Grant/Award Number: MOBJD308

Abstract

A new statistical analysis of spatially resolved photocurrent and electroluminescence images has been developed and applied to $\text{Cu}_2\text{ZnSn}(\text{S}_x\text{Se}_{1-x})_4$ (CZTSSe) monograin solar cells. CZTSSe as an absorber material has the potential to significantly reduce manufacturing costs and develop new application fields in photovoltaics. Deep understanding of the performance related parameters in various production steps is crucial for further development of the technology. In this paper we show that by a thorough investigation by means of a combination of opto-electrical measurement methods such as light beam induced current mapping, scanning electron microscopy, optical microscopy, photoluminescence, and electroluminescence measurements a correlation with different current-voltage (j/V) measurement parameters can be established. Hereby, we clearly identify barrier variations at the active interface as the main reason for current variations across the cell, which for record cells can largely be avoided. These variations show up clearly in the microscopic spatial analysis developed. The detailed analysis of the homogeneity of the solar cell photocurrent presented in this study is relevant for all kinds of solar cells including thin-film and wafer-based cells.

KEYWORDS

electroluminescence, kesterite, LBIC, monograin, photoluminescence, photovoltaics

1 | INTRODUCTION

The pentanary absorber material CZTSSe gained attention in recent years as a possible indium- and gallium-free substitute for $\text{Cu}(\text{In,Ga})\text{Se}_2$ (CIGS) in photovoltaic applications. The conversion efficiency of a thin film device based on a hydrazine-based liquid process was reported to be 12.6%.¹ By using the monograin technology it is possible to utilize this absorber material in a cost effective industrial roll-to-roll process.² Efficiencies of up to 9.5%³ of CZTSSe monograin layer (MGL) devices with an approximate active area ratio

(AAR) of about 80% were certified. The evaluation of the AAR was described in details in a previous paper.⁴ The conversion efficiency of the active CZTSSe material is in the range of 12% which is comparable to the record efficiencies measured for thin film devices. As demonstrated in the Supporting Information the record cell is of remarkable photocurrent homogeneity within $\pm 3\%$.

Despite the beneficial properties such as a direct tunable bandgap, high absorption coefficient and low temperature coefficient,⁵⁻⁷ the efficiency of photovoltaic applications with CZTSSe as absorber is still considerably smaller than

This is an open access article under the terms of the Creative Commons Attribution License, which permits use, distribution and reproduction in any medium, provided the original work is properly cited.

© 2018 The Authors. *Energy Science & Engineering* published by the Society of Chemical Industry and John Wiley & Sons Ltd.

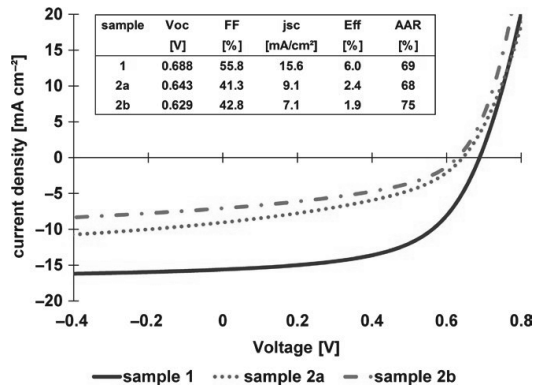


FIGURE 1 j/V measurement and parameters including active area ratio (AAR) of samples 1, 2a, and 2b

the record efficiency of CIGS, which was reported to be 22.6%.⁸ Several possible reasons for a reduction of device performance parameters such as open circuit voltage (V_{oc}) and short circuit current density (j_{sc}) of CZTSSe compared to CIGS thin film photovoltaic devices were reported in the literature and summarized by Aninat et al.⁹

To tackle performance reducing effects in CZTSSe MGL devices we combined several opto-electrical analyzing methods such as light beam induced current (LBIC) mapping, scanning electron microscopy (SEM), photoluminescence (PL), electroluminescence (EL), and transmission measurements.

First results of LBIC analysis on the here investigated devices have been published in a recent paper,⁴ in which a statistical analysis was developed allowing to analyse the active and inactive areas. Additionally an inhomogeneous current density distribution had been observed. To evaluate the reason for these inhomogeneities and performance reducing effects we extended the investigation by including additional analysis methods. Using these techniques several suspected parameters such as locally different reflection or transmission of the layers on top of CZTSSe as well as resistance differences can be eliminated as a cause for major performance differences in MGL devices. Instead variations in the p - n -heterojunction barrier height can be identified as causing these variations.

2 | EXPERIMENTAL

CZTSSe monograins are synthesized from copper, zinc sulfide, zinc selenide, tin, and sulfur precursors in potassium iodine (KI) as flux material as described in detail in previous papers.^{2,6} After the synthesis of the CZTSSe monocrystals a washing procedure with water removes the KI, after which the powder is

dried and sieved to obtain powders of desired grain sizes. This is followed by a heat treatment step at 740°C and the deposition of cadmium sulfide (CdS) by chemical bath deposition employing cadmium acetate as cadmium source and thiourea as sulfur source in an ammonia solution. A more detailed description of the synthesis and post treatment processes of CZTSSe monograins can be found elsewhere.¹⁰ By partial embedding monograins in a thin layer of polymer a so-called MGL is formed. The front contact is established by sputtering a transparent conductive oxide (TCO) layer (intrinsic and aluminum doped zinc oxide). The conductivity of the TCO is enhanced by applying a thin layer of silver nanowires and a current collector made by silver paste allows the establishment of a reliable contact for electrical measurements. By gluing the MGL with transparent polymer on soda lime glass the front side is sealed. For establishing back contacts the samples are dipped into concentrated sulfuric acid to etch the surface of the embedding polymer on the backside which makes the monograins in the MGL easily accessible, followed by an abrasion process by sand paper to open the monograins. By pasting graphite onto the abraded backside Ohmic back contacts are established. SEM images of single grains after applying a graphite layer embedded in polymer and a cross-section of a finished device can be found elsewhere.⁴ The LBIC, EL-spectra and PL-spectra investigations are conducted by means of a Horiba Jobin Yvon Labram HR800 instrument, Horiba Ltd, Kyoto, Japan. As excitation source a red (633 nm) laser is used for the LBIC measurements and a green (532 nm) laser for the PL measurements respectively. The intensity of the excitation laser is adjusted by neutral gray filters, which reduces the light intensity to around 0.013 and 0.08 μ W for the LBIC and to 2.8 mW for the PL measurements. The illuminated area is evaluated to be around 20 μ m². The LBIC current is measured by means of a lock-in amplifier and a scanning rate of around 10 measurement points per second is used. The exposure time during EL and PL measurements is 30 and 3 seconds respectively. The wavelength dependent transmission analysis of a monograin monolayer and the corresponding polymer layer is conducted by a Newport Oriel 300W Xenon lamp with a Cornerstone 260 Monochromator, silicon detector and a Merlin radiometer system, all from Newport Corporation, Stratford, CT. A Nikon SMZ 745T optical microscope, Nikon Corporation, Tokyo, Japan, is used for transmission imaging. EL imaging is conducted by means of an Andor iKon M camera, Oxford Instruments plc, Abingdon, UK.

3 | RESULTS AND DISCUSSION

3.1 | Performance related differences between CZTSSe MGL devices

The electrical performance parameters derived from j/V -measurements at standard test conditions of low efficiency (2%-6%) MGL samples as already investigated in Ref. [4]

show considerably different values. This is most prominent seen in the short circuit current density, but also variations in open circuit voltages and fill factors are clearly noticeable (Figure 1). Attributed to the high differences in j_{sc} and the semitransparency of the MGLs, initially a difference in the active area as well as optical effects have been suspected as the major cause for the high variability of the parameters of the samples. The semitransparency of the MGLs can be seen in Figure 2, where the transmission of an empty polymer layer before the application of CZTSSe grains as well as an MGL sample is displayed. While the transmission of the polymer is independent of the wavelength and reduced to around 95% by reflection and absorption, the MGL sample shows a transmission of around 13%-14% in the short wavelength range up to the optical bandgap. This optical bandgap is, as extracted by using the tilted dashed line, at around 880 nm (1.41 eV), which corresponds to the peak positions of the PL spectra shown below. The active area of the MGL samples is further reduced by electrically fully or partially inactive grains. By superposition of SEM and LBIC images (Figure 3B) and transmission and LBIC images (Figure 3C)

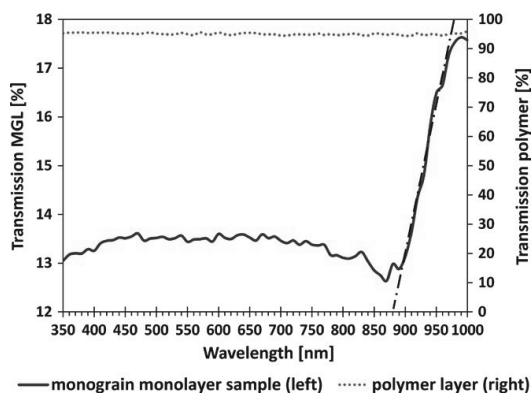


FIGURE 2 Transmission measurements of a monograin layer (MGL) sample and of an empty polymer layer. The tilted dashed vertical line indicates the bandgap

respectively, such inactive CZTSSe areas are identified. Grains without back contact due to insufficient abrasion of the backside of the sample are visible in the transmission image as well as in the SEM image, however, they do not show an LBIC response. An example for such a grain is given in Figure 3 indicated by the solid circle. However, a grain can also be just partially inactive when the corresponding area is covered by electrically insulating but optically transparent polymer, which prevents an electric front contact on this area. This part of a grain is seen in the transmission image, but it is not visible in the LBIC and SEM images. Such an inactive part of a grain is (as an example) indicated by the dashed circle in Figure 3. Such inactive absorber areas explain the difference between the optical transmission and the active area measured by LBIC, however, as it was shown previously,⁴ the electrical active area presented as the AAR does not explain the high difference in electrical performance parameters. Partially lower and inhomogeneous current values from the LBIC evaluation can be seen best in the homogeneity plot (current density distribution) of Figure 4, where sample 1 shows a high number of measurement points at a relatively narrow current range with high current values, while the majority of the measurement points of sample 2a and sample 2b are distributed in a wider current range with lower current values. The full width at half maximum in homogeneity plots for samples 1, 2a, and 2b can be extracted to be 0.46, 0.65, and 0.62 nA which represents a standard deviation of 6%, 20%, and 25% respectively. These homogeneity differences and their origin are investigated in more detail hereafter.

3.2 | Opto-electrical homogeneity investigations

Measurements of the same area of sample 2b by LBIC and EL imaging show that the vast majority of grains show an inverse correlation between the response intensities of these two analyzing methods, where grains with high LBIC response show low EL response and vice versa. In Figure 5 this correlation is seen, with two grains selected and

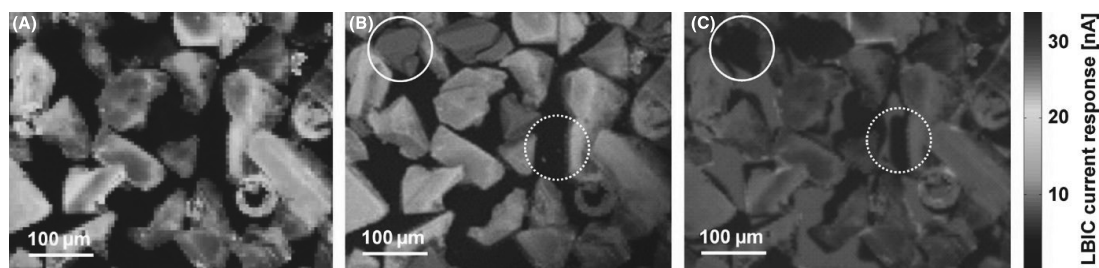


FIGURE 3 Light beam induced current (LBIC) (A), superposition of LBIC and SEM image (B), and LBIC and transmission image (C) of an excerpt of sample 2b. The solid circle indicates an inactive grain without back contact, the dashed circle a part of a grain which is inactive due to missing front contact

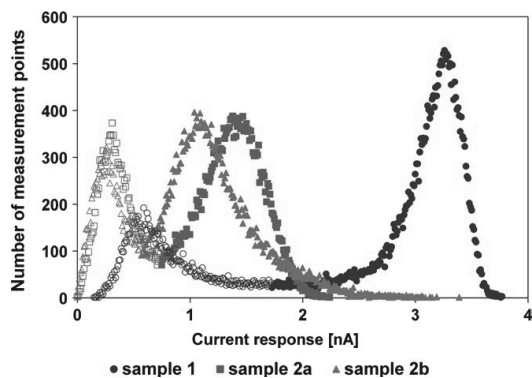


FIGURE 4 Homogeneity plot (current density distribution) of the light beam induced current response of samples 1, 2a, and 2b. The filled markers correspond to measurement points on the active area of the grains, while empty markers correspond to measurement points of the inactive area with the current being generated in the surrounding grains by reflected light

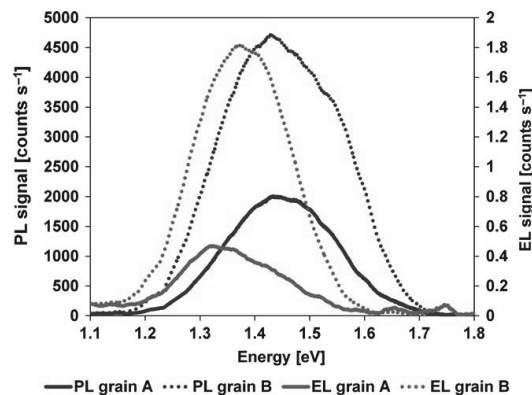


FIGURE 6 Photoluminescence (PL) and electroluminescence (EL) spectra measurements of grains of sample 2b indicated by dashed circles in Figure 5

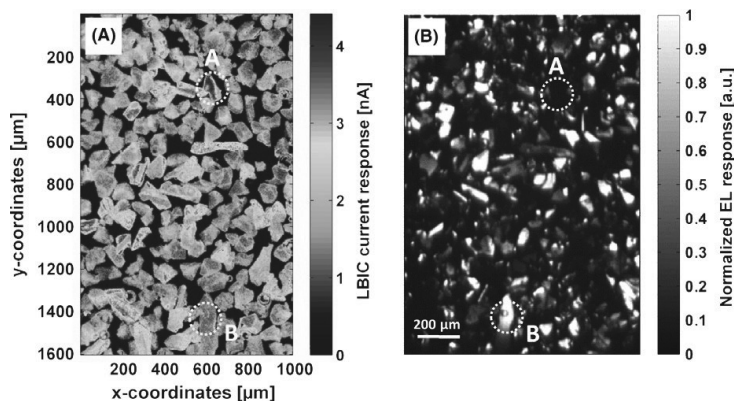


FIGURE 5 Light beam induced current (LBIC) (A) and electroluminescence (EL) (B) image of sample 2b. Photoluminescence and EL spectra of specific grains indicated by dashed circles are seen in Figure 6

indicated by dashed circles as examples. These two grains were furthermore investigated by EL and PL spectra measurements (Figure 6). The rather broad and partially dissymmetrical peaks indicate the presence of different emission energies. Furthermore, the EL spectra show a clear shift of the peaks to lower energies compared to the PL spectra. It was reported already that disordering of CZTS Kesterites can lead to different emission energies and a peak shift of the PL spectrum toward lower energies.^{11,12} However, both investigated grains show similar peak positions of the PL spectra (at higher energies) or of the EL spectra (at lower energies), which does not support a different degree of disordering of the grains. Since the photon flux density during PL spectra measurements was evaluated to be more than four orders of magnitude higher than the average current density during the EL spectra measurements, the different

peak positions of the PL spectra and the EL spectra, respectively, can be attributed to these different intensities. For PL measurements such intensity-dependent peak shifts were already reported before.^{12,13} The peak height of the EL spectra of grains A and B correspond well with the EL response intensity of the EL image as expected, and they also show a similar trend as the peak height of the PL spectra.

Some grains show distinctive patterns in both imaging methods (Figure 7). In Figure 7A a SEM image shows a grain with different oriented planes. These planes can also be identified by EL imaging (Figure 7B) and LBIC imaging (Figure 7C,D). Despite that the EL and LBIC images of the grain show a similar pattern, the response intensity is inversely correlated as it was already observed previously in Figure 5. It has to be noted that the LBIC measurements in

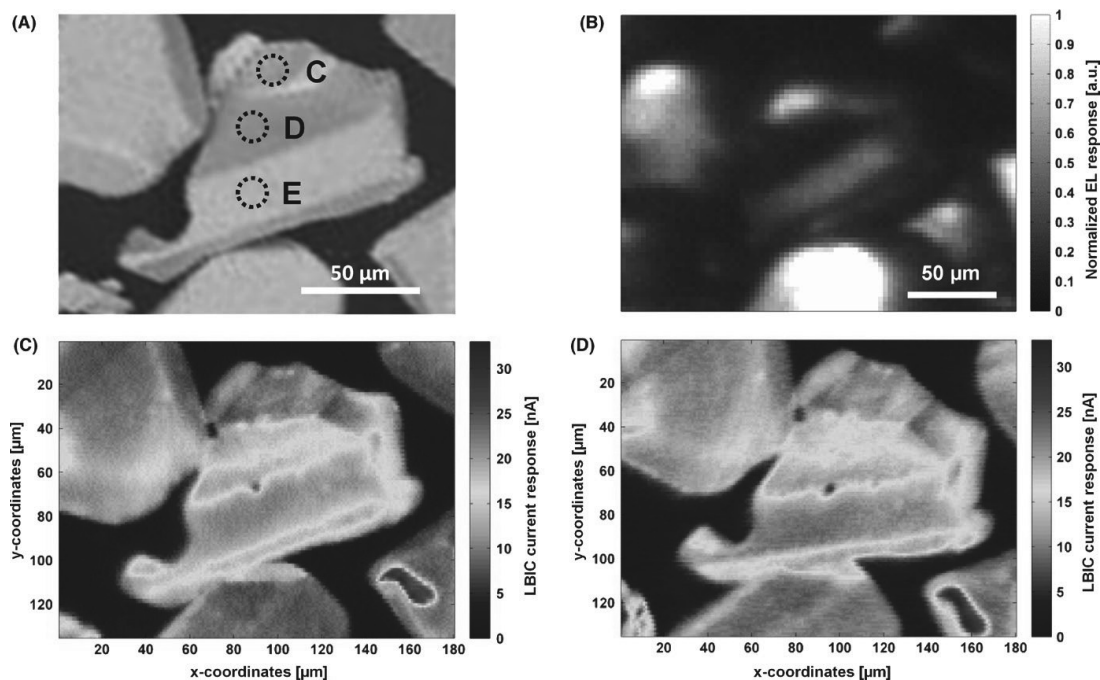


FIGURE 7 SEM (A), electroluminescence (EL) (B) and light beam induced current (LBIC) (C, D) images of one grain of sample 2b. In image (C) the LBIC scanning was conducted with the laser perpendicular to the membrane surface while in (D) the sample surface to the laser was tilted by around 18° . The dashed circles in (A) indicate the measurement spots where EL and photoluminescence spectra measurements were conducted (Figure 8)

Figure 7 were conducted with higher excitation laser intensity than in Figure 5. The different laser intensities can be found in the experimental part. Accordingly the absolute current signals in these figures are different.

Since different light reflection at differently oriented crystal planes was suspected as one reason for spatial current and luminescence variations, the angle of incidence on three planes with different orientations toward the light beam was changed. Tilting the sample during LBIC measurements by around 18° and thus changing the incident angle of the excitation beam (Figure 7D) did not result in a major change of the LBIC results compared to the LBIC image with the laser beam perpendicular to the sample (Figure 7C), which ensures that there is no major influence of the angle of incidence on the measurement results. The measurement response differences are not due to possible occurring reflection differences from the correlated planes.

Electroluminescence and PL spectra measurements (Figure 8) on three different planes of the grain as indicated by the dashed circles in Figure 7A show the same correlation between EL and PL spectra as in Figure 6, where the measurements were conducted on different grains. Thus, we conclude that the mechanism responsible for the differences

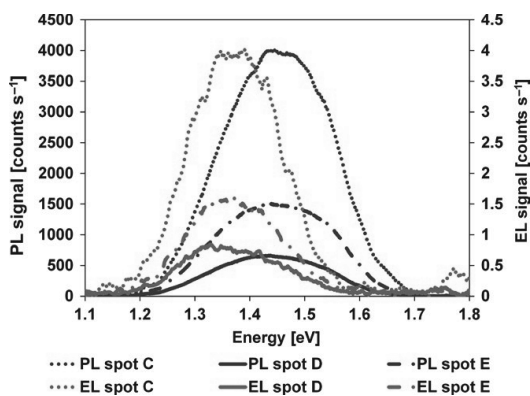


FIGURE 8 Photoluminescence (PL) and electroluminescence (EL) spectra measurements of certain areas on the grain seen in Figure 7 as indicated by the dashed circles in Figure 7A

in LBIC, EL, and PL response is the same, whether it appears on single grains or on different areas of grains.

Locally different resistances, either from the semiconductor material or the electrical contacts on the front and

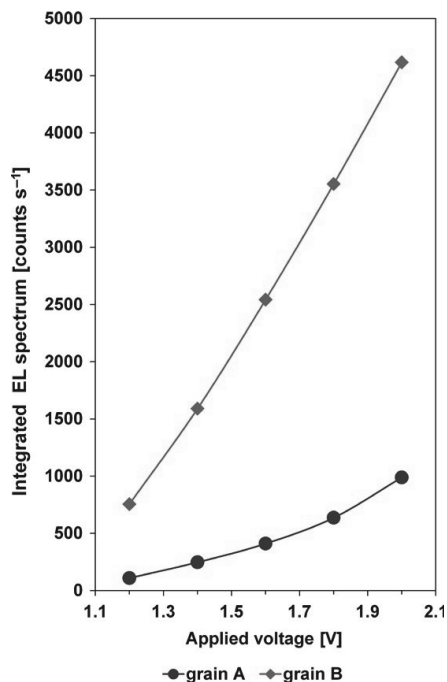


FIGURE 9 Electroluminescence (EL) response of two grains seen in Figure 5 (indicated by dashed circles) for different applied voltages. The EL response was derived by the integration of the EL spectra

backside can lead to a change of LBIC, EL and PL results. A local high resistance would limit the charge carrier extraction, hence a lower LBIC and higher PL response can be expected, which is in accordance with the observed results. However, a higher resistance would also limit the current flow to this area during EL measurements with an according lower EL response. Also local optical variances, eg. due to differences in transmission of the sealing material or the contact materials on the front side of the device, could also lead to a reduction of the excitation and thereby the measured emission intensity, and therefore to a reduction in LBIC, PL, and EL response. However, the images clearly show that the LBIC response is for all grains or crystal planes clearly inversely correlated with the PL and EL response (low LBIC response in all cases correlates with high PL and EL response and vice versa). Therefore, local optical or electrical variances cannot be the main reason for the opposite responses of LBIC and EL or PL signals.

The results that the photocurrent image measured by LBIC corresponds inversely to the image of the EL and PL intensities can easily be understood assuming variations in the barrier height of the p - n -heterojunction. We propose that

grains or areas of grains with high LBIC response but low EL and PL response have a good p - n -heterojunction and thus a high barrier. Here, the charge carriers generated by illumination are separated efficiently and in a wide depletion region leading to a high LBIC response. At the same time the effective charge carrier separation leads to a decreased radiative recombination in PL measurements and thus in a lower PL response. If, on the other hand, grains or areas of grains have a considerably smaller barrier, charge carriers during LBIC and PL measurements are insufficiently separated, which leads to a low carrier extraction during LBIC measurements and thus lower LBIC response and a high radiative recombination at the illuminated area of the PL measurement resulting in a high PL response. However, when conducting EL imaging and spectra measurements, the same voltage is applied to all electrically connected grains. The current flow over the p - n -junction barrier is controlled by the barrier height. A higher current flows over the lower barriers and consequently a higher EL response is seen for low barrier heights and lower current and EL response for higher barrier heights respectively. This mechanism explains the inhomogeneous photocurrent, PL and EL response, with the EL and PL intensities being inversely correlated to the LBIC response intensities. We therefore conclude that this variation in the barrier heights of different samples is the main factor for the differences in the observed current/voltage behavior.

Different overall barrier heights can also be seen when integrating the EL spectra measured for increasing applied voltages on different grains, as analyzed in Figure 9. The EL response for grain A in Figures 5 and 6 (high LBIC, low EL and PL response and therefore relatively high barrier) is increasing only slowly and nonlinear with increasing voltage, while the EL response for grain B in Figures 5 and 6 (low LBIC, high EL and PL response, low barrier) increases much faster and nearly linear with increasing voltage. Whereas the former is controlled by a (small) current across a barrier, while the higher current leading to luminescence at lower barriers is already controlled by an (Ohmic) resistance in the device. This supports the proposed mechanism above.

4 | CONCLUSIONS

Different opto-electrical investigation techniques such as LBIC, optical transmission, SEM, j/V , EL imaging, EL and PL spectra measurements are used to characterize spatial variations in the solar cells made from monograin powder devices. Areas of relative to other areas high photocurrent show relatively low photo- and electro-luminescence. This is especially pronounced for cells with relatively low (here 2%-6%) solar efficiency. A detailed statistical analysis of the images reveals a variation of between $\pm 6\%$ and 25% of the

average current density. Areas with a high LBIC response and a low EL and PL response can be attributed to forming a high junction barrier, while areas with low LBIC response and high EL and PL response are those with a relatively low barrier junction. It is evident that the combination of complimentary investigation methods as it was presented in this paper is crucial for a correct understanding and interpretation of measurement results done on this material. For comparison a “good” CZTSSe solar cell with a cell efficiency of 9.5% and a material (or active-area) efficiency of about 12% shows a current variation of only $\pm 3\%$.

Corresponding investigations should also be performed on thin-film and wafer-based solar cells and allow to extract reliable data for the homogeneity (given in % of the average photocurrent) as well as a deeper understanding of the reason for performance variations.

ACKNOWLEDGMENTS

crystalsol OÜ and University of Tartu cooperate in the IRESOL project (2014-2020.4.02.17-0083) which is funded by European Regional Development Fund. We thank Jaan Aarik, University of Tartu, and his colleagues for supporting research, which will be published in a following paper. We also thank the company Monospektra for borrowing the equipment used for the EL imaging in this study. This work has also been supported by Archimedes/DoRa, by the European Union through the European Regional Development Fund, Project TK141, and by a Mobilitas Pluss Postdoctoral Researcher Grant MOBJD308.

ORCID

Dieter Meissner  <http://orcid.org/0000-0003-4077-3705>

REFERENCES

1. Wang W, Winkler MT, Gunawan O, et al. Device characteristics of CZTSSe thin-film solar cells with 12.6% efficiency. *Adv Energy Mater.* 2014;4:1301465.
2. Meissner D. Photovoltaics based on semiconductor powders. In: Méndez-Vilas A, ed. *Materials and Processes for Energy*. Badajoz: Formatex Research Center; 2013:114-125.
3. Certified measurement by FhG ISE, Freiburg, Germany, Certificate-Nr. 1001076CRY0317, March 24, 2017.
4. Neubauer C, Babatas E, Meissner D. Investigation of rough surfaces on $\text{Cu}_2\text{ZnSn}(\text{S}, \text{Se}_{1-x})_4$ monograin layers using light beam induced current measurements. *Appl Surf Sci.* 2017;423:465-468.
5. Ito K, Nakazawa T. Electrical and optical properties of stannite-type quaternary semiconductor thin films. *Jap J Appl Phys.* 1988;27:2094-2097.
6. Mellikov E, Meissner D, Altosaar M, et al. CZTS monograin powders and thin films. *Adv Mater Res.* 2011;222:8-13.
7. Krustok J, Josepson R, Danilson M, Meissner D. Temperature dependence of $\text{Cu}_2\text{ZnSn}(\text{Se}_x\text{S}_{1-x})_4$ monograin solar cells. *Sol Energy.* 2010;84:379-383.
8. Jackson P, Wuerz R, Hariskos D, Lotter E, Witte W, Powalla M. Effects of heavy alkali elements in $\text{Cu}(\text{In}, \text{Ga})\text{Se}_2$ solar cells with efficiencies up to 22.6%. *Phys Status Solidi RRL.* 2016;10:583-586.
9. Aninat R, Quesada-Rubio LE, Sanchez-Cortez E, Delgado-Sanchez JM. Mapping and comparison of the shortcomings of kesterite absorber layers, and how they could affect industrial scalability. *Thin Solid Films.* 2016;633:146-150.
10. Mellikov E, Altosaar M, Kauk-Kuusik M, et al. Growth of CZTS-based monograins and their application to membrane solar cells. In: Ito K, ed. *Copper Zinc Tin Sulfide-Based Thin-Film Solar Cells*. London: John Wiley & Sons Ltd; 2015:289-309.
11. Timmo K, Kauk-Kuusik M, Pilvet M, et al. Influence of order-disorder in $\text{Cu}_2\text{ZnSnS}_4$ powders on the performance of monograin layer solar cells. *Thin Solid Films.* 2017;633:122-126.
12. Grossberg M, Krustok J, Raudoja J, Raadik T. The role of structural properties on deep defect states in $\text{Cu}_2\text{ZnSnS}_4$ studied by photoluminescence spectroscopy. *Appl Phys Lett.* 2012;101:102102.
13. Grossberg M, Salu P, Raudoja J, Krustok J. Microphotoluminescence study of $\text{Cu}_2\text{ZnSnS}_4$ polycrystals. *J Photon Energy.* 2013;3:030599.

SUPPORTING INFORMATION

Additional supporting information may be found online in the Supporting Information section at the end of the article.

How to cite this article: Neubauer C, Samiepour A, Oueslati S, Ernits K, Meissner D. Spatially resolved opto-electrical performance investigations of $\text{Cu}_2\text{ZnSnS}_{3.2}\text{Se}_{0.8}$ photovoltaic devices. *Energy Sci Eng.* 2018;6:563–569. <https://doi.org/10.1002/ese3.232>

Paper III

Neubauer, C., Samieipour, A., Oueslati, S., Danilson, M., Meissner, D. (2019). Ageing of Kesterite solar cells 1: Degradation processes and their influence on solar cell parameters. *Thin Solid Films*, 669, 595-599.



Ageing of kesterite solar cells 1: Degradation processes and their influence on solar cell parameters

Christian Neubauer^{a,b}, Ali Samieipour^a, Souhaib Oueslati^{a,b}, Mati Danilson^a, Dieter Meissner^{a,b,*}

^a Department of Materials and Environmental Technology, Tallinn University of Technology, Ehitajate tee 5, 19086 Tallinn, Estonia

^b crystalsol OÜ, Akadeemia tee 15a, 12618 Tallinn, Estonia

ARTICLE INFO

Keywords:

Copper zinc tin sulfide
Monograin
Photovoltaics
Degradation
Copper diffusion
Photoluminescence
Recombination
Solar cells

ABSTRACT

For a successful industrial implementation of Kesterites $\text{Cu}_2\text{ZnSn}(\text{S}_x\text{Se}_{1-x})_4$ (CZTSSe) as semiconductor materials for photovoltaics, the long-term stability of the materials and their devices is a key parameter next to efficiency and production costs. Although much research has been conducted on CZTSSe in recent years, the processes leading to degradation are still largely unknown. Hence in this paper we analyze the main degradation processes and their causes as well as how they affect the performance of photovoltaic devices. A temporary CZTSSe-back contact interface barrier and a long-term increase of the front contact resistance and recombination mainly at the cadmium sulfide buffer layer contact of photovoltaic devices is investigated. Copper diffusion in CZTSSe is suggested to be one of the reasons for the change in resistance and recombination and thus for the deterioration of solar cell parameters during degradation or ageing.

1. Introduction

The Kesterites $\text{Cu}_2\text{ZnSn}(\text{S}_x\text{Se}_{1-x})_4$ (CZTSSe) can be used as absorber materials in photovoltaic (PV) applications. They gained attention in recent years as a possible substitute for $\text{Cu}(\text{In,Ga})\text{Se}_2$ (CIGS) due to their use of (in contrast to In and Ga) earth-abundant and non-toxic elements, and advantageous parameters such as a high absorption coefficients, a direct tunable bandgap and low temperature coefficients [1–3]. For thin film PV-devices efficiencies of up to 12.6% have been reported [4], which is however still considerable lower than the best efficiencies achieved with CIGS which is published to be 22.6% [5].

The monograin technology has proven to be able to utilize CZTSSe in a cost efficient and industrial roll-to-roll process [6]. Efficiencies of 9.5% of CZTSSe monograin layer (MGL) devices were certified, corresponding to a material efficiency of around 12% [7]. However, next to efficiency and production costs, the long-term stability of PV products is of great importance for a successful industrial implementation.

Despite intensive literature research, just very few publications on degradation investigations on CZTSSe could be found. Yin et al. [8] proposed a decomposition model of $\text{Cu}_2\text{ZnSnS}_4$ (CZTS) with Cu–Zn separation, however at high temperatures above 600 K. These temperatures used in their experimental setup make a comparison or correlation to a rather low temperature degradation process (378 K in this study) difficult. Accelerated thermal cycling and damp heat tests on

CZTS thin films were conducted by Peng et al. [9] with the focus on the effect of different window layers on the degradation. In there the authors observed an increase in series resistance (R_S) and a reduction of the shunt resistance (R_{SH}) and thus a reduction of the fill factor (FF) for all samples to different degrees, however, for the accelerated thermal cycling process no mechanism or model for these changes is given, while for the damp heat treatment these changes are mainly attributed to the window layers or the molybdenum back contact, respectively. In other publications [10,11] the short circuit current density (j_{SC}) and open circuit voltage (V_{OC}) was modelled during degradation. The poor coverage of degradation of CZTSSe in literature stresses the importance for further investigations on this topic.

Crystalsol routinely investigates its CZTSSe monograin based solar cells under accelerated ageing conditions achieving efficiencies above 90% even for open, non-encapsulated modules after today more than 3000 h at 85 °C in dry conditions. However, the stability critically depends on the exact composition of the absorber material. In this investigation we analyze the degradation of unstable powders with additional investigations reported in a second paper [12]. Further investigations will be published in subsequent papers.

* Corresponding author at: Department of Materials and Environmental Technology, Tallinn University of Technology, Ehitajate tee 5, 19086 Tallinn, Estonia.
E-mail address: dm@crystalsol.com (D. Meissner).

2. Experimental details

2.1. Sample preparation

For the presented degradation analysis four different Kesterite monograin powders were used, two pure sulfides with different degrees of instability during the degradation process, named “CZTS semi-stable” and “CZTS unstable” further in the manuscript and two sulfur-selenides with a S to Se-ratio of 80:20 with as well different instabilities, named therefor “CZTSSe semi-stable” and “CZTSSe unstable”. The Kesterite monocrystals were synthesized from copper, zinc sulfide, tin and sulfur for CZTS and adding zinc selenide for CZTSSe in molten potassium iodine (KI) as flux material. A washing procedure with water dissolves and removes the KI and sieving the resulting powder after drying separates a fraction (56–80 μm) for further powder processing. This was followed by a thermal treatment at 740 °C. By chemical bath deposition employing cadmium acetate and thiourea in an ammonia solution, cadmium sulfide was deposited as a buffer layer on the grains. More detailed information on the production of Kesterite monograin powders can be found elsewhere [13]. By partially embedding the CdS-coated monograins into a transparent epoxy polymer, a monograin layer was formed with approximately half of the surface of the grains left open and uncovered by the polymer, forming a so-called monograin layer (MGL). A transparent conductive oxide (TCO) layer, consisting of intrinsic and aluminum doped zinc oxide was sputtered on these MGLs as a window layer. To enhance the horizontal electrical conductivity of the surface, a thin layer of silver nanowires was applied on top of the TCO, followed by the application of silver paste to form current collectors on the front side. By gluing the membrane onto soda lime glass with transparent epoxy polymer the device was sealed on the front side. An etching step with concentrated sulfuric acid partially removed the polymer on the backside to lay free the monograins, which was followed by a mechanical abrasion to remove the CdS and open the grains. Graphite paste was painted on the back side to establish an Ohmic electrical back contact which finished the PV-device preparation. A surface scanning electron microscopy (SEM) image of a Kesterite MGL and a cross section SEM image of a finished MGL PV-device can be found in [14]. For better characterizing the resistance and the graphite-Kesterite interface, a MGL with grains without CdS was made and the layers of TCO, silver nanowires and silver paste were replaced by graphite paste deposited onto abraded monograins before sealing, thus a graphite-Kesterite-graphite structure was obtained.

2.2. Measurements and investigations techniques

The degradation of the Kesterite devices was carried out here at 105 °C in dry air for different durations. Current density/voltage (j/V) measurements were conducted by means of a Newport Oriel AAA-class sun simulator at room temperature and a Keithley 2400 Source Meter. A Horiba Jobin Yvon Labram HR800 instrument was utilized for PL measurements conducted. As excitation source a green (532 nm) laser was used, where the intensity was adjusted by spectral neutral gray filters. The elemental composition of the Kesterite samples was studied by a Kratos AXIS Ultra DLD X-ray photoelectron spectrometer (XPS) using a monochromatic Al K α X-ray source at 150 W. The detailed XP spectra of core levels were recorded at 20 eV pass energy using the aperture slot of 300 × 700 μm. The relative atomic concentrations were determined from the appropriate core level integrated peak areas and sensitivity factors provided by the Kratos analysis software Vision 2.2.10.

3. Results and discussion

The solar cell parameters of semi-stable and unstable CZTS PV-devices as derived from the j/V measurements conducted with the sun simulator before degradation (0 h) and after 8.5 and 95.5 h degradation

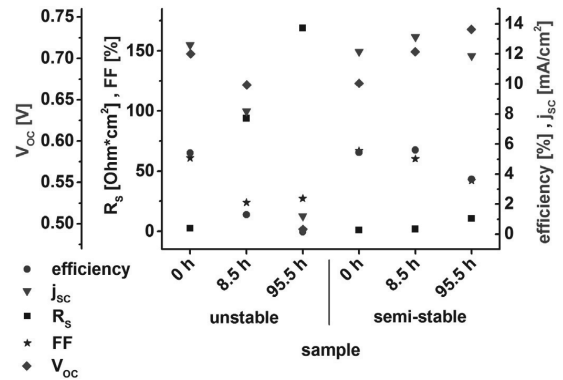


Fig. 1. Solar cell parameters of CZTS samples after different times of degradation.

show the clear difference in stability (Fig. 1). Of special interest is the pronounced increase of R_S for the unstable material. The increase of R_S is also seen for the semi-stable material, however to a much lesser extent. The decrease of V_{OC} for the unstable device also suggests an increased recombination since the change cannot be related to a bandgap decrease as can be seen later in this paper from photoluminescence (PL) measurements. Both effects lead to a reduction of FF and j_{sc} and ultimately the conversion efficiency, and thereby they reflect the big differences in stability of the CZTS devices. Similar observations can be made when comparing the degradation of semi-stable and unstable CZTSSe PV-devices (Fig. 2). However the change in parameters is not so pronounced as for the CZTS devices, especially for the unstable material after 8.5 h of degradation. (See Table 2.)

At least the j/V curves of the unstable CZTS and CZTSSe samples in Fig. 3, indicate the formation of a non-Ohmic barrier at the back contact (opposite to that of the Kesterite-CdS junction), most notable for the unstable CZTS device after 8.5 h of degradation. This effect in combination with the increased R_S led to the postulation of a barrier at the backside between back contact and CZTS. Here for classical Kesterite devices with a molybdenum back contact the formation of molybdenum sulfide at the CZTS-back contact interface and a related phase segregation and a resulting increase of the resistance has been reported during temperature treatment [15,16]. However, the back contact material of the samples investigated in this study is graphite and thus the back contact interface issue described in literature related to

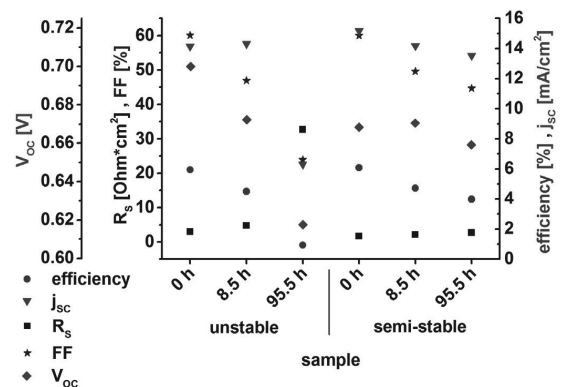


Fig. 2. Solar cell parameters of CZTSSe samples after different times of degradation.

Table 2

XPS measurement results of the copper concentration in atomic percent and the copper to zinc and tin ratio measured at the backside of the samples at different degradation stages, with the efficiency and normalized R_s of the corresponding samples.

Sample	Deg. duration	Efficiency	Cu conc.	Cu/(Zn + Sn)	norm. R_s
	[h]	[%]	[at.%]	[arb. units]	[arb. units]
CZTS unstable	0	5.41	14.6	1.00	1.00
CZTS unstable	8.5	1.31	10.1	0.73	38.9
CZTS unstable	95.5	0.16	9.1	0.58	70.0
CZTS semi-stable	0	5.44	13.1	1.00	1.00
CZTS semi-stable	8.5	5.60	11.0	0.82	2.11
CZTS semi-stable	95.5	3.67	10.3	0.67	12.9
CZTSSe unstable	0	5.94	14.3	1.00	1.00
CZTSSe unstable	8.5	4.51	10.3	0.75	1.62
CZTSSe unstable	95.5	0.93	9.8	0.72	11.2
CZTSSe semi-stable	0	6.08	11.5	1.00	1.00
CZTSSe semi-stable	8.5	4.72	13.0	1.04	1.26
CZTSSe semi-stable	95.5	3.98	12.0	1.00	1.60

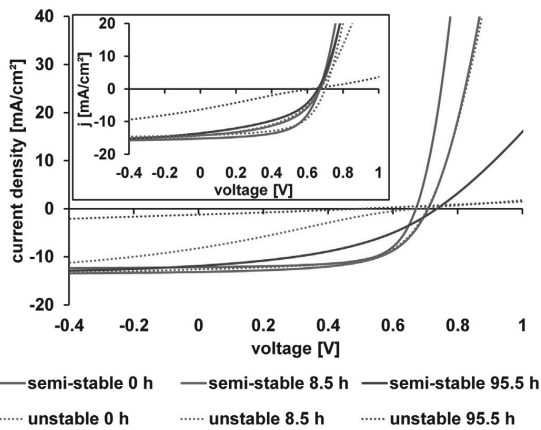


Fig. 3. j/V measurements of CZTS samples after different times of degradation. The inset shows the j/V curves of the CZTSSe samples, with the same legend as for the CZTS samples.

molybdenum cannot occur. Still, also here a non-Ohmic barrier is formed during degradation which increases the resistance.

Such barriers can also be seen in Fig. 4, where the j/V measurements

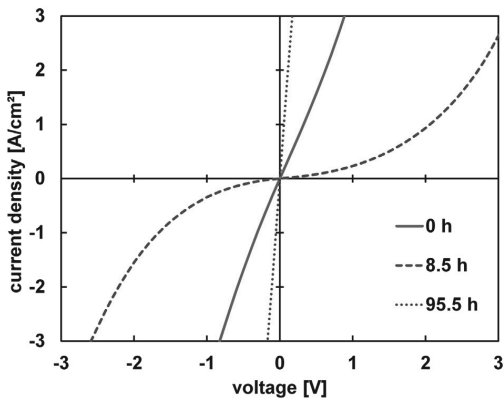


Fig. 4. j/V measurements of the graphite-CZTS-graphite sample, made from unstable CZTS monograins after 0, 8.5 and 95.5 h of degradation.

of the unstable graphite-CZTS-graphite device is shown. While the j/V curve is nearly linear before degradation, it changes to a strongly non-linear curve after 8.5 h of thermal degradation. However, after further degradation (95.5 h), the CZTS material and interfaces gets highly conductive with a linear j/V curve and a resulting resistance much smaller than to that before degradation.

To evaluate this further, resistances of all graphite-Kesterite-graphite samples after various durations of degradation are extracted from the slope of the j/V curves at 0.1 V. These values are plotted against the corresponding degradation time in Fig. 5. As seen there for CZTS, the resistances of the semi-stable and the unstable devices as well those of the unstable CZTSSe rise sharply during the first few hours of degradation, while with further degradation the values decrease again and can reach even lower values than before the degradation. Just the semi-stable CZTSSe device does not show a major change. Since most of the j/V curves are non-linear and thus the resistance is voltage dependent, the linearity value, defined as the ratio of the extracted resistance at 0.9 V to the resistance at 0.1 V, is shown in Fig. 6, with a value of 1 meaning a linear j/V curve and thus an Ohmic resistance. The linearity results can be very well correlated with the resistance values with high resistances being correlated to a low linearity, thus showing that the resistance is mainly the result of a non-Ohmic barrier. Of further interest is that the change of resistance and linearity is connected with the change of the R_s from the PV-devices. However, the high resistance and low linearity of the graphite-Kesterite-graphite samples

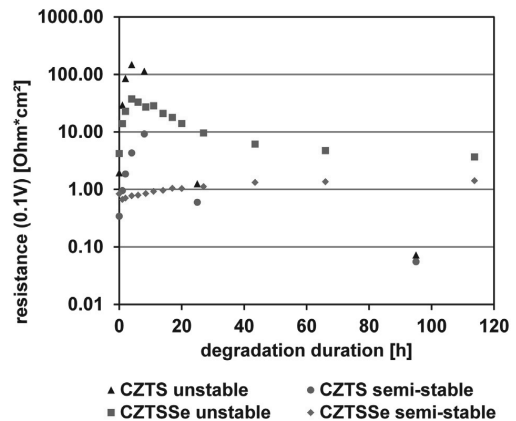


Fig. 5. Resistances of graphite-CZTS-graphite and graphite-CZTSSe-graphite samples derived from the j/V measurements on these samples at 0.1 V, different degradation durations.

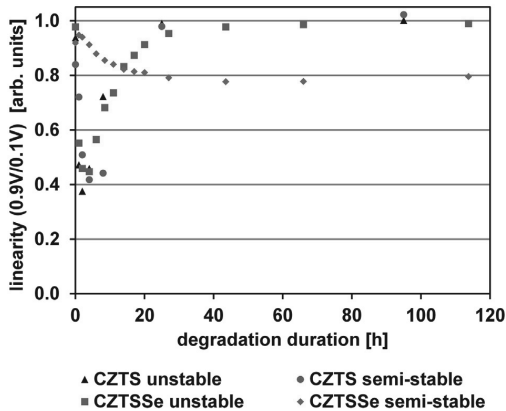


Fig. 6. Linearity values of graphite-CZTS-graphite and graphite-CZTSSe-graphite samples, derived from the ratio of the resistance at 0.9 V and 0.1 V (see also text).

changes fast and is just temporary while the increase of R_s of the PV-devices is slowly and long-term.

It is well known from literature, that copper doping of CdS leads to high dark resistivity and photoconductivity of CdS [17,18], hence copper diffusion from the absorber material into CdS is the most likely cause for the observed increased resistance during degradation. Additionally it was also reported in [19], that copper in CdS causes recombination centers and thus leads to increased recombination near the p-n-junction and to a reduction of the FF. Despite that the mentioned observations were made for devices with cadmium telluride as absorber, a similarity to Kesterite-CdS devices can be assumed.

To investigate the behavior of copper in Kesterites during degradation, the elemental composition of the Kesterite samples was investigated by XPS before (0 h) and after (8.5 h, 95.5 h) degradation on the back side of the devices without a back contact. Table 1 compares the copper concentration and the copper to zinc plus tin ratio with the observed efficiency and the normalized series resistance R_s of the samples. The hereby measured elemental concentration differs considerably from stoichiometric composition, especially showing a low copper concentration. Such off-stoichiometric composition of the surface of Kesterite materials and the high difference to the bulk composition was already measured and reported for CZTSSe monograins [20] as well as for pure selenium-based Kesterite thin films [21]. Nevertheless a comparison of different samples gives valuable insight in relative differences in composition. For the unstable devices clearly a higher copper depletion can be found than in the semi-stable devices. The increase of R_s during the different degradation steps can be well correlated with the copper depletion and the copper to zinc plus tin ratio. While the XPS measurements and the measured copper diffusion were conducted on the back side, it can be assumed that due to the seen mobility of copper the diffusion is also present at the front side which leads to the proposed copper doping of CdS. In a publication by Tajima et al. [22] the elemental distribution at a CZTS-CdS-interface was evaluated by three dimensional atom-probe tomography, and although the authors do not discuss the copper diffusion exactly this can clearly be seen in the provided figure. In another publication by Yang et al. [23], copper diffusion in the absorber layer and into the CdS buffer layer of cadmium telluride samples is presented and discussed. This clearly supports the role of the copper diffusion as a major cause of the performance reduction during degradation.

Analyzing the PV-devices by photoluminescence as seen in Fig. 7 for the CZTS and Fig. 8 for the CZTSSe samples, a change of the PL response of the CZTS samples to higher luminescence, a broadening of the peak

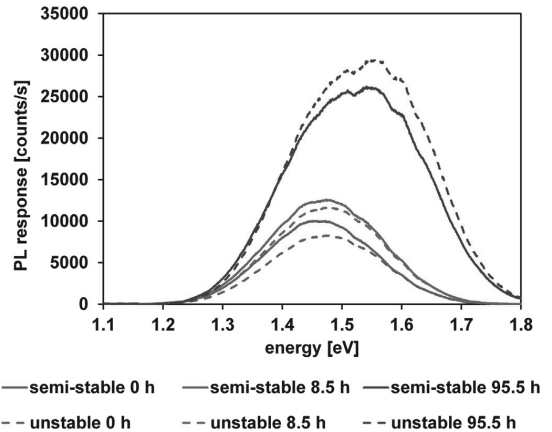


Fig. 7. PL response of the semi-stable and unstable CZTS PV-devices without and after 8.5 and 95.5 h of degradation.

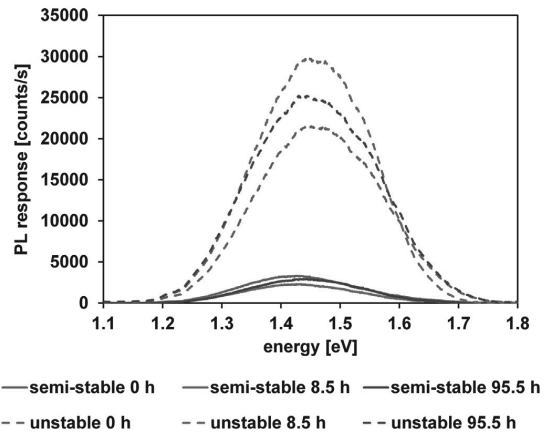


Fig. 8. PL response of the semi-stable and unstable CZTSSe PV-devices without and after 8.5 and 95.5 h of degradation.

and a peak shift towards higher energies with increased degradation becomes visible. The PL peak of samples degraded for 95.5 h is around 100 meV shifted towards higher energies compared to that of the fresh samples. A part of this shift can be explained by the increased series resistance R_s of the PV-device and thus the reduction of the carrier extraction as described before [7]. However, PL measurements of the same samples with a lower excitation light intensity show a difference in the peak position of just around 20 meV. Hence the major reason for the peak shift is attributed to an ordering-disordering effect, with more ordered CZTS after degradation. This is in accordance with previous investigations [24], where a temperature treatment of CZTS monograins at 150 °C for four hours led to a very similar peak shift. In contrast, the PL responses of the CZTSSe devices do show just a minor change with degradation, thus it can be concluded that the degradation here does not lead to a significant ordering.

4. Conclusions

CZTS and CZTSSe MGL devices with different stabilities were investigated with respect to the occurring degradation processes. Two different process paths were identified, a fast but temporary non-Ohmic

barrier at the backside at the back contact, and a slow but long-term front side degradation. Both processes are suggested to be caused by copper diffusion processes, which lead to a barrier at the backside as well as copper doping of CdS at the front side. The latter leads to a high dark resistance which hinders the carrier extraction and in combination with the formation of recombination centers increases the loss of photocurrent in the CdS close to the p-n junction. Due to these effects the solar cell performance parameters deteriorate according to the relative stability of the materials. The degradation homogeneity and increased recombination close to the p-n-junction in the CdS was further investigated by other opto-electrical methods which will be presented and discussed in a following publication.

Acknowledgements

We thank the Austrian crystalsol team, especially Paula Santos Ortiz for performing accelerated ageing tests. This work has been supported by Archimedes/DoRa, by the European Union through the European Regional Development Fund, Project TK141, and by a Mobilias Plus Postdoctoral Researcher Grant MOBJD308.

References

- [1] K. Ito, T. Nakazawa, Electrical and optical properties of stannite-type quaternary semiconductor thin films, *Jap J Appl Phys* 27 (1988) 2094–2097.
- [2] E. Mellikov, D. Meissner, M. Altsaar, M. Kauk, J. Krustok, A. Öpik, O. Volobujeva, J. Iljina, K. Timmo, I. Klavina, J. Raudoja, M. Grossberg, T. Varema, K. Muska, M. Ganchev, S. Bereznev, M. Danilson, CZTS Monograin Powders and Thin Films, *Adv. Mater. Res.* 222 (2011) 8–13.
- [3] J. Krustok, R. Josepson, M. Danilson, D. Meissner, Temperature dependence of $\text{Cu}_2\text{ZnSn}(\text{Se}_x\text{S}_{1-x})_4$ monograin solar cells, *Sol. Energy* 84 (2010) 379–383.
- [4] W. Wang, M.T. Winkler, O. Gunawan, T. Gokmen, T.K. Todorov, Y. Zhu, D.B. Mitzi, Device characteristics of CZTSSe thin-film solar cells with 12.6% efficiency, *Adv. Energy Mater.* 4 (2014) 1301465.
- [5] P. Jackson, R. Wuerz, D. Hariskos, E. Lotter, W. Witte, M. Powalla, Effects of heavy alkali elements in $\text{Cu}(\text{In,Ga})\text{Se}_2$ solar cells with efficiencies up to 22.6%, *Phys. Status Solidi RRL* 10 (2016) 583–586.
- [6] D. Meissner, Photovoltaics based on Semiconductor Powders, in: A. Méndez-Vilas (Ed.), *Materials and Processes for Energy*, Formatex Research Center, Badajoz, 2013, pp. 114–125.
- [7] C. Neubauer, A. Samiepour, S. Oueslati, K. Ernits, D. Meissner, Spatially resolved opto-electrical performance investigations of $\text{Cu}_2\text{ZnSnS}_{3.2}\text{Se}_{0.8}$ photovoltaic devices, *Energy Sci Eng.* 6 (2018) 563–569.
- [8] X. Yin, H. Gong, Heat-field-stimulated decomposition reaction in $\text{Cu}_2\text{ZnSnS}_4$, *Acta Mater.* 60 (2012) 6732–6741.
- [9] C.-Y. Peng, T.P. Dhakae, A. Emrani, S. Lu, C.R. Westgate, Stability of CZTS thin film solar cells upon accelerated thermal cycling and damp heat exposure, *Photovoltaic Specialist Conference (PVSC) IEEE 40nd*, 2014 (Colorado, USA).
- [10] P. Darvishzadeh, G. Redzwan, R. Ahmadi, N.E. Gorji, Modeling the degradation/recovery of short-circuit current density in perovskite and thin film photovoltaics, *Org. Electron.* 43 (2017) 247–252.
- [11] P. Darvishzadeh, M. Babanezhad, R. Ahmadi, N.E. Gorji, Modeling the degradation/recovery of open-circuit voltage in perovskite and thin film solar cells, *Mater. Des.* 114 (2017) 339–344.
- [12] S. Oueslati, D. Ageing of Kesterite Solar Cells 2: Impact on Photocurrent Generation, *Thin Solid Films* (vvv (2019) nnnn-nnnn, submitted).
- [13] E. Mellikov, M. Altsaar, M. Kauk-Kuusik, K. Timmo, D. Meissner, M. Grossberg, J. Krustok, O. Volobujeva, Growth of CZTS-Based Monograin and their Application to Membrane Solar Cells, in: K. Ito (Ed.), *Copper Zinc Tin Sulfide-Based Thin-Film Solar Cells*, John Wiley & Sons Ltd, London, 2015, pp. 289–309.
- [14] C. Neubauer, E. Babatas, D. Meissner, Investigation of rough surfaces on $\text{Cu}_2\text{ZnSn}(\text{S}_x\text{Se}_{1-x})_4$ monograin layers using light beam induced current measurements, *Appl. Surf. Sci.* 423 (2017) 465–468.
- [15] J.J. Scragg, J.T. Wätjen, M. Edoff, T. Ericson, T. Kubart, C. Platzer-Björkman, A Detrimental Reaction at the Molybdenum Back contact in $\text{Cu}_2\text{ZnSn}(\text{S},\text{Se})_4$ Thin-Film Solar Cells, *J. Am. Chem. Soc.* 134 (2012) 19330–19333.
- [16] K.-J. Yang, J.-H. Sim, D.-H. Son, D.-H. Kim, G.Y. Kim, W. Jo, S. Song, J. Kim, D. Nam, H. Cheong, J.-K. Kang, Effects of the compositional ratio distribution with sulfurization temperatures in the absorber layer on the defect and surface electrical characteristics of $\text{Cu}_2\text{ZnSnS}_4$ solar cells, *Prog. Photovolt. Res. Appl.* 23 (2015) 1771–1784.
- [17] R. Panda, V. Rathore, M. Rathore, V. Shelke, N. Badera, L.S.S. Chandra, D. Jain, M. Gangrade, T. Shripati, V. Ganesan, Carrier recombination in Cu doped CdS thin films: Photocurrent and optical studies, *Appl. Surf. Sci.* 258 (2012) 5086–5093.
- [18] D. Petre, I. Pintilie, E. Pentia, I. Pintilie, T. Botila, The influence of Cu doping on opto-electronic properties of chemically deposited CdS, *Mater. Sci. Eng. B* 58 (1999) 238–243.
- [19] Y. Deng, J. Yang, R. Yang, K. Shen, D. Wang, D. Wang, Cu-doped CdS and its application in CdTe thin film solar cell, *AIP Adv.* 6 (2016) 015203.
- [20] M. Danilson, M. Altsaar, M. Kauk, A. Katerski, J. Krustok, J. Raudoja, XPS study of CZTSSe monograin powders, *Thin Solid Films* 519 (2011) 7407–7411.
- [21] M.V. Yakushev, M.A. Sulimov, E. Skidchenko, J. Márquez-Prieto, I. Forbes, P.R. Edwards, M.V. Kuznetsov, V.D. Zhivulko, O.M. Borodavchenko, A.V. Mudryi, J. Krustok, R.W. Martin, Effects of Ar^+ etching of $\text{Cu}_2\text{ZnSnSe}_4$ thin films: an x-ray photoelectron spectroscopy and photoluminescence study, *J. Vac. Sci. Technol. B* 36 (2018) 061208.
- [22] S. Tajima, M. Umehara, M. Hasegawa, T. Mise, T. Itoh, $\text{Cu}_2\text{ZnSnS}_4$ photovoltaic cell with improved efficiency fabricated by high-temperature annealing after CdS buffer-layer deposition, *Prog. Photovolt. Res. Appl.* 25 (2017) 14–22.
- [23] R. Yang, D. Wang, M. Jeng, K. Ho, D. Wang, Stable CdTe thin film solar cells with a MoO_x backcontact buffer layer, *Prog. Photovolt. Res. Appl.* 24 (2016) 59–65.
- [24] K. Timmo, M. Kauk-Kuusik, M. Pilvet, T. Raadik, M. Altsaar, M. Danilson, M. Grossberg, J. Raudoja, K. Ernits, Influence of order-disorder in $\text{Cu}_2\text{ZnSnS}_4$ powders on the performance of monograin layer solar cells, *Thin Solid Films* 633 (2017) 122–126.

Paper IV

Samiepour, A., **Neubauer, C.**, Oueslati, S., Mikli, V., Meissner, D. (2019). Ageing of Kesterite solar cells 2: Impact on photocurrent generation. *Thin Solid Films*, 669, 509-513.



Ageing of kesterite solar cells 2: Impact on photocurrent generation

Ali Samiepour^a, Christian Neubauer^{a,b}, Souhaib Oueslati^{a,b}, Valdek Mikli^a, Dieter Meissner^{a,b,*}

^a Department of Materials and Environmental Technology, Tallinn University of Technology, Ehitajate tee 5, 19086 Tallinn, Estonia

^b crystalsol OÜ, Akadeemia tee 15a, 12618 Tallinn, Estonia



ARTICLE INFO

Keywords:

Copper zinc tin sulfide
Monograin
Photovoltaics
Degradation
Electron beam induced current
Light beam induced current
External quantum efficiency
Copper diffusion

ABSTRACT

As yet results of ageing experiments of Kesterite solar cells have not been published. However, at least in crystalsol detailed investigations of monograin-based solar cells have been performed proving very different stabilities depending on the exact composition of the Kesterites. Completely stable solar cells even without any sealing have been demonstrated internally. However in this paper we report on ageing effects observed for internally called “highly unstable” $\text{Cu}_2\text{ZnSnS}_4$ (CZTS) solar cells aged for 8.5 and 95.5 h at 105 °C in air, already also reported in part 1 of these investigations. During these times the initial efficiency of 5.4% decreased by 76% and another 88%, respectively. The photocurrent generation was investigated in detail by light beam induced current (LBIC) measurements of the front side and electron beam induced current (EBIC) measurements of cross sections of the CZTS/CdS/ZnO active junctions. Besides a pronounced decrease of the LBIC and the EBIC signal also a shift of the EBIC signal much further into the Kesterite material was observed, which can be explained by the in part 1 already found diffusion of copper from the surface of CZTS into the CdS buffer layer acting finally as a strong charge carrier recombination center. Thereby the EBIC signal first observed mainly close to the interface has vanished, only a small EBIC signal in a depth of around 400 nm still remains visible, a depth, from which only minority carriers can still reach this main recombination center in the interface.

1. Introduction

Although Kesterite materials are considered as the most promising earth abundant thin film materials especially for solar cell production, nearly no investigations of their stability and the lifetime of solar cell made from these materials as absorber materials can be found in the literature. In a first paper on the ageing of Kesterites, here solar cell devices made from single-crystalline, monograins $\text{Cu}_2\text{ZnSn}(\text{S}_x\text{Se}_{1-x})_4$ (CZTSSe) absorber layers, we summarized the investigations of differently stable devices [1]. In that paper we report results obtained for solar cells as well as for devices with two Ohmic contacts to graphite. These results attribute the long time (8.5 and 95.5 h) accelerated (at 105 °C) deterioration of the solar cell efficiency of semi- and unstable Kesterites to the diffusion of copper in not perfectly stoichiometric Kesterites.

In this second part of our investigations we report on more detailed microscopic investigations of the least stable pure sulfide compounds (CZTS) also already characterized in part 1. Scanning beam microscopy of solar cells after different times of ageing is reported, determined in a laser scan photocurrent setup from the outside as well as using a scanning electron microscope (SEM) for cross sections. They are completed by external quantum efficiency (EQE) spectra measurements.

Whereas no photocurrent images were found in the literature, a few papers on electron beam induced current (EBIC) investigations of solar cell cross sections, obtained by vertically embedding solar cells into a polymer glue, cutting and polishing, have been published. The EBIC signals of our samples exhibit usually a quite continuous EBIC signal at the CZTS/CdS interface inside the absorber material (compare Fig. 3), while a spotty appearance of the EBIC signal was reported by Sugimoto et al. [2] and Fukano et al. [3]. Here void formation either during the formation of the thin-film devices investigated in their papers or during cross-section preparation may be the reason.

As reported in [4], surface passivation by using atomic layer deposition of Al_2O_3 coating of the cross section surface of samples can lead to a stronger EBIC signal, here demonstrated for $\text{Cu}(\text{In,Ga})\text{S}_2$ devices. However, this critically depends on the acceleration voltage dependent penetration depth of the electron beam. In our case corresponding investigation employing Al_2O_3 films prepared by laser ablation on one of our samples did not result in a significant improvement of the EBIC signal.

2. Experimental

Copper-zinc-tin-chalcogenides, especially $\text{Cu}_2\text{ZnSnS}_4$, $\text{Cu}_2\text{ZnSnSe}_4$

* Corresponding author at: Department of Materials and Environmental Technology, Tallinn University of Technology, Ehitajate tee 5, 19086 Tallinn, Estonia.
E-mail address: dm@crystalsol.com (D. Meissner).

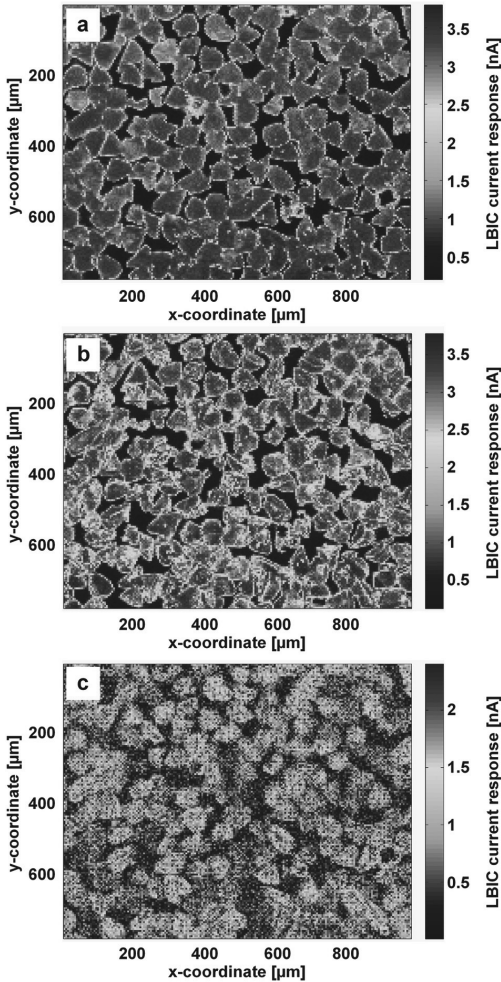


Fig. 1. LBIC results of unstable fresh (0 h, a), medium aged (8.5 h, b) and most aged (95.5 h, c) CZTS photovoltaic devices.

and their solid solutions $Cu_2ZnSn(S,Se)_4$, called Kesterites due to their crystal structure, are produced in crystalsol OÜ, Tallinn, Estonia [5]. The powder particles are single crystalline, mainly tetrahedron-shaped and grown in a molten salt flux [6]. Here, 63–80 μm semiconductor grains are arranged in a single layer membrane, called monograin layer (MGL). To complete a solar cell device on the front side, different layers are added to the absorber layer (here a not completely stoichiometric pure sulfide compound CZTS) including CdS as a buffer layer by chemical bath deposition, intrinsic and aluminum doped zinc oxide (ZnO) sputtered as a window layer, and a very thin layer of silver nanowires (from Cambrios, Sunnyvale, CA, USA) for enhancing the surface cross-conductivity. The front side is then glued to a soda lime glass window. By etching the backside with sulfuric acid, polishing the CZTS grains and painting a water based graphite-suspension to it, an Ohmic contact is formed and the solar cell is completed (compare [1,7]).

Stability tests of solar cells made from the powders are performed in an oven in air at 105 °C as reported already in [1]. Depending on the quality of the absorber material, the short circuit current decreases after 8.5 and 95.5 h ageing in an oven. Three samples of MGL-devices with

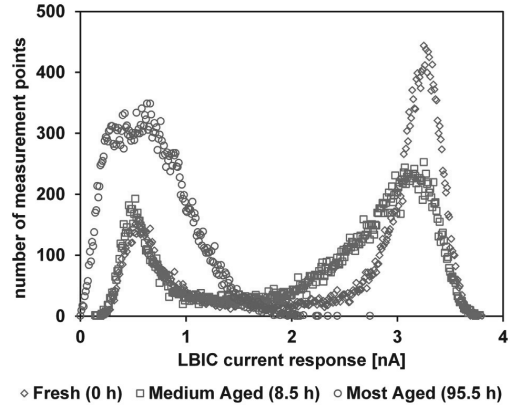


Fig. 2. Homogeneity plot of the differently degraded unstable CZTS samples.

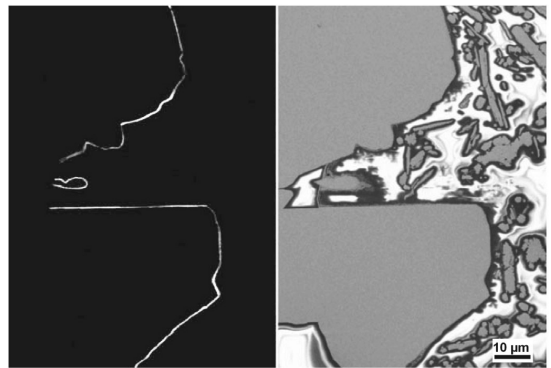


Fig. 3. EBIC signal of two different CZTS grains (left) and the SEM picture of those (right).

quite unstable CZTS monograins were investigated for this paper, a fresh (non-aged), a medium aged or a long time aged, respectively. Fresh has no degradation, medium aged was kept for 8.5 h and the long time aged for 95.5 h in the oven in air at 105 °C. Light beam induced current (LBIC) and EQE measurements of one and the same sample was measured, however at different degradation stages. For the EBIC analysis separate samples were prepared, with identical CZTS monograin powder and production process but degraded for different durations.

For cross section preparation, EpoThin 2™, Bühler, Lake Bluff, Illinois, USA, a two component polymer epoxy resin and hardener is used for mounting the monograin membranes in a cylindrical shaped device. The polymer is cured at 45 °C for 4 h and over night at room temperature. Every sample is polished using a Bühler Ecomet 250 polishing apparatus. Different sand papers are used for polishing. It is very important to avoid cracks in the grains or at the interfaces. Electron microscopy and EBIC measurements are performed using an ULTRA 55 SEM, Carl Zeiss Microscopy GmbH, Jena, Germany. EBIC images are shown as split picture of secondary electron and photo-current images obtained simultaneously, showing on one side the SEM and on the other side the EBIC image. The closest distance of the surface and the detector is set to have the best resolution of the pictures; usually 4 mm. The applied voltage to the sample should be as small as possible to avoid charging on the surface and to get a better resolution for understanding the interface borders.

Electrical characterization is performed using a calibrated AAA-

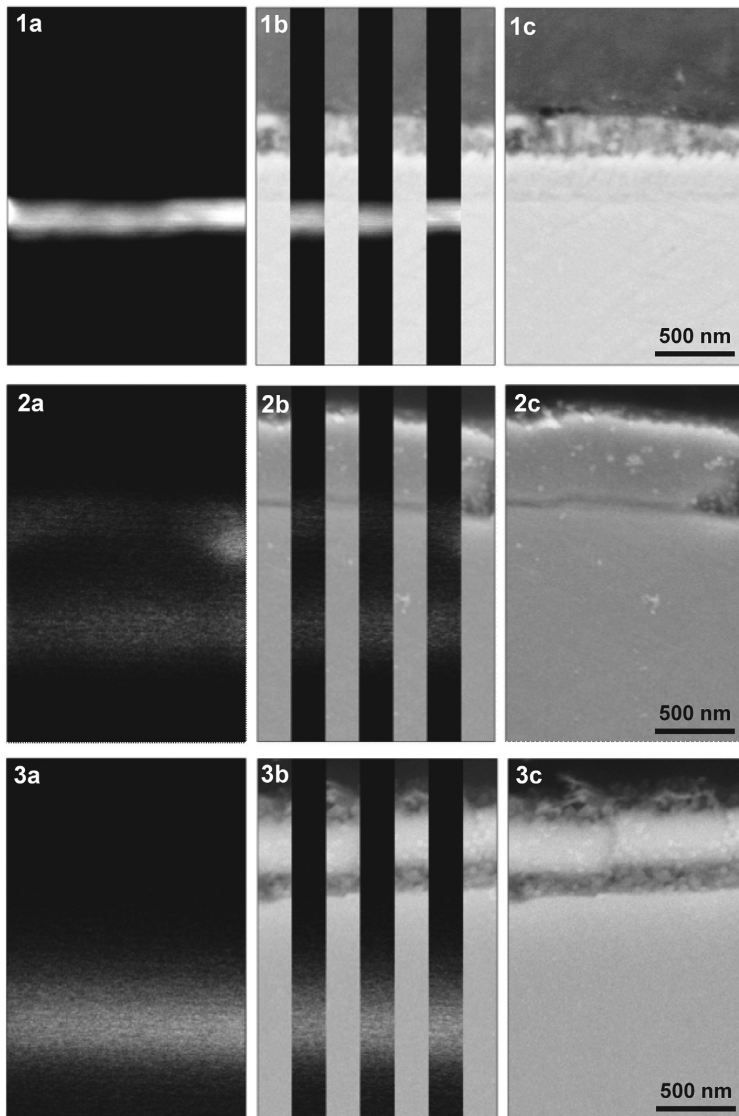


Fig. 4. EBIC (a), superimposed EBIC on SEM (b) and SEM (c) pictures of fresh (1), 8.5 h degradation (2) and 95.5 h degradation (3) CZTS solar cell.

class sun simulator as described in [1]. LBIC measurements were conducted using a red laser, a spectral neutral grey filter (to achieve an intensity of around 0.5 suns), current sensitivity 20 nA and using a time constant of 3 ms in the lock in amplifier.

The EQE measurements were conducted by a Newport Oriel system (300 W Xenon lamp, Cornerstone 260 Monochromator, silicon detector and Merlin radiometer system).

3. Results

3.1. Photocurrent imaging

Fig. 1 shows LBIC images of the investigated CZTS photovoltaic (PV) samples at different times of degradation, fresh (0 h, Fig. 1a), medium

aged (8.5 h, Fig. 1b) and most aged (95.5 h, Fig. 1c). Visually it can be observed that the LBIC response measured on the sample before degradation shows a high and homogenous current distribution. After 8.5 h of degradation some areas still have a high current response while other areas show a reduction of the signal, leading to an inhomogeneous LBIC current distribution. After 95.5 h of degradation the current response is very weak for all grains and areas.

Since the LBIC measurements were performed on the same device and nearly identical areas are measured for all the degradation steps, it is possible to directly compare the photocurrents grain by grain during degradation. For the medium aged results (8.5 h) it can be observed that while the majority of the grains show an inhomogeneous reduction of the photocurrent, some grains maintain a homogenous current response. Very few grains show even a higher photocurrent compared to

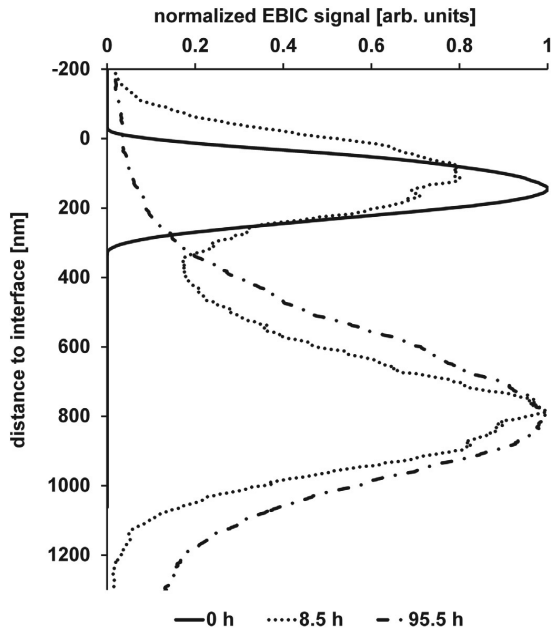


Fig. 5. Normalized EBIC signal of CZTS of fresh (solid), 8.5 h degradation (dotted) and 95.5 h degradation (solid-dash).

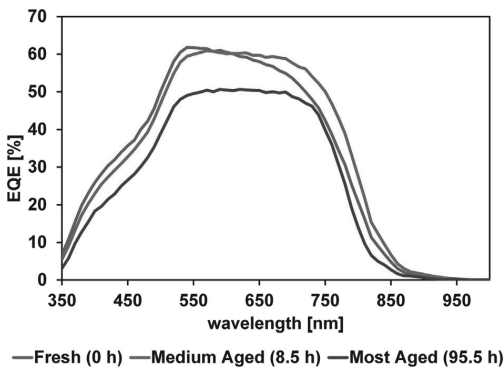


Fig. 6. EQE measurements of the unstable CZTS PV device, fresh and degraded for 8.5 and 95.5 h.

the photocurrent before degradation. However, at further degradation (95.5 h) all grains, even the ones which had an improved current response after 8.5 h, are strongly degraded and the current response is very weak. The homogeneity plots of the measured data are given in Fig. 2. In there, 2 distinctive peaks are visible for each sample. While the peaks at higher current values correspond to measurement points of active CZTS material, the second (smaller) peaks at smaller current values correspond to measurement points of the inactive area, either because no absorber material is present or the CZTS absorber is inactive due to missing front and/or back contact. Additional information on how such LBIC measurement data can be analyzed can be found in [8]. After 8.5 h degradation the maximum current value is nearly the same as in the fresh sample. However, the current response gets more inhomogeneous, which in the homogeneity plot is seen as a widening of the peak. For the most, 95 h, degraded cell the current response is very

weak and it is hard to exactly distinguish between active (above 0.7 nA) and the inactive area caused by light reflection from the polymer between the grains onto surrounding grains (below 0.7 nA).

3.2. EBIC investigations

A combined EBIC and SEM picture of a fresh sample in 2000 x magnification is shown in Fig. 3. On the right side of the SEM picture small metal parts are seen which are embedded into the polymer during the mounting to avoid charging in this part of the sample. They are useful to have a better resolution even for high magnification (e.g. by 100,000×). An EBIC signal is formed at the junction of CZTS as an absorber (p-type) and CdS as a n-type semiconductor. Good interfaces between the different layers; i.e. CZTS, CdS, intrinsic ZnO, Al doped ZnO, silver nanowires are necessary to have a well visible EBIC signal. A good interface also helps to have a strong EBIC signal. If one of the layers is damaged during the polishing, then a weaker or no EBIC can be seen.

Degradation of a CZTS solar cell changes the EBIC signal. For the same magnification of unstable CZTS grains the EBIC signal (a), superimposed (b) onto the SEM picture, and the SEM picture (c) are shown in Fig. 4 for the fresh sample (1), a sample after 8.5 h of degradation (2) and after 95.5 h (3). It has to be noted that since the absolute signal is weakening during degradation, the current amplification had to be increased with increasing degradation. The EBIC measurement of the fresh sample (Fig. 4 1a–1c) forms a strong clear signal close to the interface. When the sample is aged, this signal close to the interface gets weaker while additionally a signal more in the bulk further away from the interface is formed. The minimum in between can be attributed to the distance at which the Fermi level is located in the middle between the band edges (or energy levels involved in recombination) occurring, leading to a maximum of loss. After 95.5 h of degradation the first signal close to the CdS interface vanishes, while the signal deeper in the bulk remains.

The change of the signal close to the CZTS–CdS interface is best seen when comparing EBIC profiles extracted from the measured images of the differently degraded samples in Fig. 5. In order to extract these signal profiles along a line through the image, the EBIC pictures are converted to $Int = f(x,y)$ matrices. For this the images are loaded into the program OriginLab and exported from there as an ASCII-file, from which the data then were further processed in Excel. Typical EBIC profiles of the fresh (solid line), the sample degraded for 8.5 h (dotted) and for 95.5 h (dash/point) are depicted in Fig. 5. In order to minimize noise an average of 73 lines (lines 74–146 of the 511 vertical lines the images consist of) is used. The position is the same for all images. From these EBIC profiles the change of the signal peaks is clearly noticeable, and the peak position from the interface as well as the distance between the two peaks formed at different degradation stages can be extracted. While the peak of the signal close to the CdS is formed around 200 nm from the interface, the second peak more in the bulk is around 800 nm away from the interface, thus also the distance between the two peaks is around 600 nm. However, the peak maxima in Fig. 5 are normalized, since the signal height decreases dramatically upon ageing.

3.3. EQE investigations

In Fig. 6 the EQE-spectra of the unstable solar cells made from pure sulfide powder at different degradation stages (fresh, medium aged, most aged) are presented. It is noticeable that the response in the short wavelength range is decreasing with increasing degradation and the response in the long wavelength range is increasing after 8.5 h of degradation, hence the curve gets more rectangular. With further degradation the signal is decreasing over the whole spectrum, as could be expected from the overall decrease of the short circuit current density (J_{sc}) measured by the sun simulator (see solar cell parameters in [1]). However, the quantum efficiency at the short wavelength region seems

also here to decrease more than at the long wavelength region. It has to be mentioned here that the EQE response decreases less than the J_{SC} measured by the sun simulator. This difference can be explained by a difference in illumination intensity, where the light intensity of the EQE measurement setup is smaller approximately by a factor of 1000 compared to the light intensity of the sun simulator. Another observation is that the bandgap of the most aged sample seems to increase, which is in accordance of the shift of the PL response reported in [1] and the ordering of the Kesterite as described there.

4. Discussion

As described in part 1 [1] of this analysis, ageing of Kesterites is connected with Cu diffusion into CdS. The observed change in homogeneities of the photocurrent measured by LBIC during degradation suggests that the degradation mechanism and the related copper diffusion, which was identified as happening at locally different speeds, occurs in some grains or areas of grains faster than in others. The copper states in CdS are strong recombination centers, as known since a long time and even used in Philips CdS monograin photocurrent detectors [5,9], the parent devices of crystalsol's solar cells. These were all copper doped CdS, so copper doping of CdS introduces strong recombination centers. Thereby the lifetime of photo generated charge carriers in CdS becomes very small and the material becomes highly photoconductive. In the dark there is no conductivity if all sulfur vacancy-based electrons in the conduction band are trapped in these recombination centers, energy states deep within the band gap. Now upon illumination in our devices, electron-hole pairs are generated and in EBIC electron/hole-pairs are produced close to the interface or further away from the interface. For the investigated solar cell there is a certain width of space charge region, which if it measured sensitive enough goes quite far into CZTS, up to 1.2 μm . For the fresh sample, the majority of the photocurrent originates from charge carriers generated close to the interface. For an aged sample a large part of the photocurrent generated close to the interface is lost. Here both charge carriers can reach the CdS to recombine. Thereby the EBIC signal generated up to 300 nm away from the interface is decreasing. From this a diffusion length of the majority charge carriers of roughly 300 nm can be estimated. However, all the electron-hole pairs generated further away from the interface (between 400 and 1200 nm) are separated by the electric field. Holes (the majority carriers) do not diffuse against the electric field in a significant amount into the CdS anymore, and thus the recombination of the electrons is reduced and they can be extracted. The medium aged sample shows a double peak of photocurrent, from close to the interface as well as from deeper in the bulk, since within the space charge region a maximum recombination occurs when the fermi level passes through the middle between the band edges (or quasi-Fermi levels) while the most aged samples show just one peak further away from the interface.

Therefore the EBIC results confirm the idea that ageing mainly leads to the formation of recombination centers in the CdS, not in the CZTS. The change of the EQE response confirms this effect, since here the photocurrent generated by short wavelength light closer to the CZTS-

CdS interface decreases more than that generated by longer wavelength light deeper inside the absorber.

5. Conclusion

In this paper the degradation mechanism related to copper diffusion into CdS was further investigated by highly spatially resolved optoelectronic techniques. By LBIC an inhomogeneous and locally varying degradation can be observed. By EBIC measurements a depth dependent recombination of the generated charge carriers can be observed. After ageing, charge carriers generated close to the CZTS-CdS interface show a higher recombination rate than those generated further away from the interface deeper in the bulk. The wavelength dependent change of the EQE measurements support these findings. This in combination with the in literature well documented introduction of recombination centers in CdS by copper leads to a strong confidence in the model of the copper diffusion related degradation process.

Acknowledgement

This research was supported by the Estonian Research Council (PUT265, 1-2.10/13/39 and IUT-T4), by the European Union through the European Regional Development Fund, projects TK141 "Advanced materials and high-technology devices for energy recuperation systems" and TAR16016 "Advanced materials and high-technology devices for sustainable energetics, sensorics and nanoelectronics", and by a Mobililitas Pluss Postdoctoral Researcher GrantMOBJD308.

References

- [1] C. Neubauer, A. Samiepour, S. Oueslati, M. Danilson, D. Meissner, Ageing of kesterite solar cells I: degradation processes and their influence on solar cell parameters, *Thin Solid Films* (2019) (vuv (2019) nnnn-nnnn, submitted, and references cited therein).
- [2] H. Sugimoto, H. Hiroi, N. Sakai, S. Muraoka, T. Katou, Over 8% efficiency $\text{Cu}_2\text{ZnSnS}_4$ submodules with ultra-thin absorber, 38th IEEE Photovoltaic Specialists Conference, 2997–3000 2011.
- [3] T. Fukano, S. Tajima, T. Ito, Enhancement of conversion efficiency of $\text{Cu}_2\text{ZnSnS}_4$ thin film solar cells by improvement of sulfurization conditions, *Appl. Phys. Express* 6 (2013) (62301-1-3).
- [4] B. Bissig, C. Guerra-Nunez, R. Carron, S. Nishiwaki, F. La Mattina, F. Pianezzi, P.A. Losio, E. Avancini, P. Reinhard, S.G. Haass, M. Lingg, T. Feurer, I. Utke, S. Buecheler, A.N. Tiwari, Surface passivation for reliable measurement of bulk electronic properties of heterojunction devices, *Small* 12 (2016) 5339–5346.
- [5] D. Meissner, Photovoltaics based on semiconductor powders, in: A. Méndez-Vilas (Ed.), *Materials and Processes for Energy*, Formatex Research Center, Badajoz, 2013, pp. 114–125.
- [6] E. Mellikov, D. Meissner, M. Altosaar, M. Kauk, J. Krustok, A. Õpik, O. Volobujeva, J. Iijina, K. Timmo, I. Klavina, J. Raudoja, M. Grossberg, T. Varema, K. Muska, M. Ganchev, S. Bereznev, M. Danilson, CZTS monograin powders and thin films, *Adv. Mater. Res.* 222 (2011) 8–13.
- [7] C. Neubauer, E. Babatas, D. Meissner, Investigation of rough surfaces on $\text{Cu}_2\text{ZnSn}(\text{S}_{1-x}\text{Se}_x)_4$ monograin layers using light beam induced current measurements, *Appl. Surf. Sci.* 423 (2017) 465–468.
- [8] C. Neubauer, A. Samiepour, S. Oueslati, K. Ernits, D. Meissner, Spatially resolved opto-electrical performance investigations of $\text{Cu}_2\text{ZnSn}_{3.2}\text{Se}_{0.8}$ photovoltaic devices, *Energy Sci. Eng.* 6 (2018) 563–569.
- [9] T.S. te Velde, G.W.M.T. van Helden, *Mongrain Layers*, Philips Technical Review, 29 (1968), pp. 270–274.

Curriculum vitae

Personal data

Name: Christian Neubauer
Date of birth: 03.04.1981
Place of birth: Linz, Austria
Citizenship: Austrian

Contact data

E-mail: c.neubauer@hotmail.com

Education

2011 – 2019 TalTech, PhD
2009 – 2011 TalTech, MSc
2005 – 2009 Upper Austria University of Applied Sciences, Diploma Degree,
Eco Energy Engineering
1995 – 2000 Linzer Technikum, HTL Paul-Hahn-Straße, Elektrotechnik
High School for Electrical Engineering

Language competence

German Native
English Fluent

Professional employment

2009 – crystalsol OÜ, Tallinn, Estonia
Development Engineer
2012 – 2013 Energy Research Institute, Nanyang Technological University,
Singapore
Research Internship
2008 – 2009 Solon Hilber Technologie GmbH, Steinach am Brenner, Austria
Intern
2001 – 2005 Energie AG OÖ, Linz, Austria
Engineer

Other activities and skills

2000 – 2001 Mandatory military service
Certified in environmental management system, standard ISO 14001

Publications

1. Neubauer, C., Samieipour, A., Oueslati, S., Danilson, M., Meissner, D. (2019). Ageing of Kesterite solar cells 1: Degradation processes and their influence on solar cell parameters. *Thin Solid Films*, 669, 595-599.
2. Samieipour, A., Neubauer, C., Oueslati, S., Mikli, V., Meissner, D. (2019). Ageing of Kesterite solar cells 2: Impact on photocurrent generation. *Thin Solid Films*, 669, 509-513.
3. Santos Ortiz, P., Lopez, S., Mangalam, J., Rath, T., Edinger, S., Ursprung, M., Plessing, L., Poelt, P., Trimmel, G., Neubauer, C., Waldauf, C., Meissner, D. (2018). Towards Cd-free R2R CZTSSe-monograin-membrane PV-module production. *35th European Photovoltaic Solar Energy Conference*, Brussels, Belgium.
4. Neubauer, C., Samieipour, A., Oueslati, S., Ernits, K., Meissner, D. (2018). Spatially resolved opto-electrical performance investigations of $\text{Cu}_2\text{ZnSnS}_{3.2}\text{Se}_{0.8}$ photovoltaic devices. *Energy Sci Eng.*, 6, 563-569.

5. Neubauer, C., Babatas, E., Meissner, D. (2017). Investigation of rough surfaces on $\text{Cu}_2\text{ZnSn}(\text{S}_x\text{Se}_{1-x})_4$ monograin layers using light beam induced current measurements. *Appl. Surf. Sci.*, 423, 465-468.
6. Samiepour, A., Kouhiisfahani, E., Galajev, S., Gurevits, J., Kois, J., Neubauer, C., Taskesen, T., Meissner, D. (2016). CZTS monograin membranes for photoelectrochemical water splitting. *Baltic Electrochemistry Conference 2016*, Helsinki, Finland.
7. Ernits, K., Neubauer, C., Xianglin, L., Wong, L.H., Meissner, D., Neisser, A. (2015). Improvement of V_{OC} in $\text{Cu}_2\text{ZnSnS}_4$ monograin layer solar cells with tin oxide inter-layer. Paper presented at the *42nd Photovoltaic Specialist Conference (PVSC)*, New Orleans, LA, USA.
8. Neubauer, C., Babatas, E., Meissner, D. (2015). LBIC characterization of $\text{Cu}_2\text{ZnSn}(\text{S},\text{Se})_4$ monograin photovoltaic cells. *Photovoltaic Technical Conference*, Aix-en-Provence, France.
9. Neubauer, C., Meissner, D. (2014). Spatial surface and material investigation of CZTSSe monograin membranes with LBIC. *ILMaging2014*, Ilmenau, Germany.
10. Samiepour, A., Kouhiisfahani, E., Gurevits, J., Neubauer, C., Galajev, S., Kois, J., Meissner, D. (2014). Biomimetic Membranes for Solar Energy Utilization. *BioEl2014*, Kirchberg, Austria.

Elulookirjeldus

Isiklik informatsioon

Nimi: Christian Neubauer
Sünniaeg: 03.04.1981
Sünnikoht: Linz, Austria
Kodakondsus: Austria

Kontakt

E-post: c.neubauer@hotmail.com

Hariduskäik

2011 – 2019 Tallinna Tehnikaülikool, PhD
2009 – 2011 Tallinna Tehnikaülikool, MSc
2005 – 2009 Upper Austria University of Applied Sciences
Diplomitöö ökoenergeetikas
1995 – 2000 Linzer Technikum, HTL Paul-Hahn-Straße
Elektroonika keskkool

Keelteoskus

Saksa Emakeel
Inglise Väga hea

Töökogemus

2009 – crystalsol OÜ, Tallinn, Estonia
Arendusinsener
2012 – 2013 Energy Research Institute, Nanyang Technological University,
Singapore
Teadusuuringute praktikant
2008 – 2009 Solon Hilber Technologie GmbH, Steinach am Brenner, Austria
Praktikant
2001 – 2005 Energie AG OÖ, Linz, Austria
Insener

Muud tegevused ja oskused

2000 – 2001 Kohustuslik ajateenistus
Rahvusvahelise keskkonnajuhtimise standard, standard ISO 14001

Publikatsioonid

1. Neubauer, C., Samiepour, A., Oueslati, S., Danilson, M., Meissner, D. (2019). Ageing of Kesterite solar cells 1: Degradation processes and their influence on solar cell parameters. *Thin Solid Films*, 669, 595-599.
2. Samiepour, A., Neubauer, C., Oueslati, S., Mikli, V., Meissner, D. (2019). Ageing of Kesterite solar cells 2: Impact on photocurrent generation. *Thin Solid Films*, 669, 509-513.
3. Santos Ortiz, P., Lopez, S., Mangalam, J., Rath, T., Edinger, S., Ursprung, M., Plessing, L., Poelt, P., Trimmel, G., Neubauer, C., Waldauf, C., Meissner, D. (2018). Towards Cd-free R2R CZTSSe-monograin-membrane PV-module production. *35th European Photovoltaic Solar Energy Conference*, Brussels, Belgium.
4. Neubauer, C., Samiepour, A., Oueslati, S., Ernits, K., Meissner, D. (2018). Spatially resolved opto-electrical performance investigations of $\text{Cu}_2\text{ZnSnS}_{3.2}\text{Se}_{0.8}$ photovoltaic devices. *Energy Sci Eng.*, 6, 563-569.

5. Neubauer, C., Babatas, E., Meissner, D. (2017). Investigation of rough surfaces on $\text{Cu}_2\text{ZnSn}(\text{S}_x\text{Se}_{1-x})_4$ monograin layers using light beam induced current measurements. *Appl. Surf. Sci.*, 423, 465-468.
6. Samiepour, A., Kouhiisfahani, E., Galajev, S., Gurevits, J., Kois, J., Neubauer, C., Taskesen, T., Meissner, D. (2016). CZTS monograin membranes for photoelectrochemical water splitting. *Baltic Electrochemistry Conference 2016*, Helsinki, Finland.
7. Ernits, K., Neubauer, C., Xianglin, L., Wong, L.H., Meissner, D., Neisser, A. (2015). Improvement of V_{OC} in $\text{Cu}_2\text{ZnSnS}_4$ monograin layer solar cells with tin oxide inter-layer. Paper presented at the *42nd Photovoltaic Specialist Conference (PVSC)*, New Orleans, LA, USA.
8. Neubauer, C., Babatas, E., Meissner, D. (2015). LBIC characterization of $\text{Cu}_2\text{ZnSn}(\text{S},\text{Se})_4$ monograin photovoltaic cells. *Photovoltaic Technical Conference*, Aix-en-Provence, France.
9. Neubauer, C., Meissner, D. (2014). Spatial surface and material investigation of CZTSSe monograin membranes with LBIC. *ILMaging2014*, Ilmenau, Germany.
10. Samiepour, A., Kouhiisfahani, E., Gurevits, J., Neubauer, C., Galajev, S., Kois, J., Meissner, D. (2014). Biomimetic Membranes for Solar Energy Utilization. *BioE/2014*, Kirchberg, Austria.

